Reliability and Compact Modeling of Gamma-Irradiated 4H-SiC Bipolar Devices and Circuits

ALEXEY METREVELI

Doctoral Thesis in Information and Communication Technology, Integrated Devices and Circuits
KTH Royal Institute of Technology

Stockholm, Sweden 2026

S. et T. in memoriam
Ab illis via coepit; in hoc opere lumen eorum manet.

Abstract

This thesis investigates the radiation response of 4H-SiC bipolar junction transistors and integrated TTL inverter circuits under gamma irradiation, with emphasis on the role of bias conditions, dose rate, temperature, and oxide/interface processing. The work combines in-situ irradiation experiments using a ^{60}Co source, device- and circuit-level electrical characterization, and compact modelling approaches to establish a consistent understanding of radiation-induced degradation mechanisms in this technology.

The results show that the dominant degradation mechanism in the studied devices is an increase in base current, leading to a reduction in current gain. This behaviour is attributed to radiation–induced charge trapping in oxide layers and the formation of interface states at the SiC/SiO_2 boundary, which enhance surface recombination. Despite the wide bandgap of 4H-SiC and its intrinsically low carrier concentration, the radiation response is governed primarily by interface–controlled processes rather than by bulk material properties.

A key finding is the dependence of degradation on the electrical bias applied during irradiation. Passive or zero-bias conditions are shown to produce more severe degradation than active bias configurations.

Circuit-level experiments demonstrate that transistor degradation propagates into inverter behavior through shifts in transfer characteristics and changes in supply current. While circuits may remain operational after irradiation, their functional margins are reduced and become strongly dependent on the bias conditions.

The thesis also introduces a compact modelling framework that links radiation-induced physical mechanisms to SPICE-compatible parameters, enabling predictive circuit-level simulations under irradiation conditions.

The overall conclusion is that radiation hardness in 4H-SiC bipolar electronics in many cases can be much higher compared to silicon devices, but the radiation hardness should be understood as a condition-dependent system property, rather than as an intrinsic material characteristic.

Keywords: 4H-SiC; bipolar junction transistor; TTL inverter; gamma irradiation; total ionizing dose; radiation hardness; ELDRS; interface traps; compact modelling; SPICE.

Sammanfattning

Denna avhandling undersöker strålningsresponsen hos bipolära transistorer och integrerade TTL inverterarkretsar baserade på 4H-SiC komponenter exponerade för gammastrålning, med särskild betoning på betydelsen av biaseringsförhållanden, doshastighet, temperatur samt laddningsuppbyggnad i oxidlager- och gränsskikt. Arbetet kombinerar in-situ bestrålningsexperiment med en ^{60}Co-källa, elektrisk karakterisering på komponent- och kretsnivå, samt kompakta modelleringsmetoder för att etablera en konsekvent förståelse av strålningsinducerade degraderingsmekanismer i denna teknologi.

Resultaten visar att den dominerande degraderingsmekanismen i de studerade komponenterna är en ökning av basströmmen, vilket leder till en minskning av strömförstärkningen. Detta beteende tillskrivs strålningsinducerad laddningsinfångning i oxidlager samt bildning av gränsskiktstillstånd vid SiC/SiO_2 gränsytan, vilket förstärker ytrekombinationen. Trots det breda bandgapet hos 4H-SiC och dess intrinsiskt låga laddningsbärarkoncentration styrs strålningsresponsen huvudsakligen av gränsskiktsstyrda processer snarare än av bulkmaterialets egenskaper.

Ett centralt resultat är att degraderingen är klart beroende av den elektriska biaseringen som appliceras under bestrålning. Passiva eller icke biaserade tillstånd visar sig ge upphov till mer uttalad degradering än aktiva biasförhållanden.

Experiment på kretsnivå visar att degradering på transistornivå fortplantas till beteendet hos integrerade inverterarekretsar genom förskjutningar i överföringskarakteristiken och förändringar i matningsströmmen. Även om

kretsar kan förbli funktionella efter bestrålning, reduceras deras funktionsmarginaler och blir starkt beroende av driftförhållandena.

Avhandlingen introducerar även ett kompakt modelleringsramverk som kopplar strålningsinducerade fysikaliska mekanismer till SPICE-kompatibla parametrar, vilket möjliggör prediktiva simuleringar av kretsbeteende under bestrålningsförhållanden.

Den övergripande slutsatsen är att strålningshärdighet i 4H-SiC-baserad bipolär elektronik bör betraktas som en tillståndsberoende systemegenskap, snarare än som en inneboende materialegenskap. Dessutom konstateras att dessa 4H-SiC komponenter och kretsar i flera fall kan vara mer än 10 gånger så strålningshärdiga som motsvarande kiselkomponenter.

Nyckelord: 4H-SiC; bipolär transistor; TTL-inverterare; gammastrålning; total joniserande dos; strålningshärdighet; gränsskiktstillstånd; kompakt modellering

Acknowledgments

I would like to express my sincere gratitude to my main supervisor, Carl-Mikael Zetterling, for giving me the opportunity to work on this topic and for introducing me to the field of Silicon Carbide electronics. His support made it possible for me to gain long-term experience in an international research environment.

I am especially and warmly grateful to Anders Hallén, my co-supervisor, mentor, and friend. His continuous support, guidance, and encouragement throughout the years have meant a great deal to me. His rare ability to combine scientific depth with genuine human understanding has had a lasting impact on my journey.

I would also like to thank my colleagues and collaborators from Italy, Japan, Russia, Korea and US, as well as everyone who was involved in the experiments and research work. The shared effort, discussions, and time spent together, often under challenging conditions, have been an essential and memorable part of this thesis.

I am grateful to Jiantong Li, who, although we did not formally work together, has always been a supportive senior colleague and a source of thoughtful advice. His openness, enthusiasm, and willingness to share insights made many of our conversations both intellectually stimulating and genuinely enjoyable.

My special thanks go to Susanna Pozzoli, a colleague and a close friend, whose loyalty, support, and presence throughout the years have meant more to me than words can fully express.

I would also like to thank Victoria Moshukova for being a constant presence in my life, both during difficult moments and happier times. Her support, understanding, and quiet strength have been, and still is, deeply important to me.

I would like to express my deepest appreciation to all staff of the Kista cleanroom facilities and the Electrum Laboratory. Their quiet, continuous, and highly skilled work forms the true foundation upon which experimental science is built. Their dedication, practical knowledge, and willingness to help have been indispensable for this thesis. Without their support, guidance, and patience, none of the experimental results presented here would have been possible.

Finally, I would like to thank my family for being part of my life and for their support over the years. This journey has not been without its challenges, and I am grateful for all the people who have stood by me throughout this time.

I am also deeply thankful for the new people who have come into my life more recently, bringing encouragement, belief, and a sense of purpose at a time when it was most needed.

List of publications

This doctoral dissertation consists of two parts. The first part provides an overview of the research area, together with a summary of the main contributions.
The second part contains the contributions in the form of published papers, as listed below.

List of Papers Included in The Thesis:

I. In-situ Gamma Irradiation Effects on 4H-SiC Bipolar Junction Transistors
Alex Metreveli; Anders Hallén; Ilaria Di Sarcina; Alessia Cemmi; Jessica Scifo; Adriano Verna; Carl-Mikael Zetterling
IEEE Transactions on Nuclear Science, vol. 70, no. 12, pp. 2597-2604,,
doi: 10.1109/TNS.2023.3326608, 2023

II. The Impact of Gamma Irradiation on 4H-SiC Bipolar Junction Inverters under Various Biasing Conditions
Alex Metreveli; Anders Hallén; Ilaria di Sarcina; Alessia Cemmi; Adriano Verna; Carl Mikael Zetterling
Solid State Phenomena, vol. 361, pp. 71–76, doi: 10.4028/p-O7afLP, 2024

III. Impact of interface oxide type on the gamma radiation response of SiC TTL ICs
Alex Metreveli; Van Cuong, Vuong; Shin-Ichiro Kuroki; Kenichi Tanaka; Carl-Mikael Zetterling
Facta universitatis, vol. 37, no. 4, pp. 599–607, doi: 10.2298/FUEE2404599M, 2024

IV. SPICE Model for SiC Bipolar Transistor and TTL Inverter Degradation Due to Gamma Radiation

Alex Metreveli; Anders Hallén; Carl-Mikael Zetterling

Micromachines, vol. 16, no. 11, p. 1246, doi: 10.3390/mi16111246, 2025

V. Enhanced Gamma Radiation Sensitivity of 4H-SiC Bipolar Junction Transistors at Low Temperature

A. Metreveli, A. Hallén and C.-M. Zetterling

IEEE 34th International Conference on Microelectronics (MIEL), Nis, Serbia: IEEE, pp. 1–6. doi: 10.1109/MIEL66332.2025.11261143, 2025

List of abbreviations

Abbreviation	Explanation
4H-SiC	4H polytype of silicon carbide
AEC-Q101	Automotive Electronics Council Qualification Standard 101
ATOX	Atomic oxygen
BFOM	Baliga figure of merit
BJT	Bipolar junction transistor
BWR	Boiling water reactor
CGS	Centimetre–gram–second system
CME	Coronal mass ejection
CMOS	Complementary metal–oxide–semiconductor
COTS	Commercial off-the-shelf
CRAND	Cosmic ray albedo neutron decay
CVD	Chemical vapour deposition
DC	Direct current
DD	Displacement damage
DIP	Dual in-line package
DUT	Device under test
ECSS	European Cooperation for Space Standardization
ECSS-E-HB	ECSS Engineering Handbook
ECSS-E-ST	ECSS Engineering Standard
ECSS-Q-ST	ECSS Product Assurance Standard
EEE	Electrical, electronic, and electromechanical

EEE-INST-002	NASA Goddard EEE parts selection, screening, qualification, and derating instruction
ELDRS	Enhanced low dose rate sensitivity
EM	Electromagnetic
EMC	Electromagnetic compatibility
ENEA	Italian National Agency for New Technologies, Energy and Sustainable Economic Development
ERB	Earth's radiation belts
ESCC	European Space Components Coordination
ESD	Electrostatic discharge
ESA	European Space Agency
ESR	Electron spin resonance
FBR	Fast breeder reactor
GCR	Galactic cosmic rays
GEO	Geostationary Earth orbit
GPS	Global Positioning System
GSFC	Goddard Space Flight Center
HDR	High dose rate
HEMT	High-electron-mobility transistor
HV	High voltage
HZE	High-charge and high-energy particles
IAEA	International Atomic Energy Agency
IC	Integrated circuit
ICP-RIE	Inductively coupled plasma reactive-ion etching
IR	Infrared
JAXA	Japan Aerospace Exploration Agency
JERG	JAXA Engineering Requirement / JAXA Engineering Standard system
JGO	Jupiter Ganymede Orbiter
JTE	Junction termination extension
JUICE	JUpiter ICy moons Explorer
KTH	KTH Royal Institute of Technology
LDR	Low dose rate
LEO	Low Earth orbit
LET	Linear energy transfer

MIL-STD	Military Standard
MOS	Metal–oxide–semiconductor
MOSFET	Metal–oxide–semiconductor field-effect transistor
NASA	National Aeronautics and Space Administration
NIEL	Non-ionizing energy loss
PCB	Printed circuit board
PECVD	Plasma-enhanced chemical vapour deposition
PID	Proportional–integral–derivative
PWR	Pressurized water reactor
QST	National Institutes for Quantum Science and Technology
RDM	Radiation design margin
RF	Radio frequency
RHA	Radiation hardness assurance
RLAT	Radiation lot acceptance testing
SAA	South Atlantic Anomaly
SCR	Solar cosmic rays
SEB	Single-event burnout
SEE	Single-event effects
SEGR	Single-event gate rupture
SEP	Solar energetic particles
SHIELDOSE	Shielding dose calculation model/code
SiC	Silicon carbide
SiO_2	Silicon dioxide
SOA	Safe operating area
SOI	Silicon-on-insulator
SPE	Solar proton event
SPENVIS	Space Environment Information System
SPICE	Simulation Program with Integrated Circuit Emphasis
SRH	Shockley–Read–Hall
SWR	Supercritical water reactor
TAT	Trap-assisted tunnelling
TEOS	Tetraethyl orthosilicate
TIARA	Takasaki Ion Accelerators for Advanced Radiation Application

TID	Total ionizing dose
TTL	Transistor–transistor logic
UWBG	Ultra-wide-bandgap
VBIC	Vertical Bipolar Inter-Company model
VTC	Voltage transfer characteristic
WBG	Wide-bandgap

CONTENTS

Abstract I
Acknowledgments V
List of publications VII
List of abbreviations IX
Chapter 1. Introduction 17
1.1 Background and Motivation 17
1.2 Research Objectives and Questions 21
1.2.1 Technological Heritage: From 500 °C to System Integration 21
1.2.2 Problem Statement: From “Survivability” to Qualification 23
1.2.3 Research Objectives 24
1.2.4 Scientific Novelty and Contribution 24
1.2.5 Principal Findings 25
1.3 Structure of the Thesis 26
Chapter 2. Radiation and Its Effects on Materials 27
2.1 Overview of Radiation Phenomena 27
2.1.1 Radiation 27
2.1.2 Metrology and Unit Systems in Radiation Physics 29
2.1.3 Atmospheric Shielding and the Radiation Cascade 32
2.1.4 Mechanisms of Gamma-Photon Interaction with Semiconductor Structures 35
2.2. Spectral Composition and Particle Nature 39
2.1.4.3 Physical Mechanism of Modulation 40
2.2.1 Galactic Cosmic Rays (GCR) 40
2.2.2 Solar Cosmic Rays (SCR) 40
2.2.3 Geomagnetic Trapping and Earth’s Radiation Belts 41
2.2.4 Electromagnetic Factors and Spacecraft Charging 41
2.2.5 Specific Radiation Loads for Typical Orbits 42
2.2.6 Metrology of Radiation Effects: Fluence, Spectra, and LET 44
2.2.5 Secondary Radiation and Spectral Transformation Behind Shielding 45
2.3 Requirements for Semiconductor Devices in Space Applications 45
2.3.1 Radiation Hardness Assurance Concept and Design Margins 45
2.3.2 U.S. Department of Defense (MIL-STD) and NASA Standards 46
2.3.3 European Standardization System 47
2.3.4 JAXA Standards (Japan) and International Harmonization (ISO) ... 48
2.3.5 “New Space”, COTS, and Automotive Standards (AEC-Q101) 49

2.3.6 Summary of Section Harmonizing Requirements for SiC 49
Chapter 3. SiC Material, Devices, and Their Interaction with Radiation 50
3.1 Structural and Electrophysical Parameters of Silicon Carbide as a Wide-Bandgap Semiconductor 50
3.1.1 Crystal Structure and Polytypism 50
3.1.2 Band Structure and Intrinsic Carrier Concentration 51
3.1.3 Critical Breakdown Field and Baliga Scaling 52
3.1.4 Thermal Conductivity and Thermodynamic Stability 53
3.1.5 Challenges of the SiC/SiO_2 interface 54
3.1.6 Recombination Mechanisms: Auger, SRH, and Surface Recombination 55
3.2 Operating Principles and Process-Design Features of SiC BJTs 56
3.2.1 Vertical Architecture and Mesa Technology 56
3.2.2 Current Gain (β) and Its Limiting Factors 56
3.2.3 Impact of Incomplete Dopant Ionization 57
3.3 Review of Radiation Effects in Wide-Bandgap Devices 57
3.3.1 Intrinsic and Extrinsic Radiation Hardness: Comparative Materials Physics 58
3.3.2 Total Ionizing Effects (TID): The Interface Problem in WBG Electronics 62
3.3.3 Displacement Damage 64
3.3.4 Temperature Dependence and the “Self-Recovery Window” 64
3.3.5 Conclusion 65
Chapter 4. Experimental Methodology, Test Setup, and Parameter Extraction 66
4.1 Overview of Experimental Design 66
4.2 Standards as “design rules” for the experiment (ESA / NASA / MIL logic, expressed as controlled variables) 67
4.3 Gamma Radiation Testing Setup and Protocols 68
4.3.1 Timing Rules and Annealing Windows 68
4.3.2 Dosimetry and irradiation-field uniformity: what was controlled and how cross-facility comparability was protected 68
4.3.5 Bias-state realism: aligning experimental regimes with NASA/MIL expectations for “does it still operate?” 69
4.4 Data Collection and Analysis Techniques 69
Chapter 5. Experimental Results 73
5.1 Paper I: In-situ Gamma Irradiation Effects on 4H-SiC Bipolar Junction Transistors 73

5.2 Paper II: The Impact of Gamma Irradiation on 4H-SiC Bipolar Junction Inverters under Various Biasing Conditions 74
5.3 Paper III: Impact of Interface Oxide Type on the Gamma Radiation Response of SiC TTL IC´s 75
5.4 Paper IV: SPICE Model for SiC Bipolar Transistor and TTL Inverter Degradation Due to Gamma Radiation 77
5.4.1 Increase in saturation current (IS) 78
5.4.2 Increase in Base Resistance (RB) 78
5.4.3 Forward Transit Time (τF) 78
5.5 Paper V: Enhanced Gamma Radiation Sensitivity of 4H-SiC Bipolar Junction Transistors at Low Temperatures 80
5.5.1 Does Low Temperature Improve or Worsen Radiation Stability?. 80
5.5.2 Physical Interpretation: The “Frozen Hole” Model........................ 81
Chapter 6. Discussion..82
6.1 Comparison of Radiation Hardness of Si and SiC Bipolar Transistors 82
6.1.1 Physical Interpretation: Absolute Current Scale, Bandgap, and Device Topology... 84
Chapter 7. Conclusions 87
References...89

Chapter 1. Introduction

1.1 Background and Motivation

The evolution of the global semiconductor industry has reached a milestone increasingly described as the transition to the "post-Moore" era. For decades, Moore's Law and classical Dennard scaling drove performance growth primarily through the geometric reduction of transistor sizes. However, in power electronics and electronics for harsh environments, the center of gravity has shifted: what matters now is not just the increase in computing density, but how efficiently electrical energy is generated, converted, switched, and dissipated in real-world systems [1], [2]. In this context, the development of electronics is largely shifting from the further optimization of the silicon platform to the broader implementation of, for instance, wide-bandgap (WBG) and ultra-wide-bandgap (UWBG) semiconductors, which possess a different set of physical limits. Among these, the 4H polytype of silicon carbide (4H-SiC) has established the most mature industrial position in high-voltage and high-temperature electronics by the mid-2020s, thanks to its combination of a wide bandgap, high critical breakdown field, high thermal conductivity, and an already established manufacturing ecosystem [3], [4], [5].

This thesis assesses physical property, which is inherent in WBG semiconductors, namely the resistance to radiation. All electronic systems encounter various types of radiation, but the type of radiation and dose levels varies considerably and can be problematic in some extreme environments such as space. These types of application are summarized schematically in Figure 1.1, which links the environmental driver to the corresponding electronics requirement: reduced shielding mass in space systems, high-temperature operation in planetary and nuclear environments, and radiation tolerance in reactor and accelerator systems.

The demand for more radiation hard electronics in space is driven by three strategic sectors:

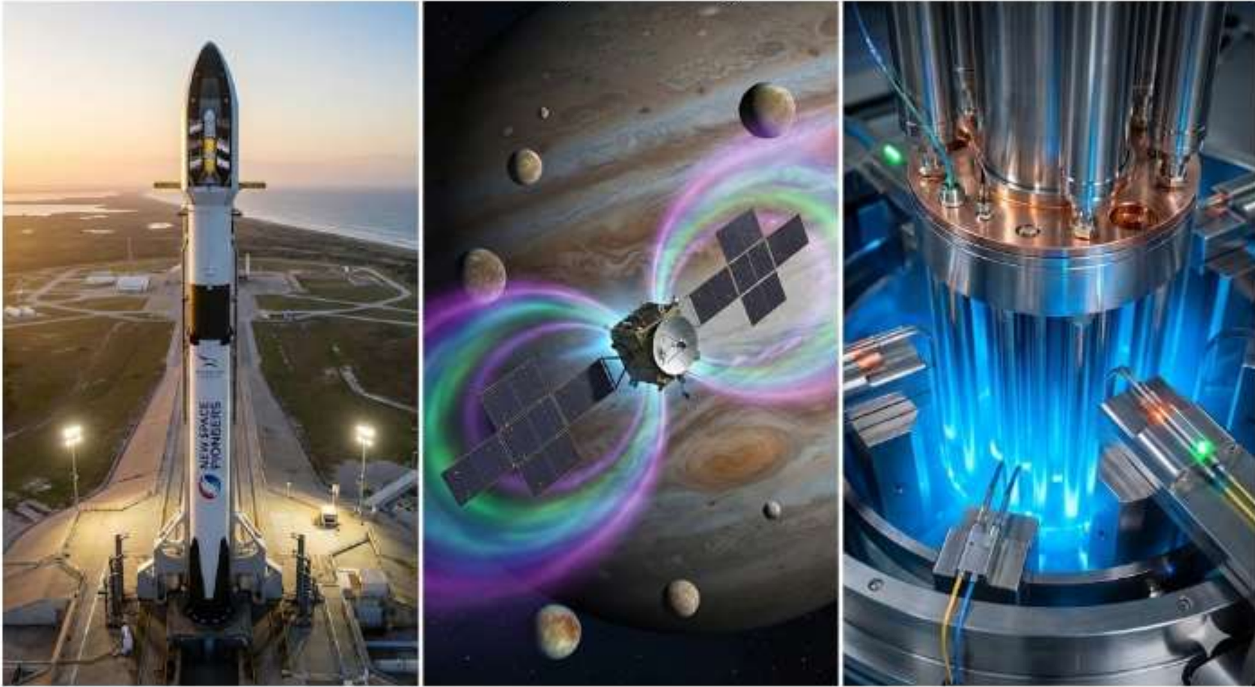

Figure 1.1. Illustrative examples of space and harsh-environment applications motivating the development of radiation-hardened electronics, aerospace and new space, deep space explorations, and nuclear power and high energy physics electronics.

Aerospace and “New Space”: The commercialization of near-Earth space necessitates a radical reduction in satellite launch mass. Traditional Si-based electronics require massive shielding (lead/aluminum) to operate within Earth’s radiation belts, imposing an unacceptable weight penalty for small satellites and constellations [2].

Deep space exploration: Missions to the Jovian system (e.g., JUICE, Europa Clipper) or the surface of Venus face conditions where active cooling is either impossible or energetically inefficient. Radiation doses in the Jovian system can exceed 100 krad(Si), and for extended missions, reach tens of Mrad, lying far beyond the operational envelope of standard Si devices without heavy shielding [6], [7].

Nuclear power and high-energy physics: Detectors and electronics situated inside reactor vessels or next generation of the colliders are subjected to neutron fluxes that induce irreversible structural damage to the crystal lattice [8].

The operability of any semiconductor device is limited by the intrinsic carrier concentration (n_i), which increases exponentially with temperature. For Si, having a bandgap $E_g \approx 1.14$ eV, at temperatures above 150–200 °C, the concentration of n_i becomes comparable to the doping level of low-doped drift regions (typically $10^{14} - 10^{15}$ cm^{-3}). This leads to the loss of p-n junction controllability, a sharp increase in leakage currents, and thermal runaway [9]. In contrast, 4H-SiC ($E_g \approx 3.26$ eV) possesses an intrinsic carrier concentration 17–18 orders of magnitude lower, preserving p-n junction functionality up to 800–1000 °C. This makes it a strong candidate for Venus surface applications and for in-engine monitoring [4].

The intrinsic carrier concentration is a key parameter that determines the high-temperature performance of a semiconductor. As shown in Figure 1.2, 4H-SiC exhibits a significantly

lower intrinsic carrier concentration compared to silicon and other WBG semiconductors over a wide temperature range.

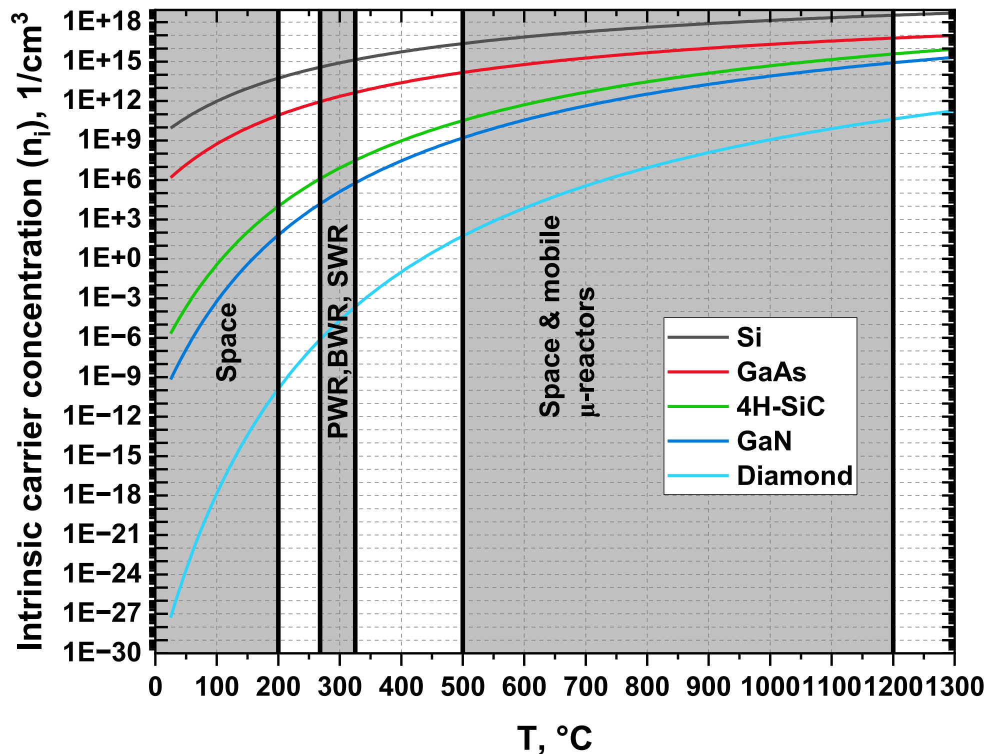

Figure 1.2. Intrinsic carrier concentration (n_i) as a function of temperature for silicon and 4H-SiC. Due to its wide bandgap, 4H-SiC maintains an extremely low intrinsic carrier concentration even at elevated temperatures, which enables stable high-temperature operation and contributes to its potential radiation tolerance. The plot indicates the device failure limit corresponding to a doping level of 10^{15} cm^{-3} [9].

The shaded regions in Figure 1.2 map the intrinsic carrier concentration limits to the operational temperature ranges of three critical harsh-environment applications:

1. Space (Aerospace: up to ~150 °C): Standard onboard electronics for Low Earth Orbit orbit (LEO) and deep space missions typically operate within the military-standard temperature range of -55 °C to +125 °C. Within this zone, the n_i of Si remains strictly below the typical drift-region doping level of 10^{15} cm^{-3}. This allows classical Si-based components to function reliably, provided there is an adequate thermal management system.
2. PWR, BWR, SWR (Commercial Nuclear Reactors: 250–350 °C): This region corresponds to the active zones and coolant loops of pressurized water reactors (PWR), boiling water reactors (BWR), and supercritical water reactors (SWR). Typical primary coolant temperatures range from 280 °C to 350 °C. As the graph demonstrates, at T > 200 °C, n_i . of silicon exponentially crosses the 10^{15} cm^{-3} failure threshold. Deploying sensors or power electronics here necessitates wide-bandgap materials to prevent thermal runaway.

3. Space & mobile μ-reactors (advanced nuclear systems: 500–1200 °C): Next-generation energy systems, such as space nuclear propulsion, NASA's kilo power reactors (using liquid sodium heat pipes at ~800 °C), and gas-cooled mobile microreactors, operate in extreme thermal domains. In this >500 °C regime, 4H-SiC and other UWBG materials demonstrate their absolute superiority. Their n_i remains orders of magnitude below the critical 10^{15} cm^{-3} threshold, enabling uncooled, close-coupled control electronics and sensors directly within the reactor's hot zone.

Silicon has a low threshold displacement energy ($E_d \approx 13 - 20$ eV). The displacement threshold is the minimum energy needed to fully knock out atoms from their lattice positions. This makes it highly susceptible to the formation of point defects, such as Frenkel pairs, upon bombardment by heavy particles (protons or neutrons). In 4H-SiC, due to the high strength of the Si–C covalent bond (4.6 eV vs. 2.3 eV for Si–Si), the displacement threshold energy is significantly higher ($E_{d,Si} \approx 35$ eV, $E_{d,C} \approx 20$ eV). This provides the crystal lattice with "intrinsic" radiation hardness against structural damage [10], [11]. In addition, the wide bandgap itself, reflecting the energy needed to form an electron-hole-pair (ehp) by ionizing electrons in the valence band of the material and promote them to mobile states in the conduction band, is a highly desirable quantity for reducing the formation of ehp. Since much of the energy absorbed from radiation results in ionization of the semiconducting material, the high levels of extra charges may severely inflict on the operation of semiconductor devices.

Among WBG materials, 4H-SiC is selected for this work due to a unique combination of properties, as illustrated in the comparative diagram in Figure 3.

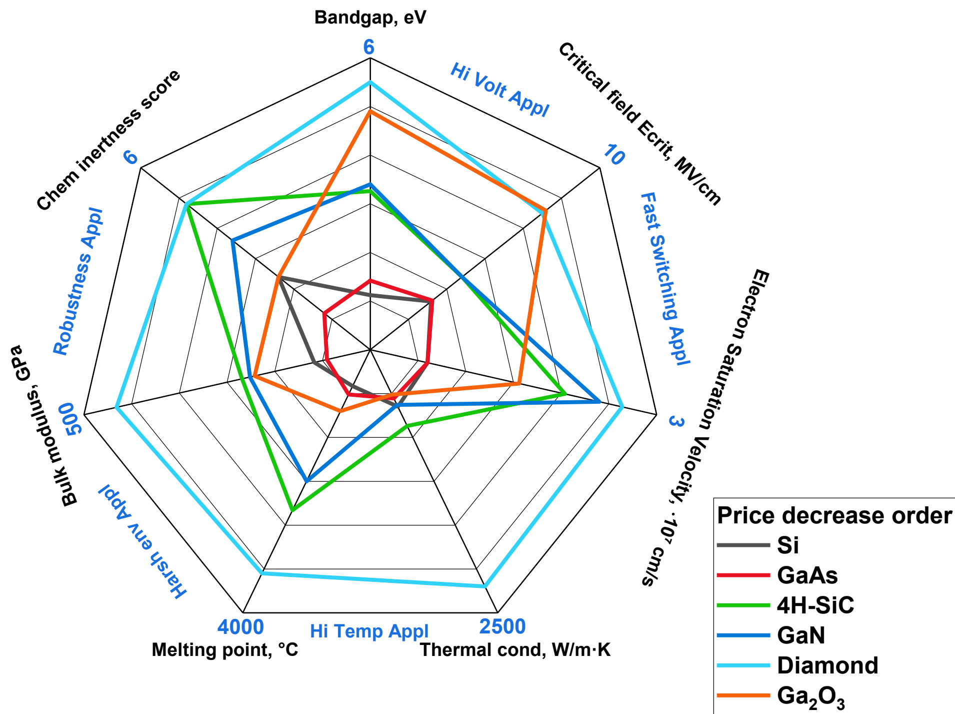

Figure 1.3. Comparative assessment of physical properties ("Figures of Merit") for key semiconductor materials, normalized to Silicon.

Key Advantages of 4H-SiC:

- Thermal conductivity ($\lambda \approx 3.7$ W/cm·K): Three times higher than Si and superior to GaN (1.3 W/cm·K). This is critical for efficient heat dissipation in vacuum environments [3].
- Critical electric field ($E_{crit} \approx 2.5$ MV/cm): Enables the design of high-voltage devices with thinner drift layers and lower On-Resistance (R_{on}) [5].
- Technological maturity: Unlike GaN, which is typically grown on foreign substrates, SiC benefits from the availability of native substrates with diameters up to 150–200 mm. This ensures the low dislocation density required for reliable vertical devices [3].

Thus, the transition to 4H-SiC is not merely a parametric improvement, but a prerequisite for creating electronics capable of surviving in the “Post-Moore” era of extreme applications.

1.2 Research Objectives and Questions

This thesis is part of a long-term effort at KTH to develop 4H-SiC bipolar electronics for environments in which conventional silicon and SOI technologies become unreliable. The work should therefore be understood not as an isolated radiation study, but as a step in the maturation of a technology platform: from discrete bipolar transistors, to integrated TTL logic, and finally to compact models suitable for circuit-level prediction.

The motivation for this work arises from a gap between demonstrated survivability and qualification-relevant understanding. Earlier work on the KTH 4H-SiC bipolar platform showed that devices and circuits can remain functional after very high radiation doses. However, survivability alone is not sufficient for system design. A component intended for space, nuclear, or accelerator environments must be characterized under realistic operating conditions, including bias state, dose rate, temperature, circuit topology, and processing route. In particular, bipolar devices are vulnerable not only to bulk displacement damage (DD), but also to radiation-induced changes in surface recombination and interface-controlled base current.

The central research question of this thesis is therefore how gamma irradiation modifies the electrical behaviour of 4H-SiC bipolar devices and integrated circuits (ICs) under operating conditions relevant for harsh-environment electronics. The thesis addresses this question by combining in-situ ^{60}Co irradiation experiments, bias-dependent transistor and inverter characterization, oxide-process comparison, low-temperature exposure, and compact SPICE-oriented degradation modelling.

1.2.1 Technological Heritage: From 500 °C to System Integration

The KTH 4H-SiC BJT platform’s evolution can be divided into five key phases, each solving a fundamental problem of high-temperature electronics while leaving the question of radiation reliability open.

The progression shown in Figure 1.5 demonstrates that the KTH platform has evolved from device fabrication to integrated high-temperature systems. The remaining step, and the focus of this thesis, is to convert demonstrated survivability into a qualification-relevant understanding of radiation response under controlled bias, dose-rate, temperature, and process conditions.

Phase 1: Device Fundamentals (Ghandi, 2011) Reza Ghandi established the process baseline: the fabrication of high-voltage bipolar junction transistors (BJTs) without using ion implantation in the active base region [9].

- Key achievement: Optimization of thermal oxidation and surface passivation to suppress recombination currents, which allowed for achieving a stable current gain (β).
- Limitation: Research focused exclusively on power electronics and did not address low-voltage applications or radiation hardness.

Phase 2: Extreme temperature digital logic (Lanni, 2014): Luigia Lanni made the transition from discrete devices to ICs. The world's first monolithic TTL logic on 4H-SiC capable of stable operation from -40 °C to +600 °C was demonstrated [4].

- Significance: Lanni demonstrated that BJTs, unlike SiC MOSFETs, avoid the threshold-voltage drift and gate-dielectric instability that complicate high-temperature MOS operation. However, the behavior of this logic under simultaneous temperature and ionizing radiation exposure remained outside the scope of the work.

Phase 3: Analog Complexity and Mixed-Signals (Shakir, 2019) Muhammad Shakir raised the integration level by developing complex analog blocks: a 555-timer, comparators, and operational amplifiers operating at 500 °C [12].

- Connection to this work: Shakir's work is critical for understanding the relevance of the current study. Analog circuits (timers, ADCs) are far more sensitive to transistor parameter degradation than digital logic. While a logic gate might function even with a 50% drop in current amplification, β, (due to noise margins), for a timer, changes in leakage currents or gain result in frequency drift and functional failure. This thesis provides the models necessary to predict the reliability of such sensitive nodes.

Phase 4: RF and sensor interfaces (Hussain, 2019; Hou, 2019)

- Hussain adapted the technology for RF applications (mixers, amplifiers up to 500 °C) [13], demonstrating the feasibility of "hot" transceivers.
- Hou integrated photodiodes and two-level metallization into the process, creating a foundation for "smart" sensors [14].

Phase 5: Radiation "Survivability" vs. Reliability (Suvanam, 2017)

- Early radiation tests (Suvanam) showed that SiC circuits can survive doses up to 100 Mrad [7]. However, these tests were performed primarily in passive mode at high dose rates. They proved the material's potential but did not provide data for

qualification, as they ignored Enhanced Low Dose Rate Sensitivity (ELDRS), bias effects, and low temperature.

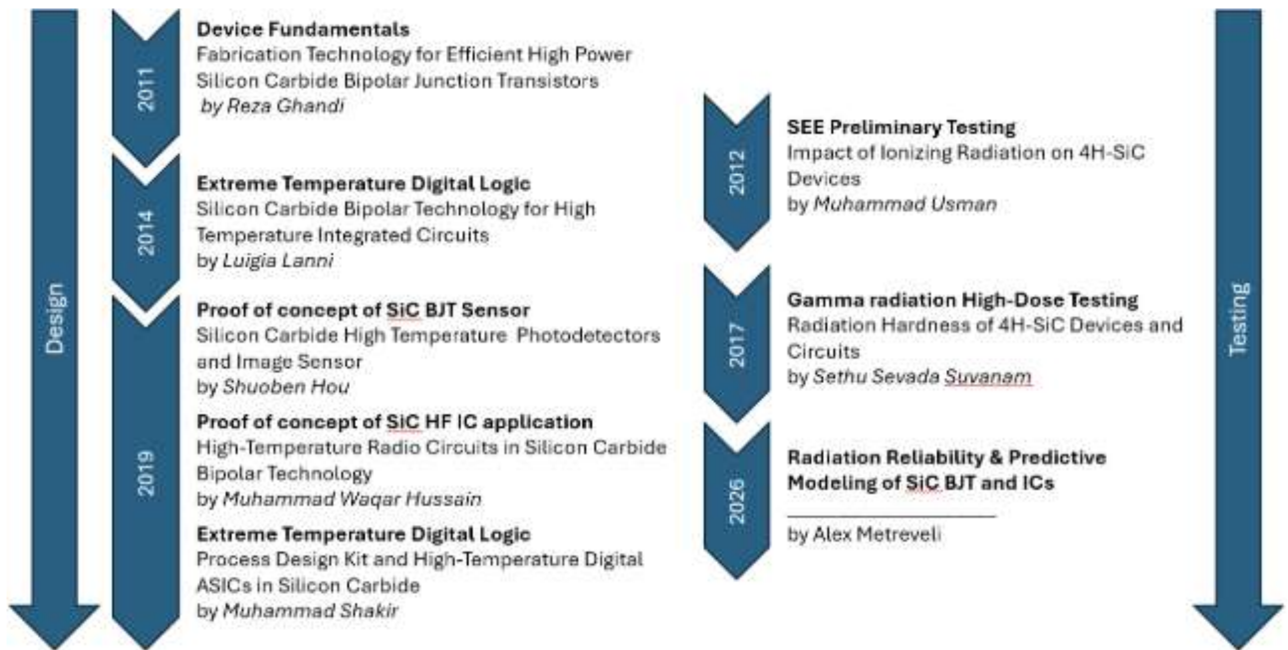

Figure 1.5. Evolution of the KTH SiC bipolar platform: from the development of a basic device to complex analog systems and ensuring their radiation reliability.

1.2.2 Problem Statement: From "Survivability" to Qualification

Three fundamental problems stand out that have not been resolved in previous works:

1. Uncertainty of enhanced dose rate sensitivity (ELDRS) in SiC: in silicon bipolar technologies, the ELDRS phenomenon is well known. As noted by Johnston and Fleetwood [9], [10], standard accelerated tests (50–300 rad/s) can underestimate degradation in space (0.01 rad/s) by a factor of 5–10 due to slow hole transport and interface trap formation.

- Gap: Until now, the presence of ELDRS in high-voltage 4H-SiC BJTs remained debatable. The lack of data on dose rate dependence makes it impossible to calculate design margins for long-duration missions.

2. Ignoring the "Bias Paradox", traditional intuition for MOS device developers suggests that the worst-case irradiation regime is the "ON" state, where the electric field in the oxide is maximal and facilitates the separation of electron-hole pairs.

- Gap: For bipolar devices, where the critical zone is the emitter-base spacer, this rule may not apply. In the absence of an external field (cut-off or storage mode), holes can be trapped more efficiently near the junction, causing stronger gain degradation in β than in the active mode. A systematic study of the "Worst-case bias" vector for SiC BJTs has not been performed previously.

3. Cryogenic vulnerability. All previous KTH platform works focused on the high-temperature range (> 300 °C). However, a spacecraft heading, for example, to Jupiter, spends years in "cold" space conditions (-100 °C to -50 °C) in a passive mode.

- Gap: The effect of low temperatures on the "freezing" of radiation defects in SiC and the suppression of dynamic annealing has not been studied. There is a risk that "cold" irradiation leads to critical charge accumulation that does not anneal as it would at room temperature.

1.2.3 Research Objectives

The overall objective of the thesis is to convert earlier evidence of SiC device survivability into a more complete radiation-hardness-assurance methodology for the KTH bipolar technology. In practical terms, the goal is to provide a basis for designers to judge not only whether a device survives irradiation, but also how much functional margin remains in circuits operated under realistic mission conditions.

To reach this objective, the work combines four lines of inquiry. First, it maps the experimental stress space through in-situ gamma irradiation of BJTs and logic inverters while varying bias state, dose rate, and temperature. second, it separates surface- and bulk-related degradation mechanisms in order to determine whether the observed loss of current gain is governed mainly by interface-controlled ionization damage or by bulk displacement effects. Third, it examines the role of processing by comparing different oxide and passivation routes. Fourth, it develops a compact modelling framework that transfers measured transistor degradation into a form usable for circuit prediction and radiation hardness analysis.

1.2.4 Scientific Novelty and Contribution

The contribution of the thesis lies in establishing a more realistic picture of radiation hardness in the described SiC bipolar platform. Rather than treating hardness as a single dose number, the work shows that the response is conditional and must be described as a function of irradiation state, dose rate, process choice, and temperature.

1. Experimental regime mapping (in-situ characterization): Conduct a series of irradiation experiments on SiC BJTs and logical inverters using gamma rays (^{60}Co) with continuous in-situ parameter monitoring. For the first time for this technology, a full factorial stress matrix was implemented:
    1. Bias: 0-bias, Active mode, cut-off/, saturation.
    2. Dose rate: high (HDR, >50 rad/s) vs. low (LDR, <0.1 rad/s) to verify the ELDRS effect.
    3. Temperature: Room (+25 °C) vs. Low (-70 °C).
2. Physical analysis of failure mechanisms: Separate the contribution of bulk and surface effects. Prove that the observed degradation of current gain (β) is driven by ionization processes at the emitter-base interface (spacer oxide), rather than bulk

displacement in the base. Link macroscopic changes in leakage currents to the kinetics of oxide charge accumulation and the generation of interface states.

3. Evaluation of technology and passivation role: Investigate the influence of interface chemistry on the radiation response. Compare standard thermal oxide with oxide formed by PECVD followed by nitridation. Verify the hypothesis that nitridation, while improving initial mobility, may introduce hidden instability under irradiation due to the presence of hydrogen bonds (Si-H).
4. Development of a predictive model (compact modeling): Create a macro-model for SPICE simulation, extending standard models (Gummel-Poon/VBIC) with radiation degradation equations.

1.2.5 Principal Findings

The principal finding of this thesis is that 4H-SiC bipolar electronics can exhibit substantial radiation tolerance, in some cases more than 10 times higher doses than silicon, but that this tolerance is not unconditional. The degradation observed in the studied BJTs and TTL inverters depends on the electrical state of the device during irradiation, on the dose rate, on the oxide/interface process, and on temperature.

For discrete BJTs, the dominant electrical signature of gamma irradiation is a reduction of current gain caused by increased base current. The degradation is most pronounced in operating regimes where radiation-generated charge can remain trapped near the emitter-base peripheral region and enhance surface recombination. This demonstrates that the relevant worst-case condition cannot be inferred solely from conventional MOS intuition and must be determined experimentally for the specific bipolar device structure.

For TTL inverters, the experiments show that device-level parameter drift translates into circuit-level changes in transfer behaviour and supply-current response. The circuit may remain functionally operational even when transistor parameters have measurably shifted, but the remaining design margin becomes state-dependent and must be assessed through circuit-level observables rather than by transistor gain alone.

The comparison between oxide/interface processes further shows that radiation response is strongly influenced by processing. This confirms that the radiation hardness of 4H-SiC bipolar technology is not only an intrinsic consequence of the SiC bulk material, but also an extrinsic property of the full device stack.

The low-temperature irradiation results indicate that reduced thermal activation and suppressed annealing can increase the apparent sensitivity of the devices. This is particularly relevant for cold-space operation, where long-duration exposure may occur under passive or weakly biased conditions.

Taken together, these findings support a qualification strategy in which SiC bipolar electronics are evaluated through bias-aware, dose-rate-aware, temperature-aware, and interface-aware testing, supported by compact modelling for circuit-level prediction.

1.3 Structure of the Thesis

The thesis is organized in seven chapters.

Chapter 1 . Introduction and Research Objectives

Introduces the technological motivation, formulates the central research questions, and positions the work within the broader development of 4H-SiC bipolar electronics for extreme environments.

Chapter 2. Radiation and its Effects on Materials

Provides the radiation-physics background required for the remainder of the thesis, including the classification of radiation fields, dosimetric quantities, interaction mechanisms, and the formal logic of radiation hardness assurance.

Chapter 3 4H-SiC Material and Devices and Interaction with Radiation

Reviews the relevant material properties of 4H-SiC, the operating principles of bipolar devices, and the physical mechanisms that govern their interaction with ionizing and non-ionizing radiation.

Chapter 4. Experimental Methodology, Test Setup and Parameter Extraction Routines

Describes the experimental methodology, including device technology, irradiation facilities, bias regimes, dosimetry, timing discipline, and parameter-extraction procedures.

Chapter 5 Experimental Results

Presents the main experimental and modeling results of the thesis, moving from discrete transistors to integrated bipolar circuits and compact SPICE representations.

Chapter 6 Discussion

Discusses the main results in a broader comparative framework, with particular emphasis on the conditional nature of radiation hardness in SiC and its implications for qualification-oriented testing.

Chapter 7 Conclusions

Summarizes the principal conclusions and outlines directions for future work.

Chapter 2. Radiation and Its Effects on Materials

2.1 Overview of Radiation Phenomena

This chapter summarizes the radiation-physics background required for the remainder of the thesis, with emphasis on ionizing radiation, dosimetry, interaction mechanisms, and radiation hardness assurance for semiconductor electronics.

2.1.1 Radiation

According to the definition of the International Atomic Energy Agency (IAEA), radiation is the emission and transfer of energy through space in the form of electromagnetic waves or submicroscopic particles [15]. In the context of this thesis, the key feature that distinguishes "radiation" from other wave phenomena is its ability to ionize matter - i.e., to remove electrons from atoms or molecules.

Radiation can be further categorized in electromagnetic waves (see Figure 2.1.1) and more particle-like entities with a mass, such as electrons, muons, protons and heavier ions. In this thesis we also consider neutrons as ionizing particles, although they interact only little with charged particles such as electrons, but may produce considerable ionization in secondary events.

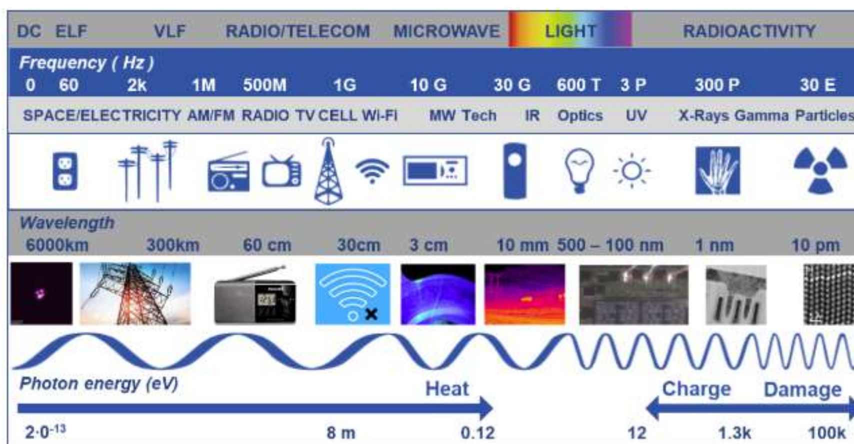

Figure 2.1.1. Electromagnetic spectrum , indicating the progression from low-energy radio-frequency radiation to high-energy X-rays and gamma rays.

There are two broad clusters of radiation: Non-ionizing and ionizing. The main difference between non-ionizing and ionizing radiation lies in their energy levels of the radiation particles and their ability to ionize atoms or molecules, which means to remove electrons from them, creating ions. The higher the particle energy (and the shorter the corresponding wavelength), the stronger its potential impact on the objects with which it interacts.

Non-ionizing radiation does not carry enough energy per quantum (photon/particle) to remove electrons from atoms or molecules and ionize them. While it can cause molecules to vibrate and heat up, it generally does not produce ions or cause severe damage associated with ionizing radiation. However, excessive exposure to certain types of non-ionizing radiation can still lead to some issues, such as UV overexposure, modification of polymers at the microscale and burns.

Figure 2.1.1 shows non-ionizing electromagnetic (EM) radiation, including: *Radio waves* used for radio and television broadcasting, with long wavelengths in the electromagnetic spectrum, *Microwaves* used in microwave ovens and for mobile phone signals,

Infrared radiation (IR), which is electromagnetic radiation with wavelengths longer than visible light, also referred to as heat, visible light which is the small portion of the electromagnetic spectrum visible to the human eye, Ultraviolet (UV) light, a part of the electromagnetic spectrum just beyond the violet end of visible light. UV radiation contains sufficient energy to burn human skin and even cause cancer at excessive exposure. UV light can also cause ionization but is most often considered as non-ionizing radiation due to the relatively low energy.

Ionizing radiation has enough energy to remove also more tightly bound electrons from atoms, thus changing the atomic and electronic structure of matter. For historic reasons, ionizing radiation is divided into: Alpha particles (He^{2+}), i.e. helium nuclei, consisting of two protons and two neutrons, for instance emitted in nuclear reactions, Beta particles (β^-), which are high-energy electrons or positrons emitted from radioactive nuclei, and X-rays and Gamma rays(γ), which is high-energy electromagnetic waves. Today these waves, or particles can also be produced in a controlled way, and the different types of ionizing particles also involve energetic protons, heavier ions, elementary particles and neutrons.

Particles with higher (kinetic) energy can penetrate deeper and are potentially more harmful than lower energy particles. The energy loss of the particles also depends on how strongly the particle interacts with the medium it penetrates, which varies with velocity, mass and charge state, often in a non-linear way. Figure 2.1.2 shows the penetrating ability for typical particles and rays in the MeV range (X-rays are typically in the keV range).

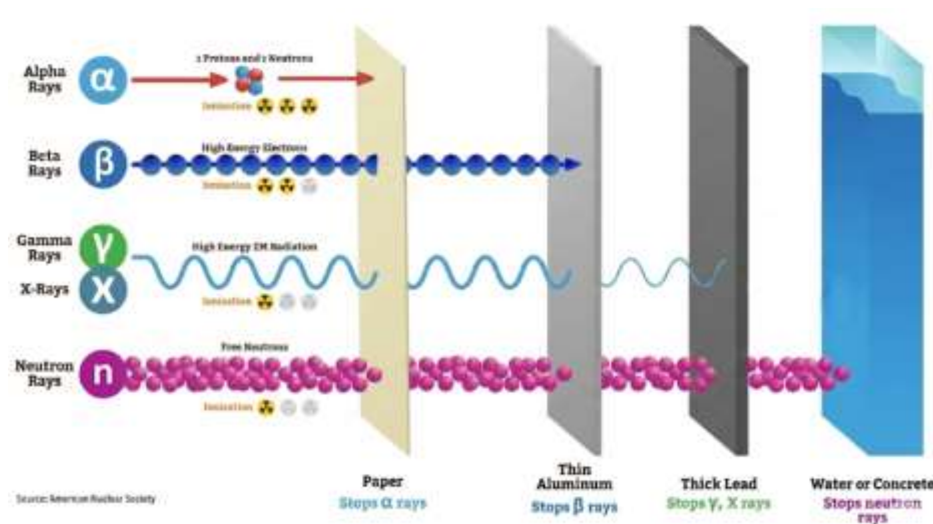

Figure 2.1.2. Schematic comparison of the penetrating ability of alpha particles, beta particles, gamma photons/X-rays, and neutrons in representative shielding media.

There is no specific physical meaning in the historical naming of the radiation types beyond historical convention. Hence there should be some clarifications made. Alpha, beta, and neutron sources are particle fluxes with continuous or discrete spectra and are not the primary focus of this thesis. Gamma radiation is considered in more detail later in its application to semiconductor materials and devices.

2.1.2 Metrology and Unit Systems in Radiation Physics

In the context of radiation testing of semiconductor electronics (radiation hardness assurance, RHA), it is critically important to clearly distinguish between concepts describing the radiation field and concepts describing the material response. The historically established duality of unit systems (SI versus non-SI units, more frequently used in the United States and in a number of industry standards) requires precise definitions in order to avoid errors in interpreting experimental data [15-18].

2.1.2.1 Source Activity: Becquerel and Curie

The activity of a radionuclide source (e.g., ^{60}Co or ^{137}Cs) characterizes the decay rate per unit time, but it does not directly define the impact on the test object.

- Becquerel (Bq): The SI unit equal to one decay per second (s^{-1}).
- Curie (Ci): A non-SI unit historically linked to the activity of 1 gram of ^{226}Ra.

$$1\ \mathrm{Ci} = 3.7 \times 10^{10}\ \mathrm{Bq}$$

2.1.2.2 Exposure Dose: Roentgen

The concept of exposure describes the ionizing ability of X-ray or gamma radiation only in dry atmospheric air [16,17].

- Roentgen (R): a historical unit of exposure for X-rays and gamma radiation in air, defined as

$$1\ \mathrm{R} = 2.58 \times 10^{-4}\ \mathrm{C/kg\ of\ dry\ air.}$$

- Limitation: Using roentgens to describe the effect on semiconductors (Si, SiC) is physically incorrect without appropriate conversion factors, because absorption cross-sections in silicon/carbon and in air (nitrogen/oxygen) are different.

2.1.2.3 Absorbed Dose: Gray and Rad

The fundamental quantity governing radiation degradation of a material (defect generation and dielectric charging) is the absorbed dose – energy dE deposited in a mass dm [16-18].

$$\text{Gray (Gy): SI unit, } 1\ \text{Gy} = 1\ \text{J/kg}.$$

Rad (rad): Traditional unit (radiation absorbed dose) expressed in the CGS system, widely used in MIL-STD (military standards) and in the space industry.

$$1\ \text{Gy} = 100\ \text{rad}$$

Important: Dose must always be specified for the absorber material, e.g., rad$_{(Si)}$ or rad$_{(SiO_2)}$. To convert dose in air (exposure X in roentgens) to dose in a medium (D in rads), the following relation is used:

$$D_{med} = f_{med} \cdot X,$$

where f_{med} is a conversion factor that depends on photon energy and the atomic number Z of the material. For ^{60}Co and silicon, $f_{Si} \approx 0.87$.

There is also a unit for absorbed dose in biological material, derived in the SI system, the Sievert (Sv), where 1 Sv represents the equivalent biological effect of the deposit of a joule of radiation energy in a kilogram of human tissue [16,18].

Any electronic system operates under natural background radiation. For radiation-hardness studies (where doses are in kilograys), the natural background (milligrays) is negligible; however, understanding it is useful for calibration and for assessing storage conditions.

At sea level, the background radiation consists of several components summarized in Table 2.1.

Table 2.1. Components of annual effective dose from natural background radiation (sea level) [18, 19]

Radiation source	Contribution (mSv/year)	Radiation type	Comment
Radon (Rn) and Thoron(Tn)	**0.5 – 2.0**	**Alpha radiation**	**Main contributor to biological dose**
Cosmic radiation	**~0.3 (sea level)**	**Mixed field (mainly muons, neutrons, and gamma rays)**	**Increases with altitude**
Terrestrial radiation	**0.3 – 0.6**	**Gamma radiation**	**External gamma dose from ^{40}K and ^{238}U the and ^{232}Th**
Internal exposure	**~0.3**	**Mainly beta and gamma radiation**	**Isotopes in materials (e.g., ^{40}K and ^{14}C)**

The situation changes significantly with increasing altitude. The atmosphere acts as a natural shield that absorbs cosmic particles. As altitude increases, atmospheric density decreases and the ionization rate rises, reaching a maximum (the Pfotzer maximum) at about 15–20 km (Figure 2.1.3) [20-23].

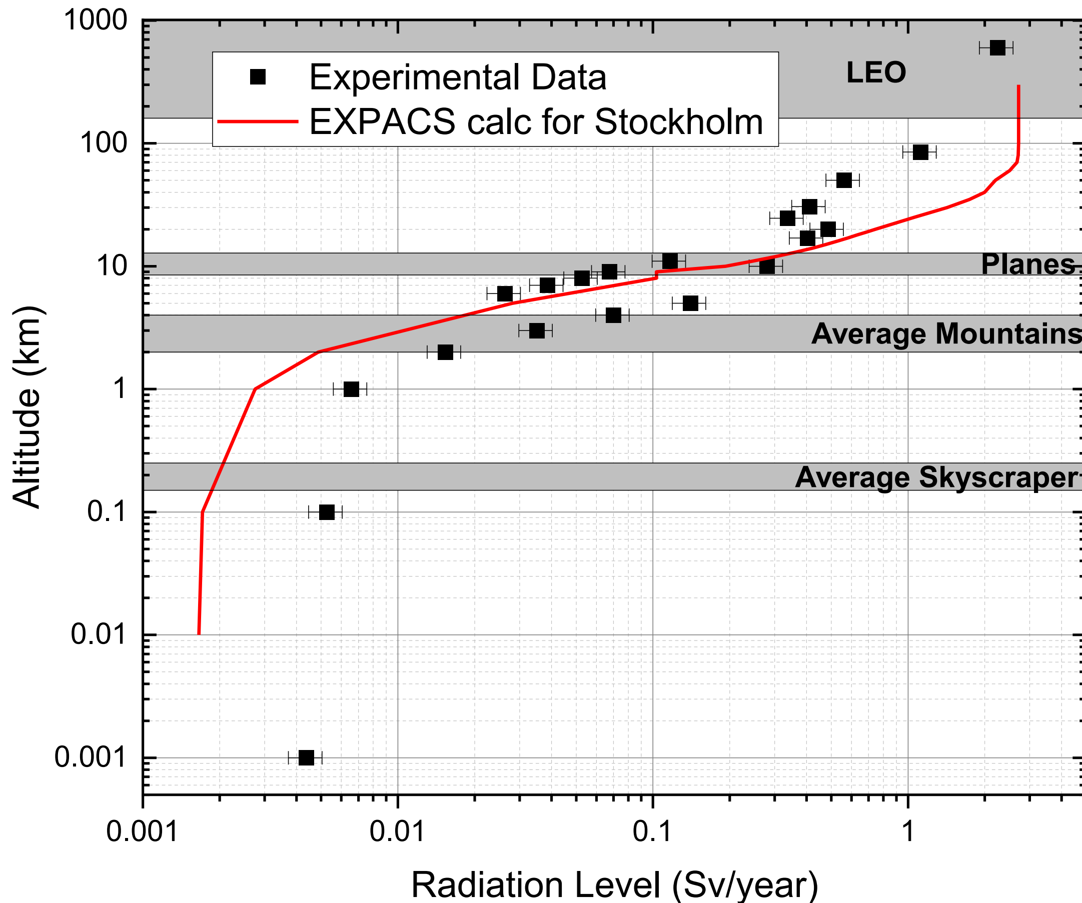

Figure 2.1.3. Altitude dependence of the annual cosmic-radiation dose equivalent: experimental data and EXPACS calculation for Stockholm.

Although radiation hardness assurance is usually formulated in terms such as procedures, margins, and acceptance logic, its physical basis depends on the damage metric used for a given failure mode. For displacement-damage assessment, one of the most informative comparative quantities is the non-ionizing energy loss (NIEL), which describes the fraction of incident particle energy transferred into atomic displacements rather than ionization.

Figure 2.1.3 therefore serves as a materials-level complement to the standards discussion above: it illustrates how the displacement-damage response of Si and 4H-SiC varies with particle energy and how a fixed particle fluence maps into an equivalent damage dose. The comparison is important because it shows that Si-based qualification intuition cannot be transferred to SiC without explicit validation of the relevant damage function.

In regions exceeding 100 kilometers above the Earth's surface, the variability in radiation models intensifies, predominantly as a consequence of the heterogeneous distribution of

radiation particles by volume. This heterogeneity renders the generation of accurate approximations challenging. Consequently, for altitudes substantially greater than 100 kilometers, the radiation models delineated in the subsequent sections are deemed to be more pertinent and reliable.

For spacecraft in orbit (altitudes > 100 km), the concept of "background" changes into a harsh environment dominated by radiation belts and solar events.

2.1.3 Atmospheric Shielding and the Radiation Cascade

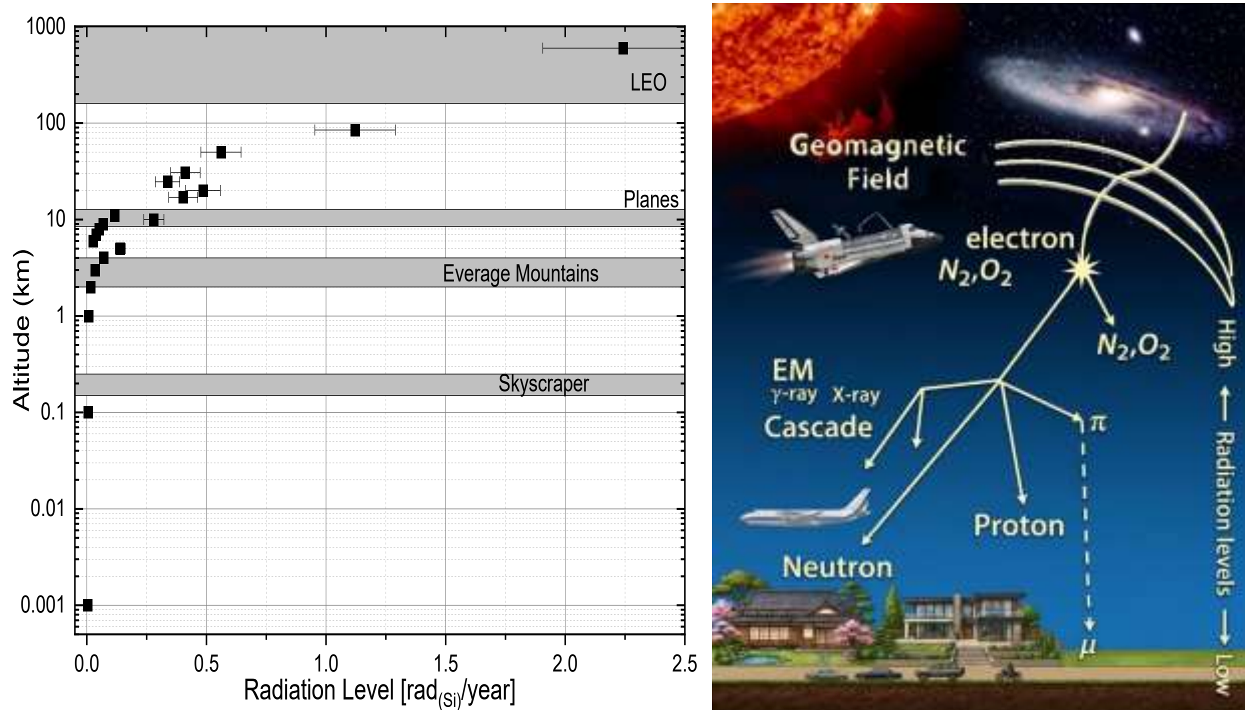

Figure 2.1.4. Atmospheric shielding and radiation cascade driven by solar energetic particles and galactic cosmic rays. Left: altitude dependence of the annual radiation level, illustrating the transition from ground-level exposure to mountain, aviation, and low-Earth-orbit conditions. Right: schematic representation of the atmospheric cascade produced when primary high-energy particles interact with N2 and O2 molecules, generating secondary photons, electrons, protons, neutrons, pions, and muons.

As depicted in Figure 2.1.4 the Earth's geomagnetic field and atmospheric layer act as a dual macroscopic shield against the primary influx of Galactic cosmic rays (GCR) and Solar solar energetic particles (SEP). Above 100 km spacecraft and their onboard electronics are exposed directly to these primary high-energy protons and heavy ions, alongside dense fluxes of electrons trapped in the Van Allen belts. In this exo-atmospheric regime, these primary particles and trapped electrons are the absolute dominant contributors to the total ionizing dose (TID), causing rapid charge buildup in semiconductor dielectrics and profound structural degradation [20,21,23].

As primary particles penetrate deeper into the atmosphere, they undergo spallation reactions with the atomic nuclei of nitrogen (N_2) and oxygen (O_2) gas molecules, initiating a complex, branching secondary shower. This cascade comprises both an

electromagnetic component (electrons, X-rays, and γ-rays) and a hadronic component (secondary protons, neutrons, pions (π), and muons (μ). While the overall radiation flux drops exponentially closer to the Earth's surface, the compositional profile shifts dramatically. At commercial aviation altitudes (10–12 km), the highly penetrating secondary neutrons and muons become the prevalent concern. Unlike the LEO environment, where TID is the primary failure driver, the radiation threat at these mid-altitudes shifts predominantly toward single event effects (SEE) induced by neutron collisions with the nuclei of semiconductors, or other materials, while their contribution to cumulative TID remains negligible[20, 21].

2.1.3.1 Synergistic Environmental Stressors in Space Operations

Beyond the purely ionizing radiation landscape, the operational environment above 100 km introduces a convergence of aggressive physical and chemical factors that synergistically accelerate device degradation. Electronic packaging and exposed semiconductor interfaces must survive a profoundly hostile multi-physics environment:

- Atomic oxygen and radical degradation: In LEO, the highly rarefied atmosphere is dominated by atomic oxygen (ATOX) and aggressive ozone radicals created by the photodissociation of residual O2 under intense UV irradiation. These highly reactive species aggressively oxidize exposed surfaces, leading to severe chemical corrosion and mass-loss erosion of polymeric passivations (such as polyimides), protective coatings, and metallic contacts.
- Deep vacuum and outgassing: The extreme vacuum conditions ($< 10^{-6}$ Torr) fundamentally alter material stability, promoting the continuous outgassing of volatile organic compounds from packaging resins and thermal interface materials. This not only degrades the mechanical integrity of the host material but also risks contaminating adjacent optical and sensitive semiconductor surfaces.
- Extreme thermal cycling: The absence of convective heat transfer in a vacuum means spacecraft are subjected to violent thermal shocks as they transit between direct solar illumination and planetary eclipse. Surface and junction temperatures can rapidly cycle between -150°C and +150°C. This induces profound thermomechanical stress and continuous interfacial fatigue.

When coupled together, the radiation-induced embrittlement of dielectrics (TID case), localized lattice damage (DD), ATOX-driven surface erosion, and unrelenting thermal fatigue create a compounding degradation matrix. Consequently, ensuring the reliability of wide-bandgap electronics in these altitudes requires moving beyond mere radiation shielding to holistic, multi-environmental robust design strategies [24, 25].

2.1.3.2 Analysis of Radiation Environments

To provide a comprehensive perspective on the scale of these environments, Figure 2.1.5 illustrates the dynamic ranges of X-ray and gamma radiation exposure dose rates (in rad/s) across different natural, industrial, and scientific settings.

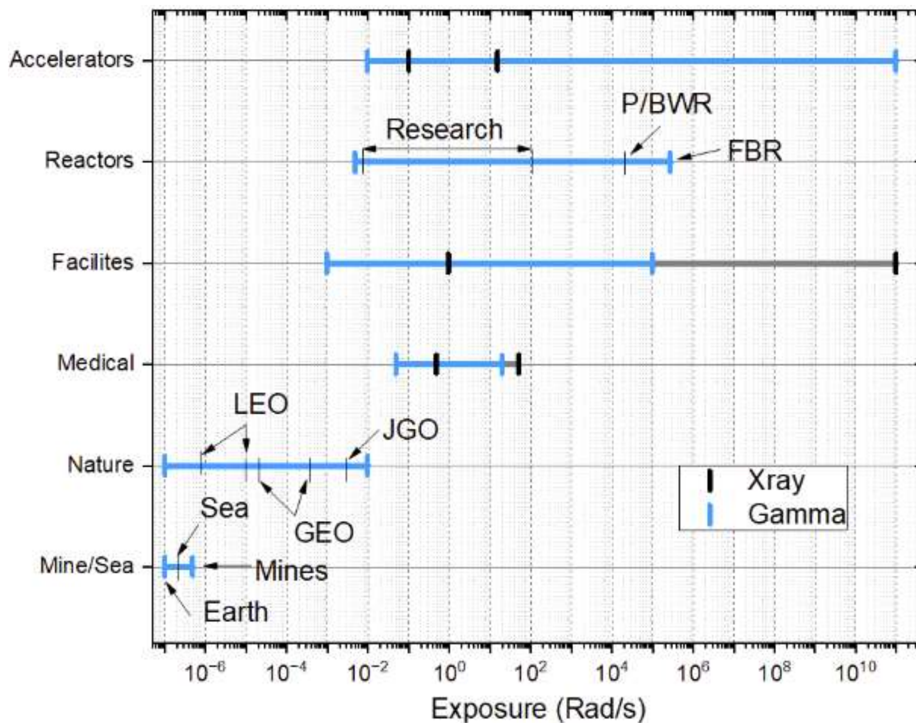

Figure 2.1.5. Comparison of typical X-ray and gamma-ray exposure rates across different environments.

The data reveals a staggering difference of over 18 orders of magnitude:

1. Natural background (mine/sea/Earth): Minimum radiation levels (from 10^{-7} to 10^{-5} rad/s) are observed on the Earth's surface, in oceans, and in mines. This baseline background causes no noticeable degradation in electronic materials.
2. Space environment (Nature): Upon entering near-Earth orbits, the radiation load increases. In LEO and geosynchronous equatorial orbit (GEO), gamma radiation dose rates rise significantly, reaching peak values around 10^{-2} rad/s in extreme environments such as the Jovian system (JGO).
3. Medical & industrial facilities: The controlled use of ionizing radiation involves localized exposure in the range of 10^{-1} to 10^{2} rad/s.
4. Nuclear reactors: Within the active zones, radiation levels are orders of magnitude higher. Research reactors generate dose rates up to 10^{2} rad/s, while commercial pressurized/boiling water reactors (P/BWR) and fast breeder reactors (FBR) create exceptionally harsh conditions with gamma levels exceeding 10^{5} rad/s.
5. Accelerators and specialized facilities: These exhibit the most extreme ranges. Depending on the operational mode, pulsed X-ray and gamma radiation levels can reach peak transient values up to 10^{11} rad/s.

Consequently, while terrestrial applications rarely face radiation degradation, designing electronics particularly wide-bandgap semiconductors like 4H-SiC for space, nuclear, and accelerator applications mandates rigorous structural design and testing.

2.1.4 Mechanisms of Gamma-Photon Interaction with Semiconductor Structures

When gamma radiation passes through matter, photon interactions with atoms, atomic nuclei, and electrons, depend strongly on the photon energy. The amount of energy that remains in the material and is transferred into ionization is described by the more continuous attenuation process, while the physical interaction channels are described by absorption processes.

These two concepts are fundamental for understanding radiation effects in semiconductors.

2.1.4.1 Attenuation

Photon penetration in matter is governed statistically by the probability per unit path length that a photon interacts via one physical process or another. This probability is described by the linear attenuation coefficient (μ) [1/cm]. A more convenient quantity is the mass attenuation coefficient (μ/ρ) [cm^2/g], which represents the probability of photon–matter interaction per unit mass thickness traversed.

The first step in evaluating photon-induced ionization is to compare how efficiently different device and shielding materials attenuate photons as a function of energy. Figure 2.1.6 shows representative mass attenuation coefficients for materials commonly encountered in semiconductor devices and packages.

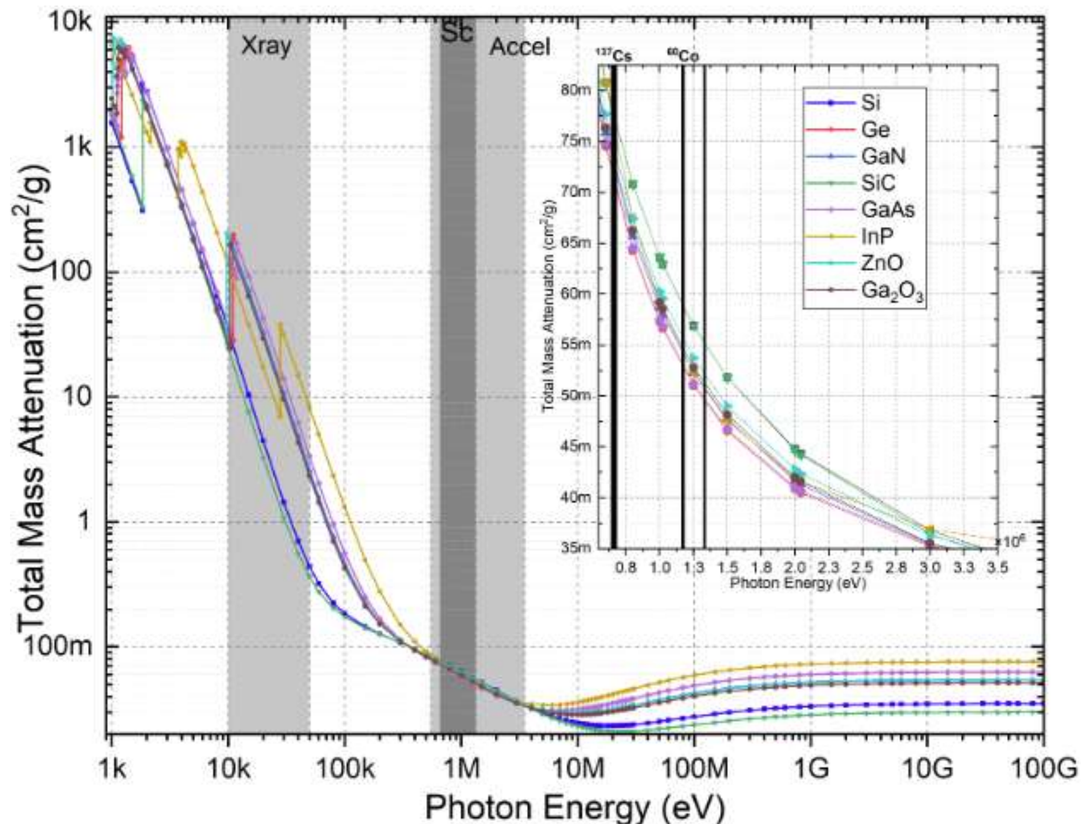

Figure 2.1.6. Attenuation coefficients for materials commonly used in the semiconductor industry.

The grey vertical regions indicate characteristic photon-energy ranges associated with commonly used irradiation sources. The X-ray region corresponds to conventional X-ray tubes operating in the keV range. The Sc region (dark grey area at Fig 2.1.6) corresponds to radionuclide gamma-ray sources, primarily ^{60}Co and ^{137}Cs. The Accel region denotes accelerator-based photon sources, including different classes of electron and photon accelerators depending on their configuration.

In the energy range from about 0.7 to 1.4 MeV, the attenuation coefficients of many semiconductor materials are relatively small and vary only moderately. Nevertheless, it is well known from both published studies and experimental practice that semiconductor devices fabricated with similar topologies and nominally comparable technologies may still exhibit markedly different radiation hardness. This discrepancy arises because the device response is determined not only by bulk photon attenuation, but also by the spatial distribution of absorbed energy, the efficiency of ionization and charge generation, and the susceptibility of dielectrics, interfaces, and active regions to charge trapping and radiation-induced defect formation.

2.1.4.2 Absorption

Gamma radiation is indirectly ionizing. The primary interaction of a photon with the crystal lattice or a dielectric generates high-energy secondary electrons. These electrons, while slowing down in the material, create cascades of ionization (electron–hole pair generation) and, to a lesser extent, lattice defects.

Three dominant interaction mechanisms are usually distinguished. Their probability (cross-section, σ) depends on photon energy E_γ and the target atomic number Z:

Several interaction channels for gamma radiation in matter are commonly cited, including the photoelectric effect (photo), Compton scattering (comp), electron–positron pair formation (pair), coherent scattering (coh), and the nuclear photoelectric effect (nuc). The total photoabsorption cross-section can be expressed as the sum of these contributions, as shown below:

$$\frac{\mu_{tr}}{\rho} = \frac{f_{pe} \cdot \sigma_{pe} + f_{incoh} \cdot \sigma_{incoh} + f_{pair} \cdot \sigma_{pair} + f_{coh} \cdot \sigma_{coh} + f_{nuc} \cdot \sigma_{nuc}}{u \cdot A}$$

Here, f are the factors representing the average fractions of photon energy transferred into the kinetic energy of charged particles in each interaction type [26]. u – molar mass; ρ –mass density of the absorber material; A – relative atomic mass of the target element. As illustrated, the relative contribution of each mechanism strongly depends on photon energy

2.1.4.3 Electron–Hole Pair Generation

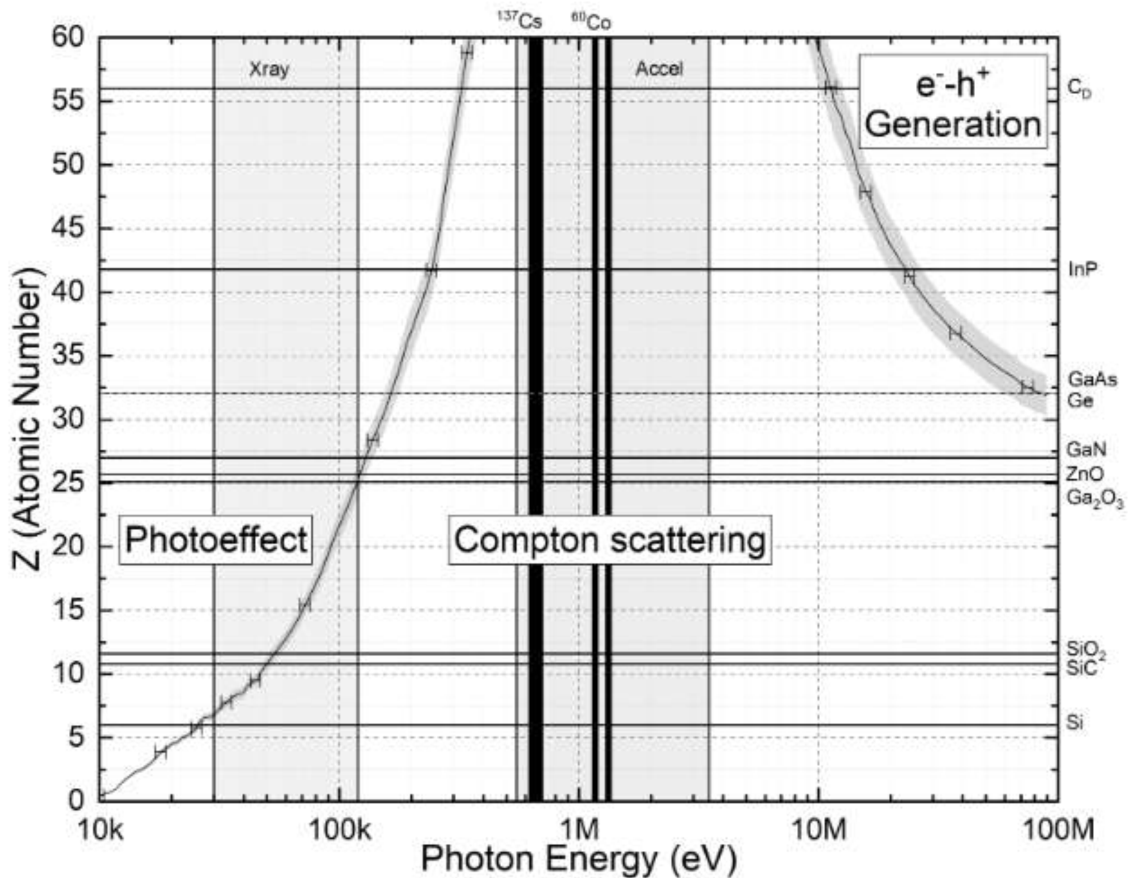

Figure 2.1.7. Total photon absorption cross-section as a function of energy for different materials.

In semiconductors, the absorbed photon energy is not converted into mobile charge carriers with an efficiency equal to the bandgap alone. Instead, the average energy required to generate one electron–hole pair is several times larger than the bandgap because a substantial fraction of the deposited energy is dissipated through phonons and secondary excitations. This quantity is material dependent and is of direct importance for radiation electronics: for the same absorbed dose, a material with a larger electron–hole pair creation energy generates a lower initial carrier density and therefore a lower transient photocurrent. This point is particularly important for 4H-SiC, whose reduced initial charge yield is one of the physical reasons for its improved tolerance to ionization-driven perturbations relative to silicon.

It is important to acknowledge that in actual space gamma radiation has distributed spectral characteristics, not monochromatic (or narrow spectra) as typically employed in laboratory settings. Consequently, the complexity and interaction of processes in natural space conditions significantly surpass the scenarios replicated during verification testing, introducing a higher degree of variability and complexity.

Figure 2.1.8 illustrates qualitatively the difference between the photoelectric effect, electron positron pair production, and Compton scattering and the resulting secondary electron populations (RSE):

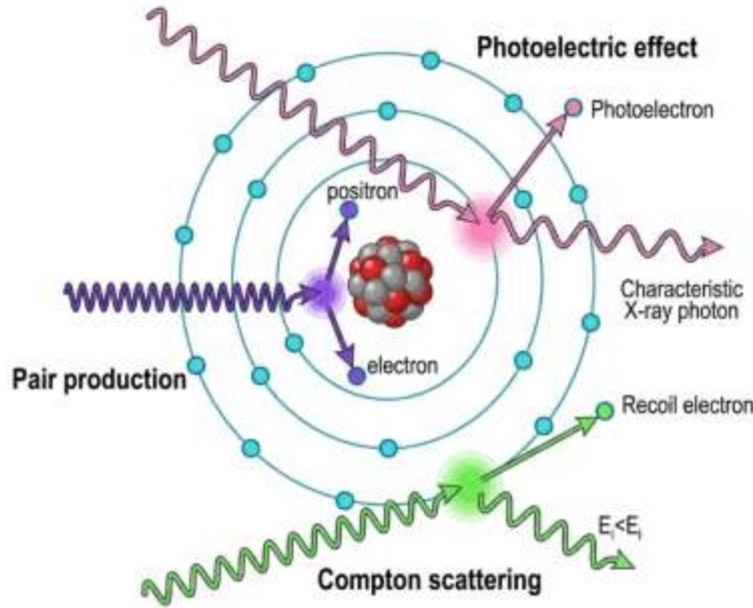

Figure 2.1.8. Comparison of secondary electron populations generated by the photoelectric effect, Compton scattering, and pair production.

2.1.4.3.1 Photoelectric Effect

At low photon energies, the dominant process is full absorption of the gamma quantum by a bound electron (typically from the K-shell), followed by electron emission. The energy balance could be described by the eq $E_e = h\nu - E_b$ where E_b is the binding energy of the electron and $h\nu$ is the incident photon energy. The cross-section dependence, σ_{ph}, decreases sharply with increasing energy and strongly depends on nuclear charge:

$$\sigma_{ph} \propto \frac{Z^n}{(h\nu)^3}, \quad n \approx 4 \dots 5$$

Since SiC is a "lighter" material ($Z_{eff} \approx 10$) than silicon ($Z = 14$), the photoelectric cross-section in SiC is lower.

Another effect is the secondary relaxation. The inner-shell vacancy is filled by an outer electron, producing either characteristic X-ray emission (fluorescence) or an Auger electron.

2.1.4.3.2 Compton Scattering

In the intermediate energy range (for Si and SiC, roughly ~ 100 keV to 10 MeV), the dominant mechanism is inelastic scattering of photons on weakly bound (valence) electrons. The photon transfers part of its energy to a recoil electron and is scattered with increased wavelength λ'. The Compton wavelength shift is described by eq:

$$\Delta\lambda = \lambda' - \lambda = \frac{h}{m_e c}(1 - \cos\theta)$$

where $m_e$is the electron rest mass, $h$is Planck's constant, c is the speed of light in vacuum, and $\theta$is the photon scattering angle.

It is good to note that for standard ^{60}Co sources (1.17 and 1.33 MeV), Compton scattering largely determines the generation of secondary electrons in the semiconductor volume. The cross-section, σ_c, scales approximately with Z (number of electrons), so the difference between Si and SiC is less pronounced than for the photoelectric effect.

Although Compton scattering is primarily treated as an ionization mechanism, sufficiently energetic secondary electrons can also induce DD (displacement damage). In silicon, the generation of Frenkel pairs by electrons requires electron energies above approximately 260 keV. Therefore, under ^{60}Co γ-irradiation, DD arises mainly from Compton electrons with energies of a few hundred keV up to about 1 MeV. Since the electron energy remains well below the $\sim$ 8 MeV threshold required for divacancy and larger cluster formation in Si, the resulting damage is dominated by isolated point defects rather than defect clusters.

2.1.4.3.3 Electron–Positron Pair Production

For photon energies above twice the electron rest energy ($E_\gamma > 2m_ec^2 \approx 1.022$ MeV), conversion of photon energy into an electron–positron pair becomes possible in the Coulomb field of a nucleus.

An electron–positron pair is created, and the excess energy becomes kinetic energy:

$$E_{kin} = h\nu - 1.022\,\text{MeV}.$$

In terms of dosimetry for the ^{60}Co spectrum, this contribution is limited, but it becomes significant for high-energy bremsstrahlung radiation (typically produced in accelerators). The cross-section scales as $\sigma_{pp} \propto Z^2$, making it important in heavy shielding materials (W, Pb), but less important for the SiC crystal itself.

2.2. Spectral Composition and Particle Nature

This thesis deals with the radiation hardness of integrated electronics based on 4H-SiC and attempts to quantify the ability of such devices to withstand the radiation environment during operation in space. In the following subsection, the radiation fields present in various parts of space will be described.

The radiation environment in near-Earth space is determined by a complex superposition of charged-particle fluxes of different origins and by the stochastic dynamics of solar activity. A basic classification of ionizing radiation sources in space includes three components originating from various parts of space: galactic cosmic rays (GCR) from outside the Solar System, solar cosmic rays (SCR) from our Sun, and particles trapped in Earth's radiation belts (ERB) [27]. A fundamental parameter that controls the flux density of high-energy particles is the 11-year solar activity cycle (the Schwabe cycle). The intensity of galactic cosmic rays arriving from the interstellar medium is strongly anti-correlated with the sunspot number (Wolf number).

2.1.4.3 Physical Mechanism of Modulation

During solar maximum, the intensified solar wind and the expansion of the turbulent heliospheric magnetic field create an effective potential barrier. This barrier scatters the low-energy component of GCR (up to ~1–10 GeV), limiting its penetration into the inner Solar System (the Forbush effect).

In contrast, during solar minimum ("quiet Sun"), the shielding weakens and the GCR flux reaches peak values. This creates critical conditions for long-duration missions, because heavy GCR ions have the highest linear energy transfer (LET).

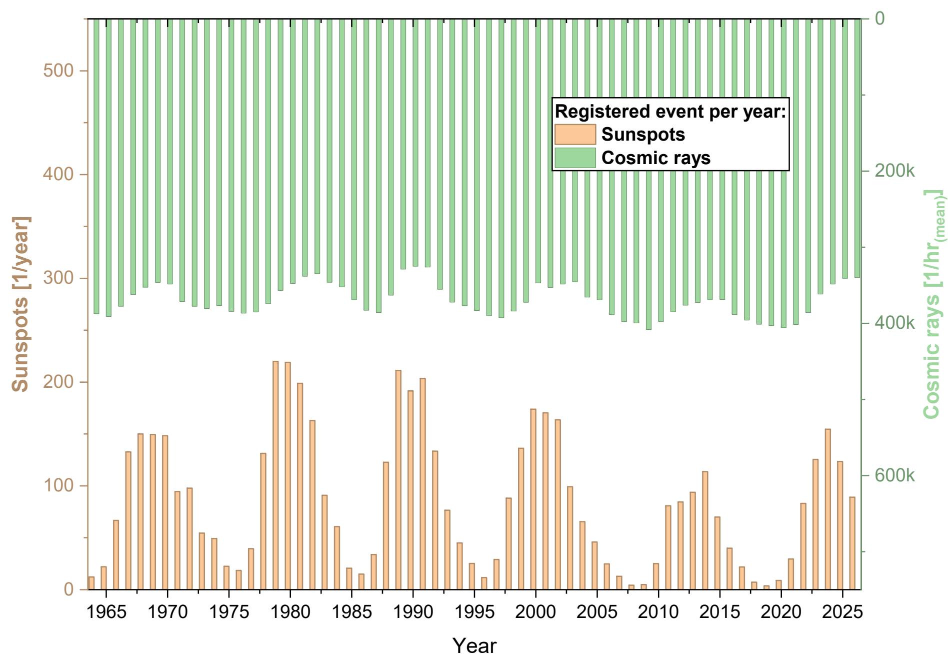

Figure 2.2.1 shows this temporal modulation and illustrates why the solar-cycle phase is a first-order input for long-duration mission dose estimates [data is provided by CRII].

2.2.1 Galactic Cosmic Rays (GCR)

GCR is an isotropic flux of nuclei accelerated to relativistic velocities. According to modern astrophysical models, the dominant acceleration mechanism is diffusive shock acceleration at supernova remnant shock waves, which can produce particle energies up to 10^{15}eV. [28]

The main constituents of this radiation are: Protons (~87%) form the baseline radiation background, alpha particles (~12%)-, Helium nuclei, and heavy ions (HZE, $Z > 2$, ~1%)- despite their low integral flux, iron-group ions (Fe) and other heavy elements dominate the probability of SEE because ionization losses scale approximately with the square of nuclear charge $dE/dx \propto Z^2$.[28]

2.2.2 Solar Cosmic Rays (SCR)

Unlike the quasi-stationary GCR flux, solar cosmic rays are produced sporadically during solar flares and coronal mass ejections (CMEs). The SCR energy spectrum is "softer"

(dominant energies < 100 MeV), but the peak proton flux can increase by 3–5 orders of magnitude over a short time (from hours to several days). For orbital systems, this is equivalent to a "shock" dose load that can degrade external coatings, optics, and solar arrays [25].

2.2.3 Geomagnetic Trapping and Earth's Radiation Belts

Earth's magnetic field captures charged particles and forms toroidal regions of enhanced radiation—the Van Allen radiation belts. This is shown in Figure 2.2.2 where the structure and population depend on geomagnetic latitude and altitude (the L-parameter) [24].

- Inner belt ($1.2 < L < 2.5$): A relatively stable region populated mainly by high-energy protons (up to hundreds of MeV), produced via decay of cosmic neutrons (the CRAND mechanism).
- Outer belt ($3 < L < 7$): A highly dynamic region dominated by energetic electrons (from hundreds of keV to several MeV). The outer-belt population can change sharply during geomagnetic storms, when particles are injected from the plasma sheet in the magnetotail.

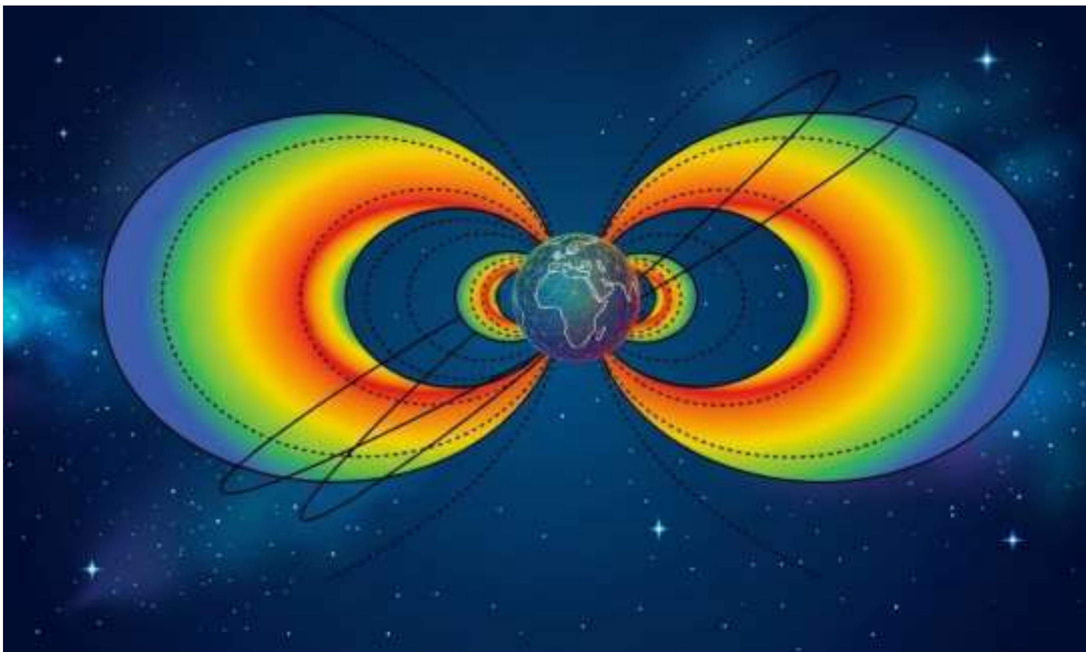

Figure 2.2.2. Structure of Earth's radiation belts, showing the proton inner belt and electron outer belt.

South Atlantic Anomaly (SAA) is a critically important feature for LEO spacecraft. Due to the offset of Earth's magnetic dipole center relative to the rotation axis and its tilt, the inner proton belt "dips" to altitudes of ~200 km in this region. When a spacecraft passes through the SAA, the rate of onboard electronic upsets increases sharply and the accumulated integral dose rises [24].

2.2.4 Electromagnetic Factors and Spacecraft Charging

In addition to particulate ionizing radiation, the reliability of onboard systems is influenced by electromagnetic compatibility (EMC) and charging effects caused by spacecraft interaction with the surrounding plasma.

Electrostatic charging (spacecraft charging) in vacuum and under exposure to space plasma, excess charge can accumulate on structural elements. Two main mechanisms are usually distinguished [29, 30].

First is surface charging dominant at geostationary orbit (GEO) and in polar regions of LEO. It is driven by competition between photoemission currents (due to solar UV) and currents from the ambient plasma (electrons and ions). In eclipse, orshadowed conditions, the spacecraft surface potential relative to the plasma can reach kilovolt levels (typically negative), creating a risk of electrostatic discharges (ESD) between elements with different conductivities (differential charging).

The second mechanism is deep dielectric (internal) charging: Caused by high-energy electrons ($E > 1$ MeV) from the outer radiation belt, which can penetrate shielding and deposit charge in dielectrics such as PCBs, cable insulation. Charge accumulation continues until the internal electric field exceeds the dielectric breakdown strength (typically $> 10^5$ V/cm), producing micro-breakdowns and induced disturbances in signal lines [19].

Naturally occurring electromagnetic interference, space weather, generates a wide range of electromagnetic disturbances:

- Solar radio bursts: Strong radio emission during flares can overlap operational bands of communication systems and GPS navigation, reducing the signal-to-noise ratio.
- Geomagnetic substorms: Magnetic-field variations induce currents in extended conductive structures (cables, solar panels), which must be considered in grounding and shielding design.

2.2.5 Specific Radiation Loads for Typical Orbits

The mission radiation profile depends strongly on orbit parameters: altitude, inclination, and the phase of the solar cycle.

For orbits at 400-1000 km altitude (LEO) with inclination $< 60°$, the dominant factor is passage through the South Atlantic Anomaly (SAA). In this region, a spacecraft periodically (up to several times per day) enters the inner radiation belt.

1. Spectrum: Mainly protons with energies up to hundreds of MeV.
2. Dynamics: Dose accumulates in discrete portions during SAA passages. Integral proton fluxes are relatively stable, but variations in atmospheric density can modulate low-energy particle populations. For polar LEO, an additional contribution comes from electron precipitation from the outer belt and from direct access of solar protons (SCR) near the magnetic poles (geomagnetic cutoff ≈ 0).

At ~36,000 km altitude (GEO), a spacecraft resides within the outer radiation belt.

3. Electron environment: Strong fluxes of electrons ($E \sim 0.1 - 10$ MeV), which can vary by 2–3 orders of magnitude within minutes during substorms. This creates extreme conditions for deep dielectric charging.

4. Proton environment: High-energy protons (GCR and SCR) have relatively free access to GEO because geomagnetic shielding is weak. During solar proton events (SPE), the proton flux can rise rapidly, threatening solar-array and optical degradation. Unlike LEO, GEO lacks the protection of a dense atmosphere and stronger magnetic shielding.

Interplanetary trajectories outside Earth's magnetosphere (deep space), shielding against GCR is essentially absent. The radiation background is dominated by continuous exposure to heavy galactic ions (an isotropic flux) and sporadic solar proton events. For missions to inner planets (e.g., Venus missions discussed by Neudeck et al.) [31], the increase in solar radiation intensity is proportional to $1/R^2$ and should be considered. It will increases both thermal and radiation loads (TID and instantaneous flux).

After identifying the main near-Earth radiation composition, it is useful to examine how shielding modifies their relative dose contribution. Figure 2.2.5 shows a schematic dose-depth dependence in which primary electrons are rapidly attenuated, while trapped protons and secondary bremsstrahlung remain relevant at larger shielding thicknesses.

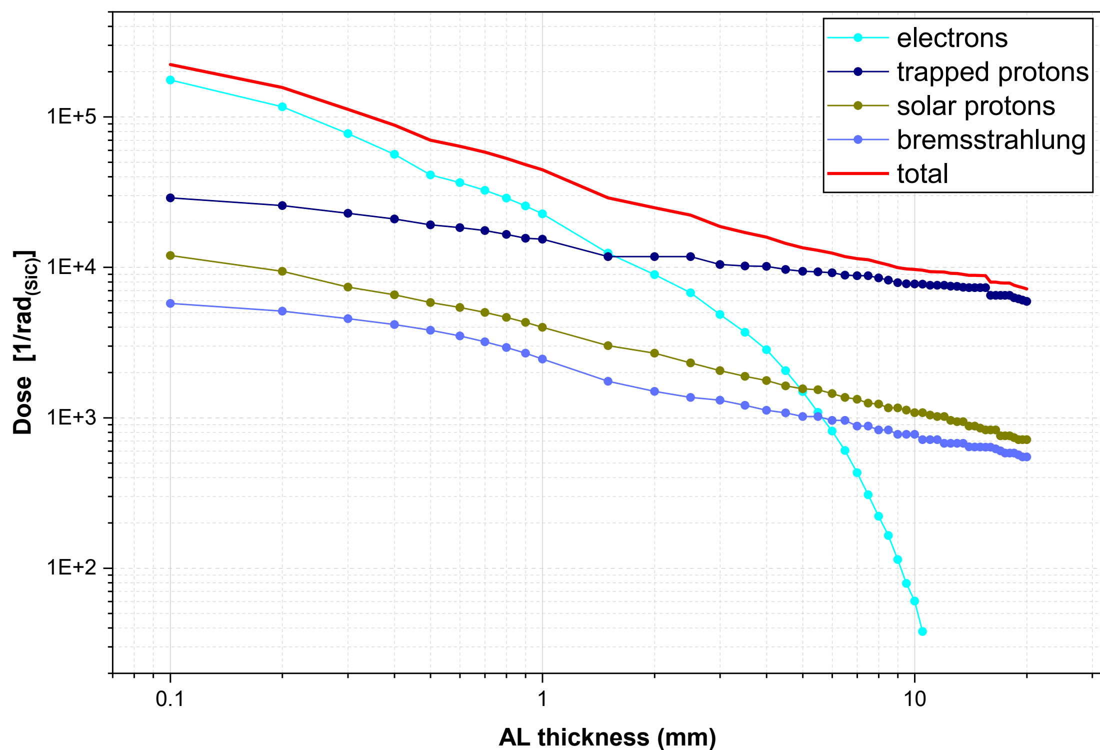

Figure 2.2.5. Schematic dose-depth dependence for representative near-Earth radiation components, adapted from standard SHIELDOSE/SPENVIS-type space-radiation analyses

Any electronic system on earth operates under natural background radiation, consisting mainly of radioactive nuclei and cosmic radiation penetrating the earth's atmosphere. For radiation hardness studies, where doses are typically in kiloGrays, the natural background in milliGrays is negligible; however, understanding the background radiation is useful for calibration and for assessing storage conditions.

2.2.6 Metrology of Radiation Effects: Fluence, Spectra, and LET

To quantitatively describe the radiation environment and to calculate hardware robustness, a set of radiometric and dosimetric quantities is used to characterize the energy and spatial parameters of radiation fields.

A basic characteristic of a radiation field is the particle flux density (flux), defined as the number of particles dN crossing an area element dA per time interval dt: $\varphi = d^2N/(dA \cdot dt)[cm^{-2} \cdot s^{-1}]$.The time integral of the flux over an exposure time T (e.g., spacecraft lifetime) gives the particle fluence $[1/cm^2]$. Real space-radiation fields are energetically non-uniform. Therefore, calculations use the differential energy spectrum, $d\varphi/dE$, which describes particle distribution over energy.

As first described by Niels Bohr, the energy loss of energetic particles can be described as an energy loss per unit pass length, dE/dx. This formulation is particularly useful for more massive particles such as ions, where the positive nucleus may be accompanied by a number of electrons. This occurs at lower ion energies when the velocity of the highly positive charged nucleus slows down and negative electrons from the surrounding media may "stick" to the ion and partly screen its charge. For even lower energies, the much heavier nucleus moves relatively slow compared to orbiting electrons and Bohr suggested that the energy loss then could be divided in two parts, one concerning the interaction of electrons in the medium and another part dealing with the interaction between the much more massive nuclei of the medium:

The "electronic" and "nuclear" energy losses are therefore very different. The total stopping power may be written as

$$\left(\frac{dE}{dx}\right)_{\text{total}} = \left(\frac{dE}{dx}\right)_{\text{el}} + \left(\frac{dE}{dx}\right)_{\text{nuc}}$$

The ionization and excitation of the electronic system are described by $\left(\frac{dE}{dx}\right)_{\text{el}}$ while collisions between nuclei, which lead to large momentum transfer, are described by $\left(\frac{dE}{dx}\right)_{\text{nucl}}$.

Nuclear collisions induce directional changes of the particle, as well as displacements and motion of the atoms of the medium. For higher energy ions the nuclear, or elastic, part of the energy transferred from the particle to the stopping media is relatively small, but may cause substantial damage in a solid, such as a crystalline semiconductor.

A key parameter for analyzing SEE is LET. It describes the ionization density along a charged-particle track and is numerically equal to the average energy lost in ionization, dE, per path length dl, normalized to the material density ρ: $LET = \frac{1}{\rho}\frac{dE}{dl}$ $[\text{MeV} \cdot \text{cm}^2/\text{mg}]$

The depth dependence of ionization losses is often described by the Bragg curve. As particles, particularly more massive ones such as ions, slows down in matter, its velocity decreases and the interaction cross-section will also increase, leading to a sharp peak in energy deposition (the Bragg peak) just before the particle stops.

2.2.5 Secondary Radiation and Spectral Transformation Behind Shielding

When primary space radiation interacts with structural materials, e.g.Al, Ti, composites, of the spacecraft, secondary particles and radiation are generated, which can significantly modify the local radiation environment inside the instrument compartment.

- Bremsstrahlung: When high-energy electrons decelerate in high atomic-number (Z) materials (e.g., IC packages, tantalum or tungsten shields), gamma photons are produced. In GEO, secondary bremsstrahlung can become a dominant contributor to the accumulated dose inside heavily shielded volumes, because it is more penetrating than the primary electrons.
- Nuclear reactions: High-energy GCR and SCR protons can induce spallation reactions in the nuclei of shielding materials and in the semiconductor itself. Reaction products (recoil nuclei, alpha particles) have high LET and can trigger SEE even when the primary radiation is not sufficiently ionizing. Secondary neutrons, being uncharged, penetrate deeply and create additional displacement damage centers [8].

2.3 Requirements for Semiconductor Devices in Space Applications

2.3.1 Radiation Hardness Assurance Concept and Design Margins

Qualification of semiconductor devices for space applications (space qualification) is not merely a series of tests, but a comprehensive, system-level process governed by radiation hardness assurance (RHA) standards. Unlike exploratory physics experiments that aim to identify ultimate degradation limits, the purpose of RHA is to statistically demonstrate that the probability of system failure over the mission lifetime will not exceed a specified reliability level [32].In this section, the most relevant standards for qualification of space electronics are briefly described.

A fundamental requirement common to the qualification practices of major space agencies, including the National Aeronautics and Space Administration (NASA), the European Space Agency (ESA), and the Japan Aerospace Exploration Agency (JAXA), is the use of a radiation design margin (RDM).

RDM is defined as the ratio of the component's mean failure level to the predicted mission environment level, including an uncertainty factor for the environment models:

$$\mathrm{RDM} = \frac{\text{mean failure level}}{\mathrm{U} \cdot \text{predicted mission environment level}}$$

where U is the uncertainty factor of the environment models, typically assumed to be in the range 1.2–2.0 [6,33].

- For dose effects (TID/NIEL): Most standards, including the European ECSS-Q-ST-60-15C and U.S. guidelines, require a conservative design margin. [32].

- For single-event effects (SEE): Requirements are formulated in terms of the threshold LET. To avoid catastrophic failures, a typical requirement is a sufficiently high threshold LET, expressed in MeV·cm²/mg. [34].

Although radiation hardness assurance is usually formulated in terms of procedures, margins, and acceptance logic, its physical basis depends on the damage metric used for a given failure mode. For displacement-damage assessment, one of the most informative comparative quantities is NIEL, which describes the fraction of incident particle energy transferred into atomic displacements rather than ionization.

Figure 2.3.1 therefore serves as a materials-level complement to the standards discussion above: it illustrates how the displacement-damage response of Si and 4H-SiC varies with particle energy and how a fixed particle fluence maps into an equivalent damage dose. The comparison is important because it shows that Si-based qualification intuition cannot be transferred to SiC without explicit validation of the relevant damage function.

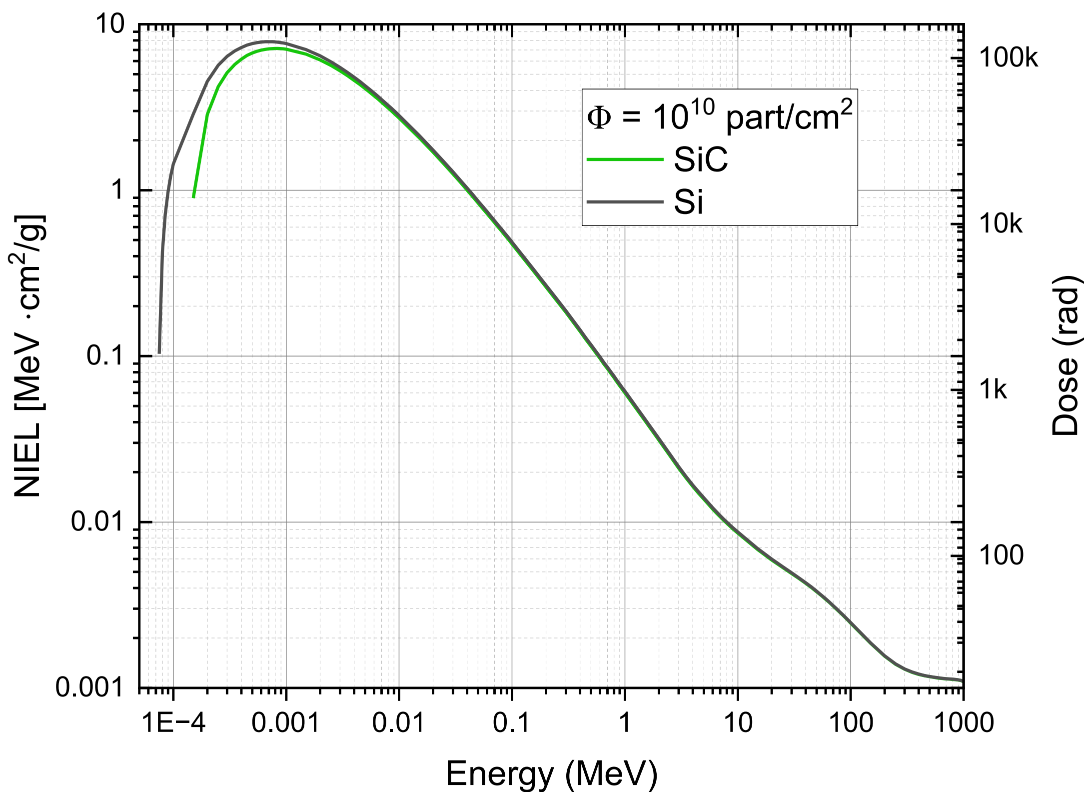

Figure 2.3.1. Energy dependence of NIEL in Si and 4H-SiC, with the right axis indicating the corresponding equivalent displacement-damage dose for an incident fluence of 10^{10} particles cm^{-2}.

2.3.2 U.S. Department of Defense (MIL-STD) and NASA Standards

The U.S. standards system is the historical foundation of global radiation-testing practice. It separates requirements for test procedures (test methods) from requirements for quality management and performance specifications.

2.3.2.1. MIL-STD-883 and MIL-STD-750: Test Methodology

MIL-STD-883, Method 1019 (Ionizing Radiation): Often considered the "gold standard" for ICs. A key feature of the latest revision (Method 1019.9) is strict control of irradiation conditions to reveal time-dependent effects.

- Condition A (High Dose Rate): Irradiation at 50–300 $rad_{(Si)}$/s. Intended to reveal oxide-trap effects, which dominate at high dose rate. A post-irradiation anneal is required to check for parameter "rebound" due to the growing contribution of interface states.
- Condition D (Low Dose Rate): Critically important for bipolar technologies. It requires irradiation at a very low dose rate to reveal. Studies indicate that bipolar SiC structures may exhibit specific sensitivity to low dose rate, especially at low temperatures, which makes this method relevant for space qualification [4, 5].

MIL-STD-750, Method 1080 (SEE): Defines testing of discrete semiconductor devices (including SiC power MOSFETs and diodes) for SEE. Special attention is given to catastrophic single-event burnout (SEB) and single-event gate rupture (SEGR), requiring a safe operating area (SOA) to be mapped in "drain–source voltage vs LET" coordinates [34].

2.3.2.2. NASA Project Specifications

For Class A missions (highest reliability, including crewed flights), NASA often applies stricter requirements than baseline MIL standards. - Goddard Space Flight Center (GSFC) EEE-INST-002: Requires radiation lot acceptance testing (RLAT) for each flight lot of components produced using commercial technologies (COTS). For SiC devices, where process-related oxide variability can still be significant, RLAT is a critical step [35].

2.3.3 European Standardization System

The European Space Agency (ESA) applies the harmonized European Cooperation for Space Standardization (ECSS) framework, which typically follows a more conservative "worst case analysis" approach than the NASA.

2.3.3.1 ECSS-Q-ST-60-15C: Radiation Hardness Assurance

This standard defines requirements for risk management. Components are classified into three groups: qualified/radiation-hard with available RHA data, requiring testing. For power devices, the standard introduces strict voltage-derating requirements. For example, to mitigate SEB/SEGR under heavy ion bombardment, the maximum operating voltage is often limited to 50–75% of the rated breakdown voltage, and this must be experimentally validated for the relevant LET spectrum [36].

2.3.3.2 ESCC Basic Specification No. 22900 (TID Test Method)

This is comparable to MIL-STD-883 but includes differences relevant to wide-bandgap semiconductors: ESCC requires electrical measurements within 1 hour after each irradiation

step (versus 2 hours in MIL-STD), which reduces uncontrolled annealing of unstable defects in SiC oxides. Temperature considerations: ESCC 22900 explicitly recommends irradiation at elevated temperatures when this matches mission operating conditions. This is important for SiC electronics intended for extreme environments, because temperature can significantly accelerate or slow down charge build-up kinetics.

2.3.4 JAXA Standards (Japan) and International Harmonization (ISO)

The Japan Aerospace Exploration Agency (JAXA) applies its own JERG (JAXA Engineering Standard) system, historically developed in parallel with U.S. MIL standards, but increasingly harmonized with ISO.

- JERG-2-211 (General Environmental Test Standard): Defines baseline requirements for environmental factors [37].
- JAXA approach: Unlike a deterministic "pass/fail" philosophy, Japanese standards emphasize building detailed component degradation models for integration into system-level simulators. For SiC devices, this is supported by dedicated heavy-ion beams at the Takasaki facility (TIARA/QST). This enables in-depth characterization of SEB including angular dependence, which may differ from silicon due to the crystal anisotropy of 4H-SiC [38,39].

Table 2.3.2 summarizes some of the key radiation-related standards discussed above and maps them to the main effect categories relevant for space qualification, namely TID, ELDRS, SEE, and DD. It also highlights important SiC-specific gaps, showing that although existing standards provide a useful qualification framework, they often do not explicitly address the material- and device-specific response of SiC electronics, especially for bipolar technologies and wide-bandgap failure mechanisms.

Table 2.3.2. Compliance matrix mapping testing standards to radiation effect types and key requirements (TID/ELDRS/SEE/DD) for the qualification of space-grade Electronic components.

Standard / system	TID (H/LDR)	ELDRS	SEE	DD	SiC-specific note
MIL-STD-883	✓ (A, D)	✓	—	—	LDR is critical for bipolar devices
MIL-STD-750	—	—	✓	—	SOA: Vds–LET (SEB/SEGR)
NASA GSFC EEE-INST-002	✓ (RLAT)	✓	✓	✓	lot-to-lot variability and COTS use
ECSS-Q-ST-60-15C	✓	✓	✓	✓	worst-case + derating
ESCC 22900	✓ (window 1h)	(per test plan)	—	—	annealing control, temperature
JAXA (JERG)	✓	✓	✓ (models)	✓	degradation model + heavy ions

"—" (not applicable / not covered); for "✓" (covered / applicable);

2.3.5 "New Space", COTS, and Automotive Standards (AEC-Q101)

The shift toward "New Space" concept for the past 10 years has increased the use of commercial off-the-shelf components (COTS), often qualified under automotive standards.

- AEC-Q101: De facto becoming a baseline selection standard for discrete SiC devices, ensuring process stability.
- Up-screening: Use of COTS requires additional qualification, including RLAT for each lot.
- Risks: The main issue for COTS SiC devices is lot-to-lot variability in radiation hardness. Process variations allowed under AEC-Q101 (e.g., in epitaxial thickness) can significantly change SEB sensitivity [5, 14].

2.3.6 Summary of Section Harmonizing Requirements for SiC

An analysis of regulatory frameworks (MIL-STD, ECSS, JAXA) shows that existing standards require adaptation for SiC-based electronics.

Key gaps identified:

- Displacement-damage dosimetry (NIEL): A transition to SiC-specific damage functions is required.
- TID temperature regimes: MIL-STD-883 does not fully account for SiC operation at extreme temperatures (cryogenic and high), where degradation mechanisms may deviate from standard models.
- SEE failure criteria: Binary "pass/fail" logic should be replaced by probabilistic SOA-based safety assessments.

Chapter 3. SiC Material, Devices, and Their Interaction with Radiation

3.1 Structural and Electrophysical Parameters of Silicon Carbide as a Wide-Bandgap Semiconductor

3.1.1 Crystal Structure and Polytypism

Silicon carbide (SiC) is a binary compound of Group IV elements, crystallizing in a strongly covalent structure (ionic fraction ~12% according to Pauling). The fundamental building block is the SiC_4 (or CSi_4) tetrahedron, where a carbon (or silicon) atom is surrounded by four silicon (or carbon) atoms at the vertices due to sp^3 hybridization.

A special feature of SiC is pronounced polytypism-the ability to crystallize in different modifications with identical chemical composition, density and basal-plane lattice parameters, but with different stacking sequences along the c- axis ([9] symmetry axis). More than 250 polytypes are known, however, only a few are relevant for devices: cubic 3C-SiC (zinc blende structure), hexagonal 4H-SiC and 6H-SiC (wurtzite-related structures) [9], [4].

The local bonding environment in SiC is tetrahedral, but the stacking sequence of Si-C bilayers determines whether the material adopts a cubic or hexagonal polytype. Figure 3.1.1 illustrates the difference between representative cubic and hexagonal lattice sites.

The stability and thus the feasibility of growing large crystals of specific SiC polytypes are influenced by temperature. This has practical implications, making certain polytypes like 3C-SiC, 4H-SiC, and 6H-SiC more prevalent and commercially available due to their balance of properties and manufacturability.

In modern power electronics and radiation-hard applications, the dominant polytype is 4H-SiC, due to its favorable band structure:

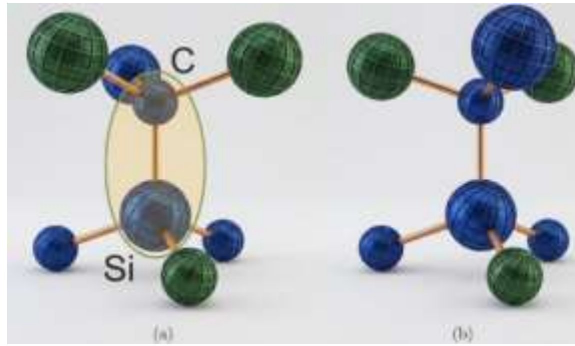

Figure 3.1.1 The cubic (a) and (b) hexagonal lattice site for Si(bright larger spheres) and C atoms(dark spheres) in SiC lattice.

- Largest bandgap: $E_g \approx 3.26$ eV (vs 2.3 eV for 3C-SiC and 3.0 eV for 6H-SiC).
- Higher mobility isotropy: Unlike 6H-SiC, where electron mobility along the c axis is much lower than in the basal plane ($\mu_{\parallel c}/\mu_{\perp c} \approx 0.2$), 4H-SiC shows weak anisotropy ($\mu_{\parallel c}/\mu_{\perp c} \approx 0.85$). This is critical for vertical power devices (MOSFETs, BJTs), where current flows perpendicular to the substrate.

3.1.2 Band Structure and Intrinsic Carrier Concentration

All SiC polytypes are indirect-bandgap semiconductors. For 4H-SiC, the conduction band minimum is located near the M point of the Brillouin zone, while the valence band maximum is at the Γ point.

The practical consequence of this stacking flexibility is the existence of several technologically relevant SiC polytypes. Figure 3.1.2 compares the stacking sequences of the common cubic and hexagonal forms.

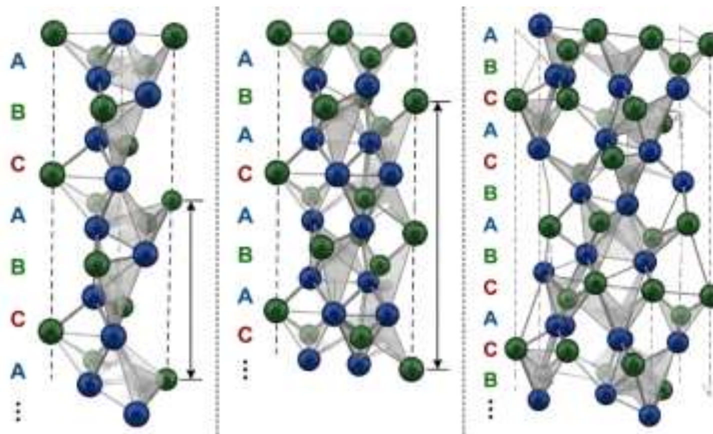

Figure 3.1.2. Atomic structure and stacking sequence Si and C biplanes of major SiC polytypes(left to right): cubic (3C) and hexagonal (4H, 6H).

A key advantage of SiC for high-temperature applications is the extremely low intrinsic carrier concentration n_i, determined by the bandgap E_g:

$$n_i = \sqrt{N_C N_V} \exp\left(-\frac{E_g}{2k_B T}\right)$$

At room temperature ($T = 300$ K), silicon has $n_i \approx 1.5 \times 10^{10}$ cm^{-3}, whereas 4H-SiC has $n_i \approx 5 \times 10^{-9}$ cm^{-3}.

Silicon p–n junctions lose rectifying behavior due to thermal generation already at $T > 150–200$°C when n_i becomes comparable to doping. In contrast, 4H-SiC devices can theoretically maintain low leakage and functionality up to $800–1000$°C (practically limited by packaging and contacts) [4].

3.1.3 Critical Breakdown Field and Baliga Scaling

The high Si–C bond energy ($E_{bond} \approx$ 4.6 eV) leads to a high critical electric field for avalanche breakdown (E_{crit}). For 4H-SiC, $E_{crit} \approx$ 2.5–3.0 MV/cm, which is about an order of magnitude higher than silicon (~0.3 MV/cm). This advantage is captured by the Baliga figure of merit (BFOM), which describes conduction losses in unipolar power devices:

$$BFOM = \epsilon \mu E_{crit}^3$$

For a given blocking voltage V_{BR}, the drift region thickness W_{drift} in SiC can be ~10 times smaller and the doping N_D can be ~100 times higher than in silicon. This reduces the specific on-resistance ($R_{on,sp}$) by roughly 300–400 times.

The practical importance of the high critical breakdown field becomes most evident when one considers the drift-region-limited resistance of unipolar high-voltage devices. Because a larger E_{crit} permits both a thinner drift layer and a substantially higher drift doping at the same blocking voltage, the resistance penalty associated with voltage scaling is dramatically reduced for larger bandgap materials. Figure 3.1.3 summarizes this argument by plotting the theoretical unipolar limit of specific drift-region resistance as a function of breakdown voltage. On a log–log scale, the separation between the Si and 4H-SiC curves is substantial over the entire voltage range, illustrating why 4H-SiC is fundamentally better suited for vertical high-voltage power devices. Table 3.1 below compares critical material and device parameters for silicon and different wide bandgap semiconductors.

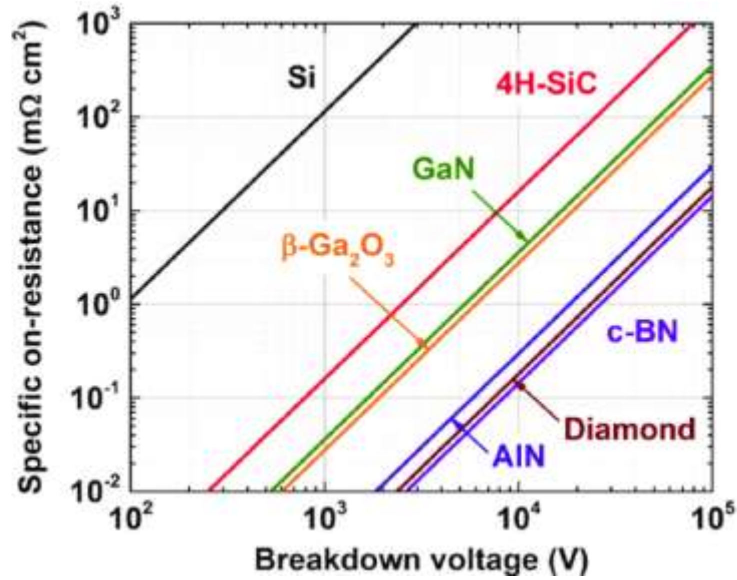

Figure 3.1.3. Theoretical unipolar limit of specific drift-region resistance as a function of breakdown voltage for Si and 4H-SiC. The log-log comparison illustrates the reduction in drift-region resistance enabled by the higher critical electric field of 4H-SiC.

As mentioned previously, the large bandgap of SiC and other wide bandgap semiconductors is also a substantial advantage when discussing radiation hardness, because the bandgap reflects the ionization energy, the energy needed to ionize atoms and induce charges in the material. In addition, it should be mentioned that the larger bandgap also indicate a stronger bonding between the atoms in the lattice, implying that larger energy is needed to displace lattice atoms. This is another benefit for the material tolerance to energetic particles.

3.1.4 Thermal Conductivity and Thermodynamic Stability

Thermal conductivity (λ) is critical for radiation robustness because it determines how efficiently heat, for instance deposited along a heavy-ion track, can be dissipated (thermal spike model). Single-crystal 4H-SiC reaches 3.7–4.9 W/(cm·K) at 300 K, exceeding copper and being ~3× higher than silicon. This not only reduce cooling needs for operating devices, but also helps minimize local overheating under pulsed ionizing radiation and increases thresholds for secondary breakdown and latch-up in parasitic bipolar structures [40].

Table 3.1. Comparative electro-physical parameters of Si, 4H-SiC, GaAs, GaN, and selected ultra-wide-bandgap materials at T = 300 K. Parameters should include bandgap, critical electric field, thermal conductivity, carrier mobility, density, electron-hole-pair creation energy, and displacement-threshold energy where available; units and sources must be stated for each quantity or in a table note.

Parameter	Si	4H-SiC	Diamond	GaN	GaAs	β-Ga_2O_3
Atomic number (Z)	14	14 / 6	6	31 / 7	31 / 33	31 / 8
Density (g/cm³)	2.33	3.22	3.51	6.15	5.32	5.88
Relative permittivity (ε_r)	11.9	9.7	5.7	9.6	12.9	10.2
Energy gap (eV)	1.12	3.23	5.5	3.39	1.42	4.6–4.9
e–h pair creation energy (eV)	3.6	7.6–8.4	13	8.9	≈4.2	≈13.5–14.3

3.1.5

Displacement energy (eV)	13–15	30–40	43	20	(13 ±1)	≈20–23 (Ga), ≈17–17.4 (O)
Breakdown electric field (V/cm)	$3 \cdot 10^5$	$(3-4) \cdot \cdot 10^6$	10^7	$4 \cdot 10^6$	$4 \cdot 10^5$	$(\geq 8 \cdot 10^6)$
Electron mobility (μ_n) (cm²/V·s)	1450	800	1800	1000	8500	150–180
Hole mobility (μ_p) (cm²/V·s)	450	115	1200	30	400	—
Saturated electron drift velocity (cm/s)	$0.8 \cdot 10^7$	$2 \cdot 10^7$	$2.2 \cdot 10^7$	$1.4 \cdot 10^7$	$\approx 1.0 \cdot 10^7$	$(1–2) \cdot 10^7$
Thermal conductivity (W/cm·K)	1.5	4.9	24–25	2.5	0.55	0.11–0.27

Challenges of the SiC/SiO_2 interface

A central technological limitation of SiC electronics, and one that becomes even more important under irradiation, is the quality of the SiC/SiO_2 interface. Unlike the oxidation of silicon, the thermal oxidation of SiC is not chemically clean: the growth of SiO_2 is accompanied by the release of carbon, and incomplete removal of carbon-containing species leads to the formation of suboxides and carbon-related defects in the near-interface region. As a result, the interface-state density remains comparatively high in relation to the Si/SiO_2 interface, especially close to the conduction-band edge of 4H-SiC.

To clarify the physical picture, Figure 3.1.4 schematically illustrates the spatial distribution of oxide and near-interface trapping regions discussed in irradiated oxide/semiconductor systems. Although this representation originates from the classical Si/SiO_2 literature, the same general classes of processes—fast interfacial exchange, slower border-trap exchange, and longer-lived hole trapping deeper in the oxide—are, at the present level of theoretical understanding, also expected in SiC/SiO_2 structures. The crucial difference is that, in SiC, the microscopic defect chemistry is strongly influenced by carbon-related oxidation by-products and by the inherently more complex interfacial transition region. For this reason, radiation-induced degradation in SiC must be treated primarily as an interface-controlled problem rather than as a purely bulk-material problem. [41].

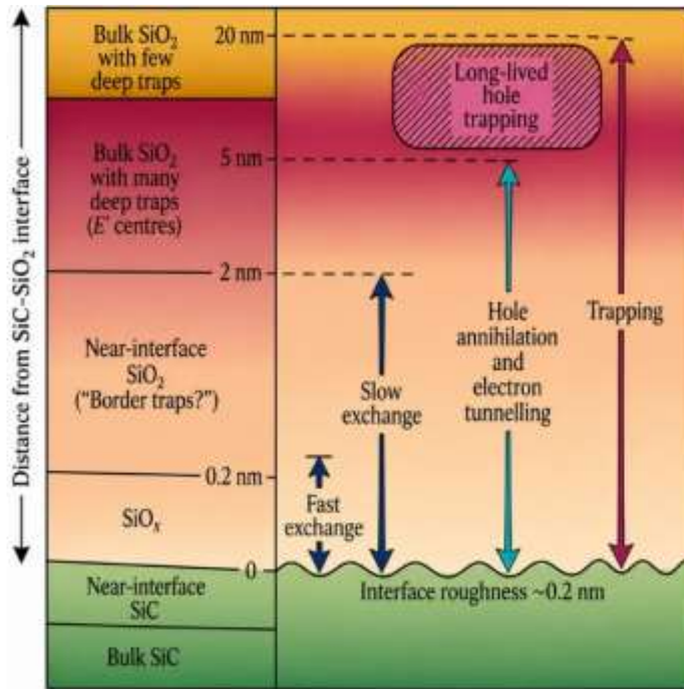

Figure 3.1.4. Schematic classification of near-interface and bulk-oxide trapping regions relevant to radiation-induced charge storage. [modified from 42]

The scheme was originally formulated for Si/SiO_2 systems; however, analogous fast interfacial exchange, border-trap dynamics, and deeper long-lived hole trapping are also expected in SiC/SiO_2, albeit with different microscopic defect chemistry.

3.1.6 Recombination Mechanisms: Auger, SRH, and Surface Recombination

Understanding recombination mechanisms is essential for analyzing radiation effects. For instance the base current I_B in a bipolar transistor can be represented as the sum of several components:

$$I_B = I_{SRH,bulk} + I_{surf} + I_{Auger}$$

Shockley–Read–Hall (SRH) recombination typically dominates in the bulk of the depletion region and the quasi-neutral base. The magnitude of this current is governed by the concentration of deep levels, intrinsic and radiation-induced defects. Surface recombination (I_{surf}) occurs at the periphery of the emitter junction and in SiC BJTs this contribution often dominates at low base current densities. Radiation-induced charge in the passivation oxide modulates this term, causing degradation of the transistor current amplification β at low collector currents, i.e. the low-injection region of the Gummel plot [41]. The final term, the Auger recombination, becomes significant only at high injection levels, limiting the maximum current density.

3.2 Operating Principles and Process-Design Features of SiC BJTs

3.2.1 Vertical Architecture and Mesa Technology

Unlike silicon integrated electronics, where planar lateral structures dominate, modern 4H-SiC bipolar transistors are implemented mainly in a vertical topology, as shown in Figure 3.2.1. This is driven by the need to achieve relevant high breakdown voltages while maintaining moderate current density.

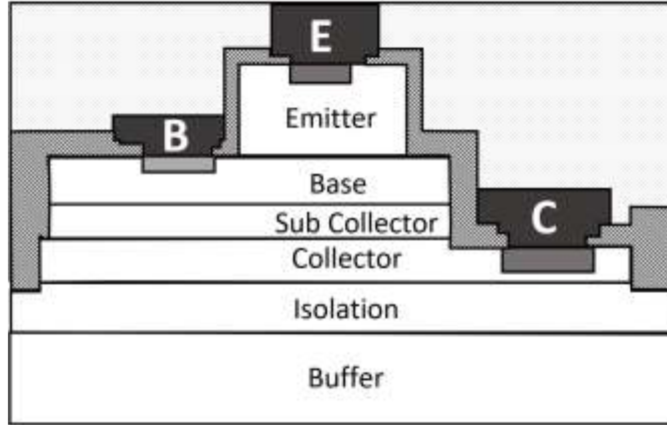

Fig. 3.2.1. Cross section of a typical high-voltage 4H-SiC BJT with mesa isolation of the emitter and a multi-step junction JTE system.

A typical n-p-n SiC BJT is formed by chemical vapor deposition (CVD) epitaxy and consists of the following layer sequence: 1. Emitter: A heavily doped n-type layer ($N_D \sim 10^{19}$ cm^{-3}) to ensure high injection efficiency. 2. Base: A thin p-type layer (0.1–0.5 µm) with relatively high doping ($N_A \sim 10^{17}$–10^{18} cm^{-3}). SiC-specific feature: Due to very low dopant diffusion in SiC, the base is formed not by thermal diffusion (as in Si) but by epitaxial growth. This allows precise control of the doping profile, but complicates the formation of low-resistance ohmic contacts. 3. Collector (drift region): A lightly doped n-type layer ($N_D \sim 10^{15}$–10^{16} cm^{-3}). Its thickness and doping concentration defines the device blocking capability (V_{CBO}).

Emitter–base and base–collector isolation is typically achieved by deep plasma etching (ICP-RIE), forming mesa structures. The emitter mesa sidewalls are critical regions, because the p–n junction reaches the surface, creating potential paths for leakage currents and enhanced surface recombination.

3.2.2 Current Gain (β) and Its Limiting Factors

A key BJT parameter is the common-emitter DC current gain ($\beta_{DC} = I_C/I_B$). In SiC BJTs it is determined by the competition between emitter injection efficiency (γ) and the base transport factor (α_T):

$$\frac{1}{\beta} \approx \frac{1}{\gamma} + (1 - \alpha_T) \approx \frac{D_p W_B N_A}{D_n L_p N_D} + \frac{W_B^2}{2L_n^2}$$

where W_B is the base width and L_n is the electron diffusion length in the base. where β is the common-emitter current gain, γ is the emitter injection efficiency, α_T is the base transport factor, W_B is the neutral base width, D_p is the hole diffusion coefficient in the n-type emitter,

D_n is the electron diffusion coefficient in the p-type base, L_p s the hole diffusion length in the emitter, L_n is the electron diffusion length in the base, N_A is the acceptor concentration in the base, and N_D is the donor concentration in the emitter (for an n-p-n transistor).

In terms of SiC: The short minority-carrier lifetime in the base ($\tau_n \sim 0.1\text{–}1$ μs), limited for instance by deep centers (e.g. $Z_{1/2}$, the carbon vacancy), reduces the transport factor that affects bulk recombination. As a result, β becomes highly sensitive to DD defects that introduce additional recombination centers [43]. Due to the mesa geometry, the emitter–base junction intersects the surface. High surface recombination velocity (S_{surf}) at the SiC/SiO_2 interface along the mesa sidewall generates a significant parasitic base current. This is the main degradation mechanism under ionizing radiation, since charge build-up in the oxide modifies the surface area and potential [41, 44, 45].

3.2.3 Impact of Incomplete Dopant Ionization

Unlike silicon, where common dopants (B, P, As) are fully ionized at room temperature, in 4H-SiC the ionization energies of acceptors (Al: –200 meV) and donors (N: –90 meV) are relatively high. This has the effect that the ionization degree of acceptors (Al) in the base may be just a few percent. This increases base resistance (R_B) and leads to emitter current crowding toward mesa edges, increasing local current density and sensitivity to surface-related effects. However, with increasing temperature, dopant ionization increases exponentially, which may cause an increase in current gain β (unlike the typical decrease in Si) until it is compensated by reduced mobility and reduced lifetime at very high temperatures (> 300°C) [4].

3.3 Review of Radiation Effects in Wide-Bandgap Devices

Before delving into the specific radiation tolerance of various semiconductor materials, it is important to place wide-bandgap semiconductors within the broader class of materials used in electronic devices, including not only the active semiconductor itself, but also on-chip dielectrics and contacts, as well as mounting, interconnection, and packaging materials. This comparison is shown qualitatively in Figure 3.3.1.

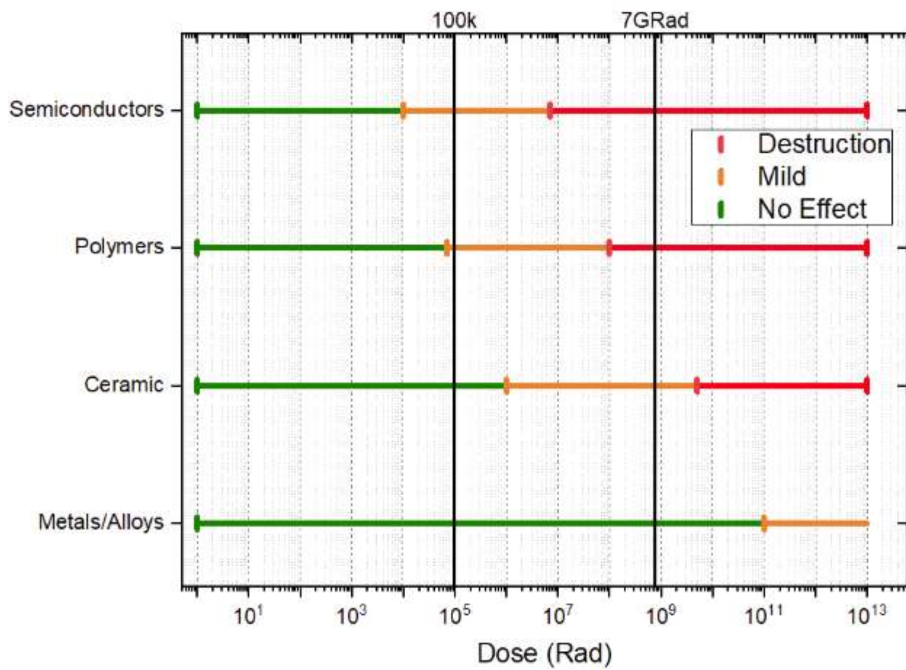

Figure 3.3.1. Radiation tolerance ranges for broad material classes used in electronics, indicating thresholds for no effect, mild degradation, and destruction.

Figure 3.3.1 illustrates the comparative radiation tolerance of four major material classes semiconductors, polymers, ceramics, and metals/alloys measured by total absorbed dose. The operational states are categorized into "No Effect" (green), "Mild" degradation (orange), and "Destruction" or catastrophic failure (red).

As the chart demonstrates, metals and alloys exhibit extreme radiation hardness, showing virtually no functional effect up to doses of 10^{11} rad. Ceramics also demonstrate high robustness, maintaining their properties up to approximately 10^6 rad before mild degradation begins, with structural failure occurring only near the 7 Grad threshold. Polymers, widely used for passivation and packaging, are more sensitive, starting to degrade mildly at 100 krad and reaching destruction around 10^8 rad.

Critically, semiconductors represent the most vulnerable class of materials. Mild degradation (such as threshold voltage shifts and increased leakage currents) can begin at doses as low as 10^4 rad, and catastrophic failure typically occurs just above 10^7 rad. This fundamental sensitivity dictates that the radiation limit of any complex electronic system is almost entirely determined by its active semiconductor components. Consequently, understanding the intrinsic and extrinsic mechanisms of semiconductor degradation specifically in wide-bandgap materials is the primary focus of this chapter.

3.3.1 Intrinsic and Extrinsic Radiation Hardness: Comparative Materials Physics

The radiation hardness of a semiconductor device under gamma (γ) irradiation is not a single parameter; rather, it represents a superposition of two independent factors that govern the device's response to high-energy photon interactions [46-47]:

- Intrinsic hardness: Defined by the properties of the crystal lattice (bond energy, displacement threshold, material density) and the electronic band structure.

- Extrinsic hardness: Limited by technology- and process-dependent layers—gate dielectrics, passivation, contacts, and interface quality.

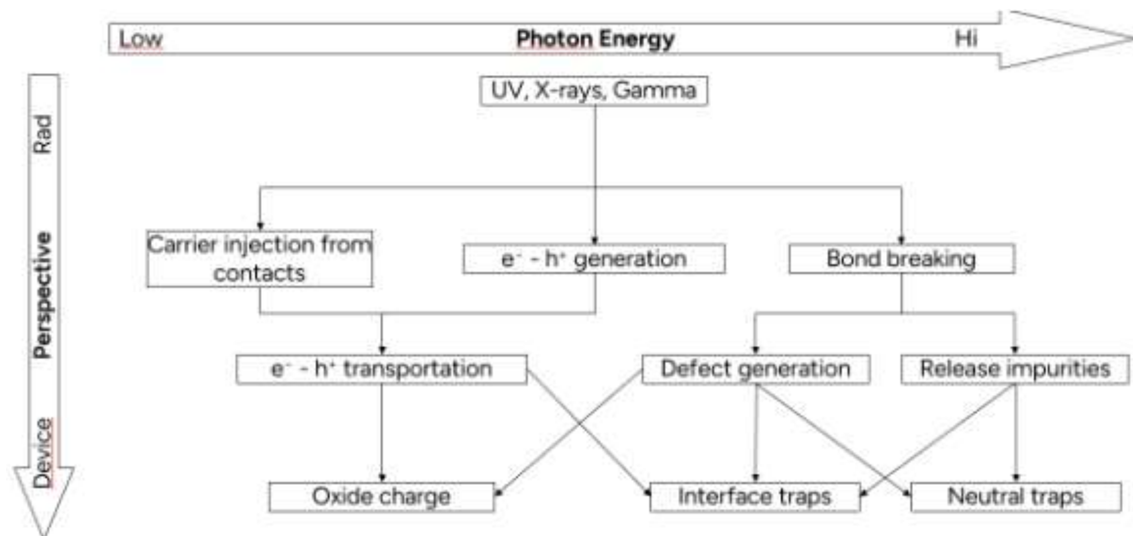

Figure 3.3.2. Hierarchical conceptual flowchart linking photon-induced ionization, defect generation, oxide/interface trap formation, and macroscopic device-level degradation, modified from [46-47].

To systematically understand how these intrinsic and extrinsic factors interact, Figure 3.3.2 illustrates the hierarchical flow of physical mechanisms, mapping the progression from the fundamental radiation perspective down to the macroscopic device perspective [47, 48].

Depending on the incident photon energy (ranging from UV to high-energy X-rays and γ-rays), the initial interaction triggers three primary microscopic processes: carrier injection from contacts, electron-hole (e^-/h^+) pair generation within the semiconductor bulk and dielectric layers, and direct bond breaking.

These primary events subsequently evolve into intermediate transport and structural modifications. The generated e^-/h^+ pairs undergo transportation, where difference in electron and hole mobilities dictate the charge dynamics, while bond breaking leads to localized defect generation and the release of impurities [47-49].

Ultimately, these processes converge at the device level, manifesting as extrinsic degradation mechanisms:

- Oxide charge: Primarily formed by the transport and subsequent trapping of holes within the dielectric layers, a process often aggravated by radiation-induced defects.
- Interface traps: Created by a complex combination of charge transport dynamics, direct defect generation at the material boundaries, and the migration of released impurities toward the interface.
- Neutral traps: Resulting directly from bulk defect generation and the release of impurities within the lattice.

This pathway clearly demonstrates how intrinsic fundamental interactions (pair generation and bond breaking) directly drive the degradation of extrinsic device elements (oxide and interface quality) [47,48].

A comparison of 4H-SiC with Si and competing III–V compounds like GaAs and GaN helps identify the fundamental physical limits of each technology in radiation environments.

3.3.1.1 Electron–Hole Pair Creation Energy (ε) and Initial Charge Yield

A key parameter governing sensitivity to ionizing exposure is the average energy required to generate one e^{-}/h^{+} pair by an ionizing particle, E_p. This parameter is vital for TID and transient processes in SEE and is given below for some relevant semiconductors [1, 2].

- Si ($E_g = 1.12$ eV): $E_p \approx 3.6$ eV.
- GaAs ($E_g = 1.42$ eV): $E_p \approx 4.8$ eV.
- 4H-SiC ($E_g = 3.26$ eV): $E_p \approx 7.8$ eV.
- GaN ($E_g = 3.4$ eV): $E_p \approx 8.9$ eV

Physical implication: When an ionizing particle (e.g., a proton or a heavy ion) traverses the active region, 4H-SiC generates ~2.2 times fewer excess charge carriers than silicon and ~1.6× fewer than GaAs, assuming the same absorbed energy.

Because the average energy required to create an electron–hole pair in 4H-SiC is substantially larger than in Si or GaAs, the same deposited ionizing energy produces a smaller initial excess-carrier density. In practical terms, this suppresses the amplitude of radiation-induced photocurrents and increases the charge required to activate parasitic regenerative structures. The consequence is not immunity to TID or SEE, but a lower initial charge yield at the moment of energy deposition. This reduced prompt carrier generation is one of the intrinsic physical advantages of wide-bandgap semiconductors in radiation environments. It gives lower TID and a lower probability of latch-up in parasitic BJT or thyristor structures, since the critical charge required to trigger a parasitic path is harder to reach [50].

3.3.1.2 Displacement Threshold Energy (E_d)

Resistance to DD is determined by the threshold kinetic energy that must be transferred to a lattice atom to displace it from its site into an interstitial position (Frenkel-pair formation) [51,52].

- Si: $E_d \approx 13–20.5$ eV (approximately isotropic).
- GaAs: Ed(GaAs)≈13±1 eV.
- 4H-SiC: E_d(C) $\approx 20–22$ eV, E_d(Si) ≈ 35 eV.
- GaN: E_d(N) $\approx 19–22$ eV, E_d(Ga) ≈ 45 eV

The high covalent bond energy in SiC makes it extremely resistant to nuclear interactions. However, as noted by Messenger [53], the presence of two sublattices with different atomic masses (Si and C) creates a complex defect-formation landscape. The “light” carbon sublattice is damaged significantly more efficiently at low energies of incident particles (electrons; and gamma quanta indirectly via Compton electrons). Carbon vacancies (V_C),

evolving into thermally stable $Z_{1/2}$ complexes, become the dominant recombination centers (lifetime killers) in 4H-SiC.

Unlike SiC, in GaN the large mass difference ($M_{\mathrm{Ga}} \approx 5.8 M_{\mathrm{N}}$) causes irradiation energy to be transferred predominantly to nitrogen atoms during ion irradiation, making the N sublattice the "weak link".

3.3.1.3 Volumetric Charge Yield and Rad-Hard Potential: A 3D Perspective

To quantitatively assess the intrinsic radiation hardness of various semiconductor materials and insulators, it is essential to evaluate their potential from the perspective of initial gamma radiation-induced charge generation. This is done in Figure 3.3.3.

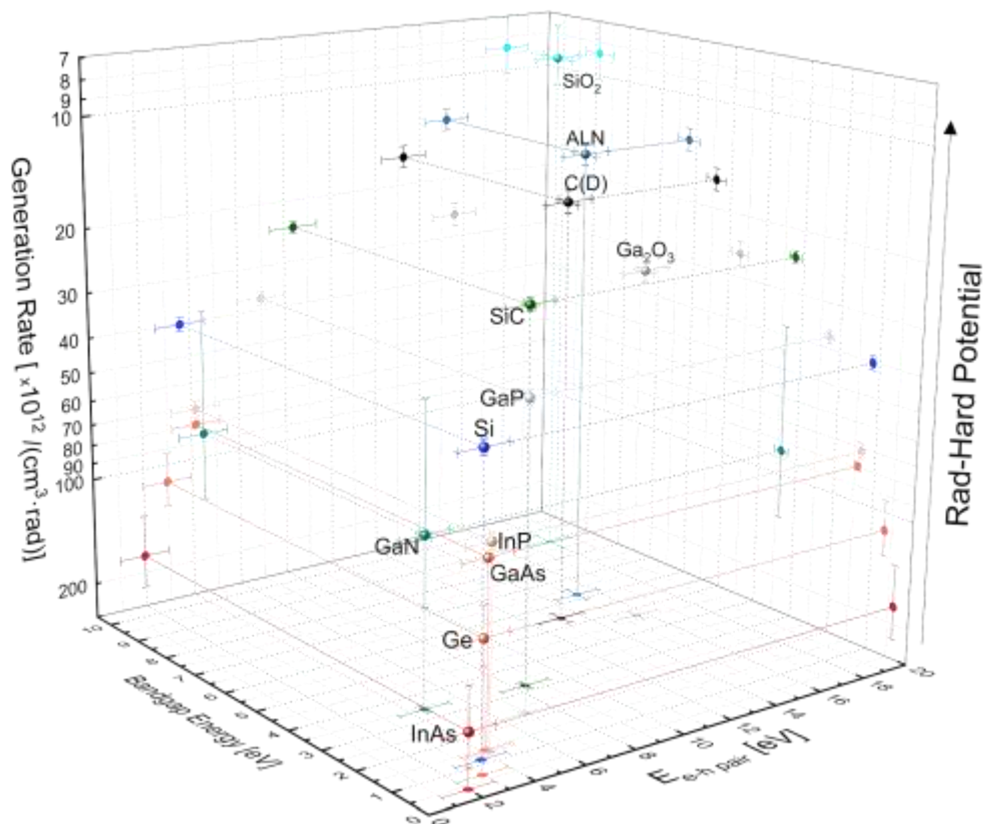

Figure 3.3.3. Comprehensive 3D mapping of fundamental semiconductor properties governing intrinsic radiation hardness.

The plot correlates bandgap energy (E_g), average electron-hole pair creation energy $E_{e\text{-}h\ pair}$), and volumetric charge generation rate, with material density (g/cm^3) color-coded. The vertical "Rad-hard potential" vector demonstrates the superiority of WBG and UWBG materials in minimizing radiation-induced plasma yield.

The 3D scatter plot in Figure 3.4.2 serves as a unified multidimensional map, illustrating this comparative potential by synthesizing the fundamental components that govern ionization. The generation of free charge under ionizing radiation is strictly dependent on two primary band-structure parameters: the bandgap energy (E_g) and the energy required to generate a single electron-hole pair (E_{e-h}). By calculating the volumetric charge yield

based on these parameters, the vertical Z-axis represents the generation rate (expressed in 10^{12} pairs/(cm^3 · rad)).

The visualization clearly segregates electronic materials into distinct performance clusters along the "Rad-hard potential" vector:

- The vulnerable cluster (bottom): classical narrow-bandgap semiconductors such as InAs, Ge, GaAs, and Si are grouped at the bottom of the Rad-hard potential axis. They are characterized by low E_{e-h} values and exceptionally high carrier generation rates ($> 40 \times 10^{12}$ pairs/(cm^3 · rad)). This massive initial plasma yield fundamentally limits their stability in high-radiation environments, making them highly susceptible to transient dose-rate effects and single-event latch-ups.
- The WBG transition zone (middle): Materials like 4H-SiC and GaN sit significantly higher on the axis. Possessing larger bandgaps and higher E_{e-h} thresholds, their volumetric generation rate is dramatically suppressed.
- The UWBG and insulator apex (top): Ultra-wide-bandgap materials (such as AlN and Diamond) and insulators (SiO_2) occupy the pinnacle of the chart. Their charge generation is suppressed to single-digit values on this scale.

Thus, 4H-SiC structurally minimizes the initial plasma yield during γ-irradiation, visually confirming that its superior radiation tolerance is deeply rooted in its fundamental electronic band structure rather than just processing techniques. Furthermore, the color-coded density parameter highlights a crucial physical nuance: while denser materials exhibit different interaction cross-sections for incident particles, the overarching driver for ionization suppression and upward movement along the "Rad-hard potential" axis remains the E_g/E_{e-h} synergy.

3.3.2 Total Ionizing Effects (TID): The Interface Problem in WBG Electronics

Despite high bulk hardness, the main vulnerability of SiC devices (especially MOSFETs and BJTs) is the dielectric layers and interfaces. This is where a fundamental difference between SiC and GaN technologies becomes apparent.

3.3.2.1 Specific Features of SiC Oxidation

SiC is essentially the only WBG material with a stable native oxide (SiO_2), enabling a planar technology similar to silicon. However, during thermal oxidation, carbon clusters and suboxides (SiO_xC_y) form at the SiC/SiO_2 interface. These defects create a high interface-state density (D_{it}) and act mainly as deep hole traps.

GaN typically does not have a native oxide and is widely implemented as HEMT structures with a Schottky barrier or a p–n junction gate. This makes GaN HEMTs largely insensitive to TID in the gate region, because there is no thick oxide available for charge buildup. However, surface passivation (commonly Si_3N_4 or Al_2O_3) remains a vulnerable element [32].

3.3.2.2 Physics of Charge Trapping in SiC/SiO2

Under ionizing irradiation, e^{-}/h^{+} pairs are generated in the oxide. Electrons, due to high mobility ($\mu_n \approx 20$ cm²/V·s), leave the oxide rapidly (on picosecond time scales). Holes, in contrast, are transported extremely slowly ($\mu_p \sim 10^{-5}$ cm²/V·s) via polaron hopping transport [43].

In radiation-hardened Si technologies, thin or nitrided oxides are used to minimize hole trapping. In SiC, by contrast, the high concentration of near-interface defects can drive the hole-capture fraction (f_h) close to 100%. This causes for instancea strong negative threshold-voltage shift (ΔV_{th}) in MOSFETs and s-type inversion in the p-base of BJTs, creating leakage channels.

3.3.2.3 Temperature and Bias Dependence

Classical silicon TID models (where the worst case is irradiation under positive bias) require modification for SiC.

- Cryogenic anomalies: At low temperatures (-50°C to -100°C), hole transport in the oxide nearly stops ("frozen holes"). This results in the buildup of a very large positive charge (N_{ot}) in the oxide bulk, without reaching the interface. As shown in [54], for SiC bipolar transistors this can lead to enhanced base-leakage degradation and reduced current gain β specifically at low temperatures—behavior not typical for silicon.
- Zero-bias condition: The absence of a sweeping electric field (zero-bias regime) in SiC BJTs promotes recombination and trapping near critical emitter-mesa regions, making this regime a "hidden" worst case for passive on-orbit storage.

The charge-trapping pathway that connects gamma irradiation to surface recombination in SiC BJTs is summarized schematically in Figure 3.3.4. The diagram emphasizes the asymmetry between rapid electron transport and slow hole transport in SiO₂, and the resulting accumulation of positive oxide charge near the semiconductor interface.

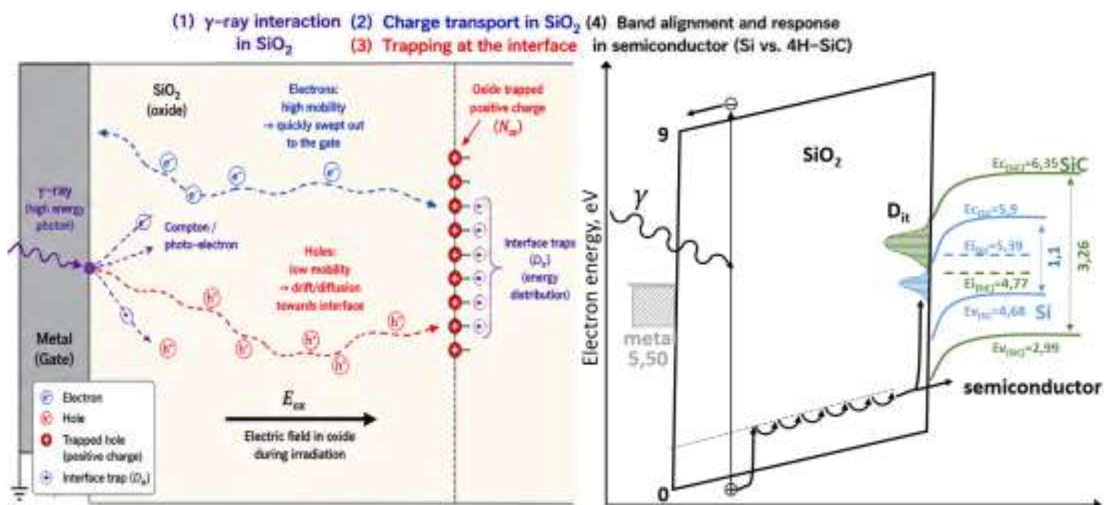

Figure 3.3.4. Adapted from Oldham & McLean . Mechanism of radiation-induced charge buildup in the SiO₂/semiconductor (SiO2-black, Si blue and SiC-green, not in scale) system.

The diagram above illustrates pair generation, rapid electron escape, slow hole drift, and hole trapping at deep levels like E'_{γ} centers and carbon clusters near the interface. It also indicates differences in bandgap and barrier heights for Si versus SiC. A high density of carbon-related interface traps leads to efficient hole trapping and degradation of device parameters.

3.3.3 Displacement Damage

While TID tolerance is determined by dielectric quality, resistance to displacement damage is a fundamental property of the crystal lattice. Quantitatively, damage is described using the NIEL metric, which enables scaling across particles of different nature (protons, neutrons, electrons).

3.3.3.1 Defect Spectroscopy in 4H-SiC

Due to its high bond energy, SiC exhibits a low introduction rate of primary defects (vacancies and interstitials). However, the defects that do form have distinctive electrical properties.

Dominant defect ($Z_{1/2}$): In n-type 4H-SiC, the main radiation-induced defect is the $Z_{1/2}$ center located at $E_C - (0.63 - 0.67)$ eV. It is commonly identified as a carbon vacancy (V_C) *[55]*.

Impact on recombination: A defining feature of the $Z_{1/2}$ center is its extremely large capture cross section for minority carriers ($\sigma \sim 10^{-14}$ cm²). This implies that even a small defect concentration can cause a sharp reduction in minority-carrier lifetime (τ). This is critical for bipolar devices (BJTs, PiN diodes), since β degradation can occur even at fluences that do not produce noticeable dopant compensation (i.e., without strong R_{on} changes) [5, 6].

3.3.3.2 BJT Degradation: Messenger–Spratt Model

Experimental irradiation data for SiC BJTs with neutrons and ions indicate that gain degradation follows the relationship [31]:

$$\frac{1}{\beta(\Phi)} = \frac{1}{\beta_0} + K_\beta \cdot \Phi_{eq}$$

where $\beta(\Phi)$denotes the irradiated common-emitter current gain, β_0 is the initial gain before irradiation, K_β is the damage coefficient characterizing gain sensitivity to DD, and Φ_{eq} is the equivalent DD fluence. The linear dependence of $1/\beta$ on Φ_{eq} is the classical Messenger-Spratt form for BJT gain degradation under DD. [7, 8].

3.3.4 Temperature Dependence and the "Self-Recovery Window"

A unique feature of SiC is the possibility of operation at temperatures high enough to activate in-situ annealing of radiation defects during device operation.

Annealing stages [56-57]:

- $150 \dots 300°C$: Annealing of the simpler defects (interstitials, close Frenkel pairs). Partial mobility recovery is observed.
- $400 \dots 600°C$: A critical range for bipolar devices. Dissociation/transformation of complexes such as $EH_{1/3}$ can occur. Experiments [8, 9] show that annealing at $420°C$ (achievable in specialized packaging) can almost fully restore BJT gain after moderate-fluence proton irradiation.
- $> 600°C$: Annealing of deep centers such as $Z_{1/2}$

These features of thermal defect stability could have design implication. Unlike silicon, where heating aggravates leakage and thermal generation, in SiC elevated operating temperature can be exploited as a method to extend radiation lifetime: Radiation hardening by system design.

3.3.5 Conclusion

The literature analysis suggests that SiC BJTs occupy a distinctive niche for radiation-hard applications. They avoid the main MOS weakness—gate oxide vulnerability, e.g single event gate rapture SEGR and TID sensitivity. Their main vulnerability is perhaps gain loss due to displacement-induced defects, but this can be mitigated at the circuit level by base-current margins, or technologically/system-wise by operation at elevated temperatures, enabling self-annealing.

Chapter 4. Experimental Methodology, Test Setup, and Parameter Extraction

4.1 Overview of Experimental Design

In space qualification, the total ionizing dose is not always the main ambiguity; the ambiguity is almost always how the dose was delivered and how the device was studied while it was exposed. Radiation-hardness claims can be made "true" or "false" simply by changing (i) dose rate, (ii) bias state, and (iii) the time window between irradiation and measurement—because oxide/interface charging and recombination-related damage in bipolar technologies are strongly governed by slow kinetics for trap capture/emission, hydrogen-related reactions, and time-dependent relaxation. This is the deeper reason why modern RHA is not "testing at the end," but a requirements-driven experimental contract: the mission environment and operational modes must be translated into a test plan whose stress axes, such as dose, dose rate, bias, temperature and timing, are explicit and reproducible [34, 59-61].

Two consequences follow immediately:

- A single "unbiased ^{60}Co exposure" cannot bound all operational risks, even if the measured degradation looks small—because bias fields can change where charge builds up and which leakage or recombination paths become active.
- A single high dose-rate test cannot always bound low dose-rate performance, especially in bipolar technologies where ELDRS is a known risk class and is widely discussed in the broader bipolar radiation-effects literature (largely in silicon, but as a *design warning* rather than a material-specific claim) [62, 63].

These principles are not philosophical; they are embedded in European and US test standards that treat dose rate, bias, and post-irradiation timing as controlled variables rather than "details." For example, ESCC 22900 standards explicitly structures TID testing around defined

dose-rate ranges and required measurement timing windows, including a "time window" requirement after irradiation and options for interim measurements, reflecting the practical reality of recovery, or annealing, and time-dependent relaxation [34, 59, 60].

4.2 Standards as "design rules" for the experiment (ESA / NASA / MIL logic, expressed as controlled variables)

A standards-aligned TID program must treat the following as first-class experimental variables.

ESCC 22900 defines structured dose-rate categories (commonly expressed as A/B/C-type ranges) and couples them to required measurement timing logic, reflecting the fact that TID outcomes can change when irradiation is "fast" versus "slow." NASA guidance similarly emphasizes that test conditions (including dose rate and timing) must be selected and reported so the results remain interpretable for mission use, especially when bipolar-like dose-rate sensitivity is a concern [34, 59-61].

Bias fields reshape the internal electric-field distribution, which in turn changes where oxide/interface charge is trapped and how leakage and recombination paths are activated. This is why ESCC-style testing treats bias as part of the test definition, not as an optional annotation [59,60].

A critical practical reason why standards impose timing windows is that post-irradiation recovery (or relaxation) can mask the peak damage state. The early KTH circuit work explicitly reports measurements performed within a bounded timing framework and later measurements after hours or days, illustrating that timing is part of the reported experimental contract. ESCC 22900 similarly encodes timing windows and interim measurement logic as part of the method itself [*59,60, Paper II*].

Space qualification is not only about average values; it is more about analysis: part-to-part variability, condition-dependent dispersion, and worst-case behavior. This becomes especially important when dose rate decreases—because lower dose rate can increase sensitivity *and* widen variability in some technologies. NASA RHA guidance explicitly treats these issues as central in qualification logic [61-63].

The experimental program in this thesis expands along five controlled directions: i) device-level BJT response, ii) circuit-level inverter/TTL behavior, iii) interface/process variation, iv) compact modeling, and v) temperature. Together, these axes transform "SiC survives radiation" from a scalar statement into a design-relevant sensitivity map.

Table 4.1 summarizes how the five appended papers are positioned within the overall experimental strategy of the thesis. For each paper, Table 4.1 identifies the primary study object, the controlled stress axes, the main extracted observables, and the corresponding outcome type. This overview clarifies how the work progresses from discrete transistor

characterization to circuit-level analysis, compact modeling, and temperature-dependent qualification.

Table 4.1. Overview of the appended papers and their roles within the experimental radiation-hardness methodology of the thesis.

Paper	Primary study object	Controlled stress axes	Outputs	Outcome type
Paper I	Discrete/characterized BJT	Dose, dose rate, bias regime	β degradation, V_{BE} shift, regime ranking	Worst-case map at device level
Paper II	BJT inverter	Dose, dose rate, logic state (activ/ON/pass)	Transfer curve stability, supply/standby current	System-level vulnerability mode
Paper III	TTL IC batches	Dose, bias state, oxide type	I_{CC} deviation, batch comparison, ELDRS evidence	Interface-limited hardness
Paper IV	BJT + inverter SPICE	Dose → parameter drift	VBIC parameter trends, circuit-level prediction	Design-grade predictive layer
Paper V	BJT at low T	Dose, dose rate, temperature	β(T,D) trends, amplified sensitivity at cold	Kinetics-aware mission relevance

4.3 Gamma Radiation Testing Setup and Protocols

The standards perspective reframes earlier KTH high-dose demonstrations and they remain essential because they show that the technology survives, but they do not by themselves bound mission-relevant worst cases. This thesis therefore treats the earlier work as the feasibility baseline and extends it to standards-aligned characterization with explicit control of dose rate, bias, temperature, and measurement timing [Paper I-III].

Across Papers I–III and V, the protocol systematically varies total dose, dose rate, bias state, temperature, and post-irradiation timing. This common framework makes the data comparable across irradiation campaigns and ties the experiments directly to the needs of radiation hardness assurance.

4.3.1 Timing Rules and Annealing Windows

Here a 10-to-1 exposure-to-measurement timing used, according to the recommendations in theMIL-STD-883 standard (Method 1019). A key timing rule is that post-irradiation electrical measurements must begin within a time interval bounded relative to the incremental irradiation time, commonly described as a 10% constraint [Paper I, Paper V].

ESCC 22900 formalizes a “multi-time” readout philosophy, where an early readout shortly after exposure is used to capture immediate damage before substantial annealing, and delayed readouts to capture relaxation and longer-term drift. It also specifies an elevated-temperature bake step for recovery assessment [Paper II, Paper III].

4.3.2 Dosimetry and irradiation-field uniformity: what was controlled and how cross-facility comparability was protected

Because the thesis uses multiple irradiation facilities, dosimetry becomes a first-order requirement. The campaigns therefore preserve explicit dose definitions, fixed geometry within

the uniform radiation field, and reported uncertainty/uniformity bounds so that comparisons across facilities remain physically defensible [Paper I, Paper III, Paper V].

4.3.5 Bias-state realism: aligning experimental regimes with NASA/MIL expectations for "does it still operate?"

At system level, the key distinction is between functional survivability and parametric integrity. The strength of the stated experimental program is that it does not test radiation in a single convenient state, but across realistic passive, standby, and active regimes so that worst-case vectors can be stated explicitly [Paper I–III, Paper V].

4.4 Data Collection and Analysis Techniques

The experimental methodology used in this thesis was designed to ensure that radiation-induced changes were recorded under controlled electrical and thermal conditions, with minimal uncertainty introduced by post-irradiation delay, long interconnects, or environmental interference. For this reason, the main principle of the data-acquisition workflow was in-situ characterization, in which the devices remained electrically connected and were measured immediately after each irradiation dose increment, rather than being removed from the radiation field and tested later. This approach was particularly important for 4H-SiC bipolar structures, where oxide- and interface-related degradation may evolve on timescales comparable to the exposure sequence itself. In practice, the method allowed the electrical state of the device during irradiation to be preserved as an explicit experimental variable, while also reducing ambiguity caused by uncontrolled short-term recovery [Paper I–III, Paper V].

The discrete BJT measurements were carried out using packaged dies mounted in Kyocera 40-pin dual in-line packages (DIP) and wire-bonded with gold wires. Irradiation was performed at the ^{60}Co Calliope facility at ENEA Casaccia, using a source rack composed of cobalt plates distributed over an active area of approximately 41 × 75 cm inside a shielded irradiation cell with activity 1.4×10^{15} Bq (38 kCi) (May 2023). The dose quantification was based on ESR-alanine dosimetry. To improve spectral relevance and suppress unwanted low-energy secondary photons, an Al/Pb filter was placed in front of the devices. This was especially important for the BJT campaign, where the objective was not only to accumulate TID, but also to compare degradation across multiple biasing conditions and dose rates without introducing avoidable spectral distortion [Paper I, Paper V].

The remote electrical readout was assembled on a National Instruments PXIe platform, using an NI PXIe-1078 chassis, PXIe-4081 digital multimeter, two PXIe-4136 source-measure units, a PXI-4110 programmable DC supply, and an NI PXIe-2532 switching matrix. Because the instrumentation had to be positioned outside the high-dose zone, the devices were connected through approximately 20 m cables. These long lines introduced non-negligible parasitic

capacitance and susceptibility to electromagnetic pickup. Therefore, the cable shields were driven from the guard terminals of the SMUs, and the switching matrix was configured in sense mode to improve accuracy over long interconnects. In addition, line calibration was performed at every iteration. The practical readout time after each step was approximately 2 min, which represented a compromise between measurement completeness and strict control of timing-induced annealing effects [Paper I, Paper V].

The physical device geometry used in the BJT irradiation campaigns is shown in Figure 4.1. This structure is relevant because the emitter-mesa sidewall, passivation oxide, base contact geometry, and termination region define where surface recombination and oxide/interface charge accumulation can influence the measured base current.

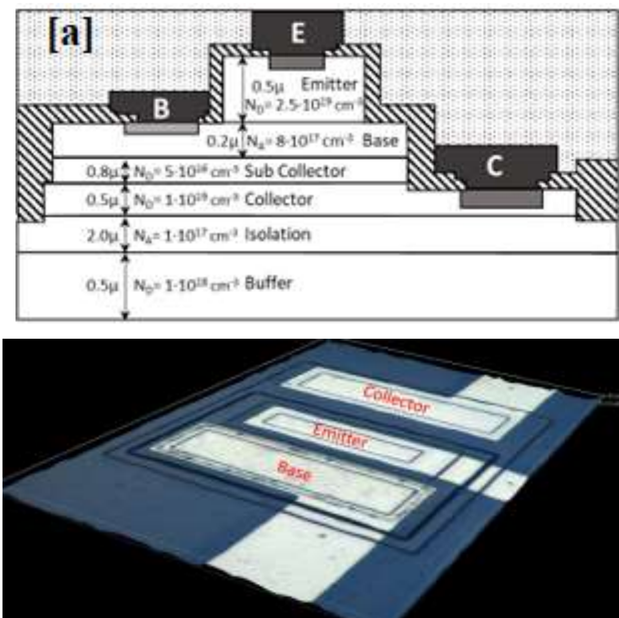

Figure 4.1. Cross-section and top view of the discrete 4H-SiC BJT used in the irradiation experiments. Layers (a) and 3D view (b). Not to scale.

For the discrete transistors, the primary acquisition mode was DC characterization through Gummel-type measurements. During each readout sequence, the collector-emitter voltage was fixed at $V_{CE} = 15$ V, while the base-emitter voltage was swept from 0 to 15.6 V in 0.2 V steps. Current compliance was set to 1 A at each terminal. Since the bunker environment and long cables inevitably introduced occasional outliers and pickup noise, every voltage-current point was sampled seven times, after which a trimmed mean with $\alpha = 15\%$ was computed. This simple but robust statistical filter improved the effective current resolution to approximately 5 ± 1 nA, which was sufficient for monitoring subtle changes in base current and low-injection collector current. The raw dataset therefore consisted of repeated $I_C(V_{BE})$and $I_B(V_{BE})$ curves acquired after successive dose increments, from which the common-emitter current gain $\beta = I_C/I_B$ was extracted as the principal degradation observable. The same infrastructure was

reused for measurements under saturation, cut-off, active, reverse, and zero-bias irradiation conditions, allowing the operating state itself to be treated as part of the experimental matrix rather than as an uncontrolled background condition. [Paper I, Paper V]

A second acquisition branch of the work extended the same measurement logic to low-temperature irradiation. For this purpose, a dedicated Peltier-based cooling stand was developed. The system was capable of contact-cooling devices under test (DUTs) with dimensions up to $80 \times 40 \times 12$ mm down to approximately $-70°C \pm 5\%$ within about 25 min, while dissipating up to 13 W of thermal load. To suppress frosting and stabilize the thermal environment during irradiation, the chamber volume was filled with CO_2, and the temperature was regulated by a PID controller with an accuracy of approximately $\pm 3°C$. The cooled enclosure was placed directly in the irradiation position, so that the transistor could remain electrically connected, thermally biased, and continuously traceable by the same in-situ readout chain used for room-temperature work. As a result, temperature became an explicit experimental axis rather than a post hoc explanatory variable [Paper V].

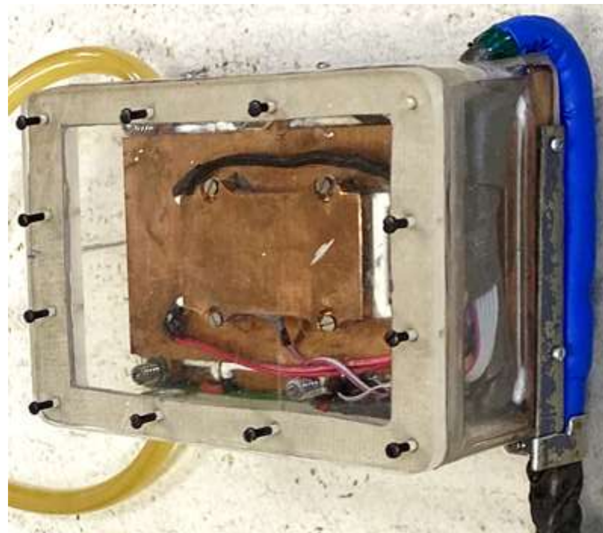

Figure 4.2. Cooling box of the low-temperature irradiation setup used for in-situ measurements at $-70°C$. The fixture integrates thermal control and electrical access during exposure.

For the integrated-circuit experiments, the acquisition strategy was adapted to the logic nature of the DUT. The SiC TTL inverters were irradiated at Hiroshima University using a ^{60}Co source with 15 rod-shaped elements arranged inside a cylindrical source assembly. The applied dose rates were 17.9, 7.3, and 2.47 rad(Si)/s, and an Al/Pb filter was again used to reduce the impact of low-energy secondary photons and improve the stability of the electrical readout. In this campaign, the devices were not reduced to a single scalar output. Instead, the recorded observables were the full transfer characteristics $V_{OUT}(V_{IN})$ and the supply-current traces $I_{CC}(V_{IN})$, both measured over the complete input-voltage range and then re-evaluated in the transition window, where degradation was most pronounced [Paper III].

The key analytical quantities extracted from the inverter data were the shift of the switching region, the variation of the transient supply-current maximum $I_{CC,\max}$, and the displacement of the corresponding input voltage V_{IN}. In contrast to the BJT experiments, where the main objective was to track β-loss, the TTL analysis focused on transfer-curve displacement and transition-current dynamics. This distinction was technically important; the circuit can still preserve valid logic levels while already exhibiting nontrivial degradation in transient current, leakage pathways, or noise-margin position. To capture this behavior, the forward and reverse switching branches were evaluated separately, and the evolution of $I_{CC,\max}$ and its associated V_{IN} value was followed as a function of accumulated dose. The resulting data treatment enabled a direct comparison between different oxide technologies and between passive and actively biased circuit states without relying on a single threshold criterion [Paper II–IV].

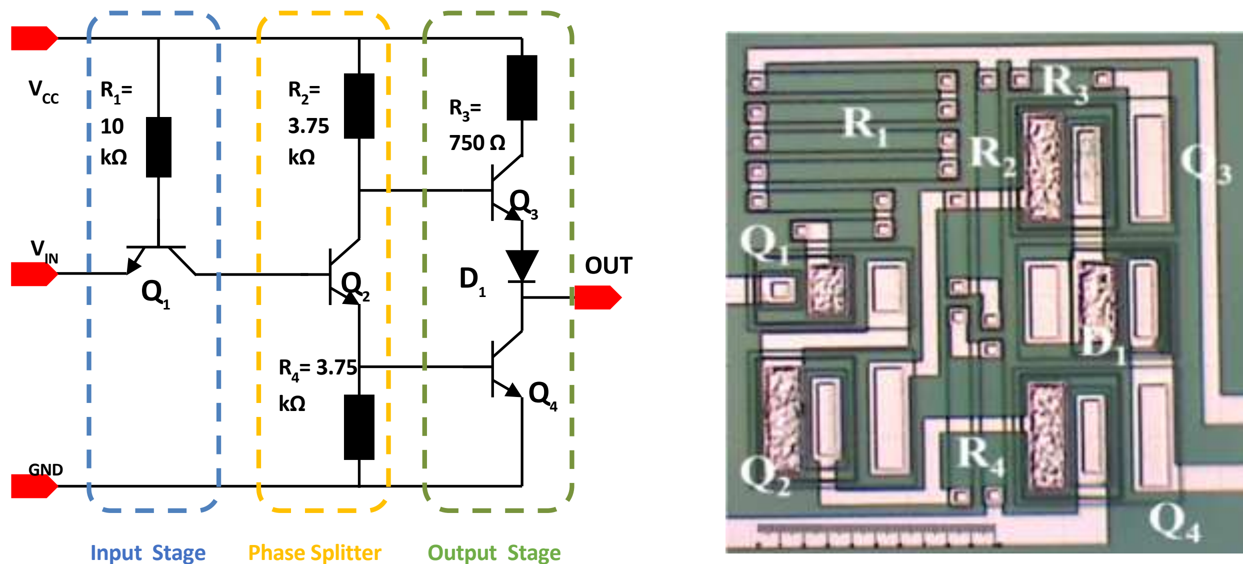

Figure 4.3 BJT SiC Inverter representation (a) A schematic representation of the Integrated inverter TTL IC, (b) A photograph of the fabricated inverter (scale bar is 100 µm)

From a methodological standpoint, the experiments described in this thesis therefore relied on a common acquisition architecture despite the difference in DUT type. In all cases, the workflow combined calibrated ^{60}Co irradiation, filtered spectra, remote guarded measurement hardware, long-line compensation, tightly controlled exposure-to-measurement timing, and repeated sampling with statistical post-processing. The specific observables differed by hierarchy level: I_C, I_B, and $\beta(V_{BE})$ were used for discrete BJTs, while $V_{OUT}(V_{IN})$, $I_{CC}(V_{IN})$, $I_{CC,\max}$, and transition-point shift were used for TTL ICs. However, the underlying philosophy remained the same throughout: the collected data had to preserve the physics of degradation under the actual irradiation state, rather than merely document the post-irradiation condition of the device [Paper I–V].

Chapter 5. Experimental Results

In this chapter, the results from the five appended papers are summarized and briefly discussed. A more general discussion is presented in the following chapter, high-lightening the main finding of the thesis.

5.1 Paper I: In-situ Gamma Irradiation Effects on 4H-SiC Bipolar Junction Transistors

Paper I revisit the widely cited KTH result that the 4H-SiC bipolar platform tolerates very high gamma doses. Instead of treating that result as a final statement of hardness, the paper asks a more demanding question: how strongly does degradation depend on dose rate and bias state, and what does that imply for qualification of the devices. The main result is that current-gain degradation remains moderate in absolute terms - about 22% at 2 Mrad(Si), and below roughly 10% up to 1 Mrad(Si) in, at least, one regime—but it is clearly not regime-independent. The devices remain functional, yet the severity of degradation changes enough with irradiation conditions that hardness cannot be reduced to a single scalar dose limit [Paper I].

The practical significance of Paper I is therefore twofold. First, it confirms that 4H-SiC BJTs are genuinely robust under gamma irradiation. Second, it shows that this robustness is conditional: worst-case behavior must be identified explicitly over bias state and dose rate, rather than inferred from a convenient test condition [Paper I].

The measured dependence on dose rate and bias state is much more consistent with oxide- and interface-controlled ionization damage than with a purely bulk-displacement explanation. In that sense, the paper does not weaken the claim that SiC is radiation hard. Rather, it refines this statement by showing under which conditions the remaining vulnerability becomes visible [49, 46].

An alternative explanation for the observed degradation would be bulk DD from γ-generated Compton electrons. However, the measured dependence on dose rate and bias state, together

with the continuity with known bipolar ionization-damage phenomenology, points much more naturally to an oxide/interface-controlled mechanism than to a purely bulk-displacement picture [Paper I, 49, 64, 65].

In practical terms, Paper I resolves the controversy in a useful way: 4H-SiC BJTs are indeed robust, but that robustness is conditional. Hardness must therefore be expressed as a state-dependent map over dose, dose rate, bias, and temperature, with zero-bias storage and low dose rate treated as explicit worst-case vectors rather than as benign defaults [Paper I].

5.2 Paper II: The Impact of Gamma Irradiation on 4H-SiC Bipolar Junction Inverters under Various Biasing Conditions

Paper II extends the hardness investigation from a single transistor to a monolithic TTL inverter. This step is important because circuit failure is not determined by one parameter alone: even moderate transistor drift can alter current redistribution, transfer characteristics, threshold position, and noise margin in a way that is functionally significant [Paper II].

The inverters were irradiated up to 1 Mrad(Si) under active and passive bias conditions and at different dose rates. The voltage-transfer characteristic was used as the principal functional observable because it shows directly how the balance between pull-up/-down behavior changes with dose [Paper II].

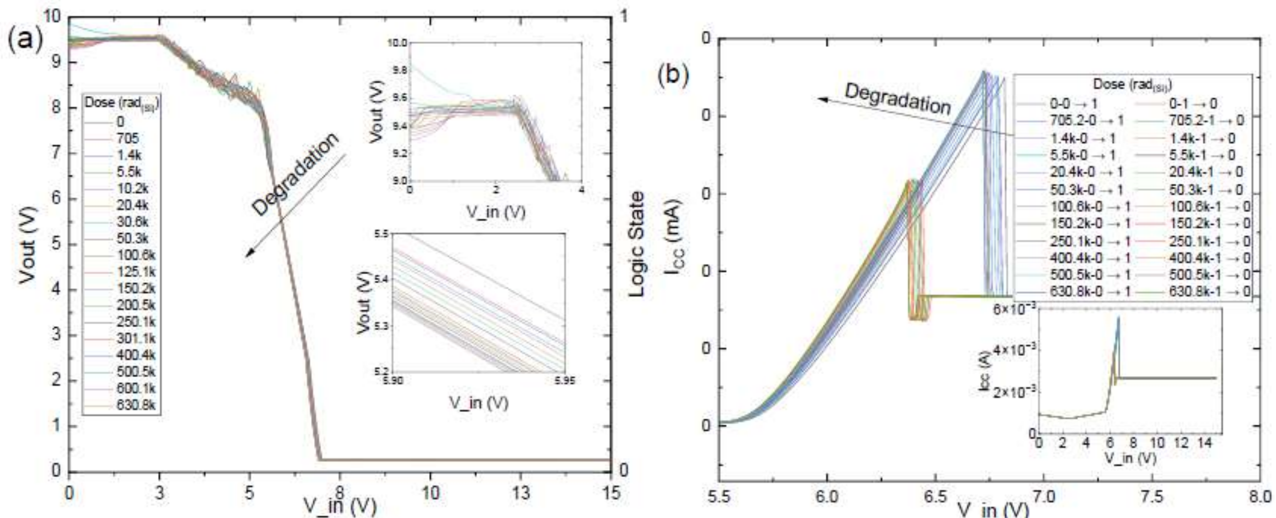

Figure 5.1. Evolution of the voltage transient characteristics of a 4H-SiC TTL inverter as the accumulated dose increases up to 1 Mrad(Si): The passive case exhibits a substantially faster degradation of the high logic level, indicating a more rapid loss of output pull-up capability under unbiased exposure.

The most critical effect of the degrading transistors that can be seen in Figure 5.1 is the collapse of the logic "1" level (V_{OH}). For an ideal inverter, $V_{OH} \approx V_{CC}$, where V_{CC} is the voltage at the common collector. Under irradiation, the forward current gain β of the output transistor and its driver decreases. Maintaining the same load current with reduced β requires higher base drive, which increases voltage drops on internal resistors and shifts the

operating point. V_{OH} decreased by more than ~15–20%, approaching the boundary of valid logic levels [Paper I–II].

Secondly, a shift of the switching threshold (V_M) can also be seen. The switching point V_M shifts leftward in the Figure 5.1. Practically, this means the circuit begins to interpret the input as a logic "1" at a lower voltage, reducing the low-level noise margin NM_L. A consistent physical cause is increased base leakage of the input transistor and redistribution of currents in the phase-splitter or in the output stage [Paper II].

A third result of the irradiation that can be seen in Figure 5.1 is that the stability of the logic "0" level (V_{OL}) remains relatively unaffected. This is consistent with the fact that the lower totem-pole transistor, when "ON", operates in deep saturation. Even with a significant reduction in β, it can still sink the required current without a major increase in V_{OL}.

The most important result of the study in Paper II is the experimental confirmation that unpowered (passive, or un-biased) irradiation is the worst-case condition for SiC TTL logic. The study showed clearly that powered inverters ($V_{CC} = 15\,\mathrm{V}$) showed moderate V_{OH} degradation and only small threshold shifts, while unpowered inverters (passive) exhibited much stronger VTC degradation at high dose. The rate of V_{OH} reduction was ~1.5–2 times higher than in active mode. This is probably caused by the internal electric fields in p–n junctions and isolation oxides under biasing, which can promote drift of radiation-generated holes, reducing their probability of capture at critical interfaces [Paper II].

Paper II also investigates the influence of dose rate on IC parameters. Comparing devices irradiated at 2.47 rad/s (low dose rate, LDR) and 18 rad/s (high dose rate, HDR) indicates behavior consistent with ELDRS-like sensitivity. It is observed that for the same total dose (e.g., 500 krad), the LDR group exhibited a stronger switching-threshold shift than the HDR group. This agrees with a picture in which, at low dose rate, the formation of stable interface states, N_{it}, becomes dominant, whereas at high dose rate a larger fraction of carriers recombine in the oxide before being trapped. For TTL circuits—where input leakage currents and bias-network currents control the switching threshold—the growth of N_{it} (and the associated leakage redistribution) at low dose rate is a critical functional driver [Paper II, 62, 63].

5.3 Paper III: Impact of Interface Oxide Type on the Gamma Radiation Response of SiC TTL IC´s

A fundamental distinction between silicon and SiC technology lies in the stoichiometry of the oxidation process. Unlike silicon, where the oxide interface is abrupt and chemically simple, the thermal oxidation of SiC involves a complex reaction path that inevitably generates carbon by-products. The chemical kinetics can be described as follows [66]:

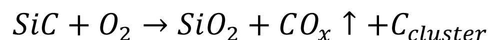

$$SiC + O_2 \rightarrow SiO_2 + CO_x \uparrow + C_{cluster}$$

The incomplete out-diffusion of carbon species leads to the formation of carbon clusters ($CO_xC_{cluster}$) and sub-oxides (SiO_xC_y) at the interface. These defects act as energetically deep hole traps [66].

In the context of RHA, this raises a critical question: is it possible to improve the radiation tolerance by using different process technology, sometimes referred to as hardening by process. To resolve this, a comparative study was conducted on monolithic TTL inverters fabricated using two distinct passivation routes [Paper III].

The study utilized a process split approach on identical circuit topologies, i.e. 4H-SiC TTL inverters, as described earlier in Paper II, to isolate the impact of the dielectric formation method from circuit design factors [Paper II, Paper III].

Two batches are therefore fabricated in this investigation, Batch 1 (Thermal Oxide) where passivation is formed by dry oxidation at 1150°C followed by N_2O annealing. This represents the standard industry baseline.

For Batch 2 (PECVD Oxide), passivation is formed by depositing SiO_2 from TEOS precursors at low temperature, thereby preventing the oxidation of the SiC surface lattice.

Fig. 5.2 compares the relative change in I_{cc} for TTL inverters fabricated with thermally grown oxide and PECVD oxide under different dose-rate and bias conditions.

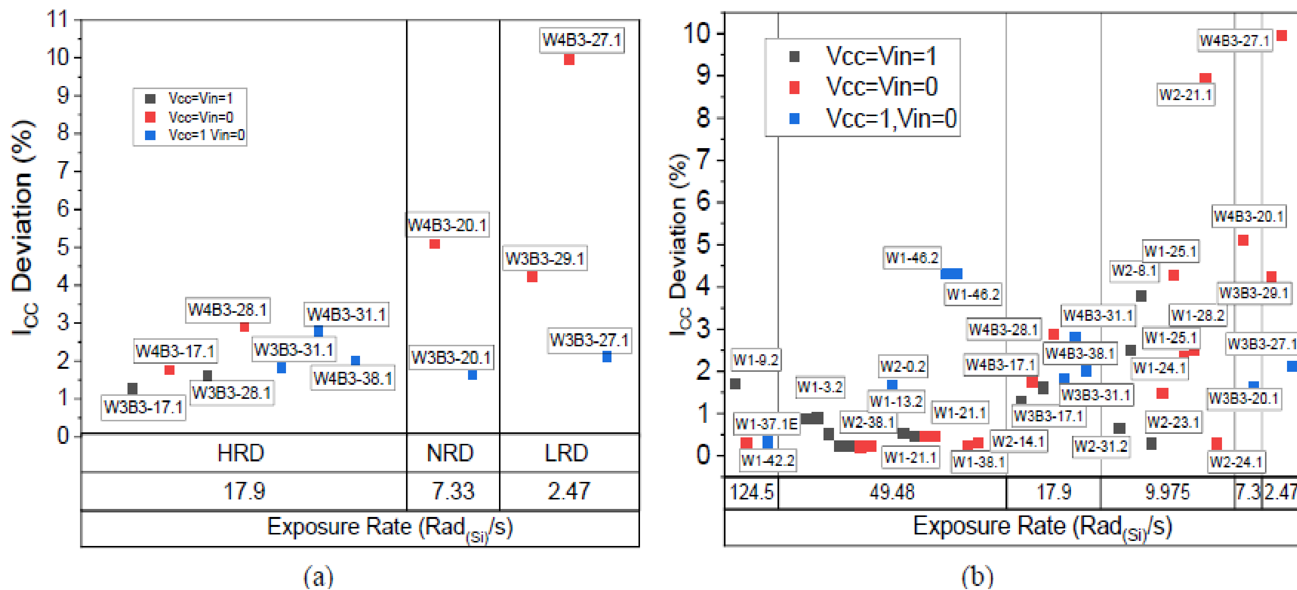

Figure 5.2. Comparative degradation of Voltage Transfer Characteristics for SiC TTL inverters with (a) thermal oxide and (b) PECVD oxide after 500 krad irradiation.

The study showed that the high-level output voltage V_{OH}, which depends on the current gain β of the pull-up transistor, showed distinct degradation rates:

- Thermal Oxide: At 500 krad (LDR), V_{OH} dropped by ~18%, approaching the functional failure margin.

- PECVD Oxide: Under identical conditions, the drop was limited to ~12%.

It can also be seen that devices with thermal oxide exhibited a larger negative shift in the shifting ($beta$), implying a higher rate of positive charge buildup (N_{it}) in the oxide, which modulates the input leakage current.

The superior performance of PECVD oxide–often considered "lower quality" in silicon complementary metal–oxide–semiconductor (CMOS) technology due to bulk porosity—can be explained by the specific defect chemistry of SiC [41, 66].

The total density of radiation-induced interface traps (N_{it}) is proportional to the precursor defect density (N_{pre}) available for activation and may be written as follows:

$$\Delta N_{it}(D) \propto \sigma \cdot N_{pre} \cdot D$$

In thermal oxide: The interface is rich in carbon-related precursor defects ($N_{pre}^{carbon} \gg 0$) generated by the oxidation reaction. These defects have large capture cross-sections (σ) for holes generated by radiation.

In PECVD Oxide: Since the deposition process does not consume the SiC substrate, no carbon is released. The interface is structurally "cleaner" regarding carbon clusters, even if the bulk oxide has a lower density. Consequently, the hole trapping efficiency (f_h) is reduced, leading to slower parameter drift.

Thus, radiation hardness in 4H-SiC bipolar devices is interface-limited, not bulk-limited, and eliminating the oxidation reaction (and thus carbon release) via the PECVD process offers a valid hardening strategy [Paper III, 39, 66].

Finally, it is also shown by the study that ELDRS is not eliminated by changing the oxide type.

Both technologies show an enhancement factor of ≈ 1.8 at low dose rates. This suggests that the kinetic mechanisms responsible for ELDRS (likely proton transport H^+ and metastable hole trapping) are intrinsic to the SiO_2 material system itself, regardless of whether it is grown or deposited. However, because the degradation of PECVD is lower, the final impact of ELDRS is less severe [Paper III, 62, 63].

5.4 Paper IV: SPICE Model for SiC Bipolar Transistor and TTL Inverter Degradation Due to Gamma Radiation

Paper IV addresses a design problem. A device may continue to operate after irradiation, yet its parameter drift may still be large enough to compromise timing, static power, or noise margins in a circuit. The purpose of the modelling work is therefore to express radiation response in a form that circuit designers can use directly [Paper IV].

The VBIC (Vertical Bipolar Inter-Company Model) [67, Paper IV] framework was selected as the compact-model baseline and calibrated against measured BJT characteristics and inverter transfer curves. The fitted parameter shifts link physical degradation at the oxide/interface level to a circuit-level prediction of functional drift.

The reduction in current gain is modeled through the modification of the ideal Forward Beta (BF) and Transport Saturation Current (IS).

The extraction revealed an exponential trend for beta:

$$BF(D) = BF_0 \cdot \exp\left(-k_\beta \cdot D\right)$$

where $k_\beta \approx 4.21 \times 10^{-6}$ per rad.

5.4.1 Increase in saturation current (I_S)

The collector transport saturation current (IS) that describes the carrier transport, exhibits an increase:

$$IS(D) = IS_0 \cdot \exp(k_{IS} \cdot D)$$

In the model, the increase in IS (for a fixed V_{BE}) mathematically compensates for changes in the effective base width and mobility. However, physically, the dominant effect is the increase in the base recombination current which is modeled separately via parasitic diode components.

5.4.2 Increase in Base Resistance (R_B)

The base resistance (RB) demonstrates a linear increase with dose:

$$RB(D) = RB_0 \cdot (1 + k_{RB} \cdot D)$$

Physical Interpretation: ionization generates positive fixed charge in the oxide overlying the extrinsic base region and spacers. This charge depletes the p-type surface areas of majority carriers (holes), thereby narrowing the effective cross-section for base current flow and increasing (RB).

5.4.3 Forward Transit Time (τ_F)

The forward transit time (TF), which determines the cut-off frequency (f_T), also degrades:

$$TF(D) = TF_0 \cdot (1 + k_{TF} \cdot D)$$

The increase in TF is attributed to reduced carrier mobility due to radiation and potential widening of the quasi-neutral base.

The parameter trends extracted at the transistor level are only useful for design if they reproduce circuit-level behaviour. Figure 5.3 compares measured and simulated TTL inverter

transfer characteristics at several dose levels to verify that the compact model captures the dominant circuit degradation trends.

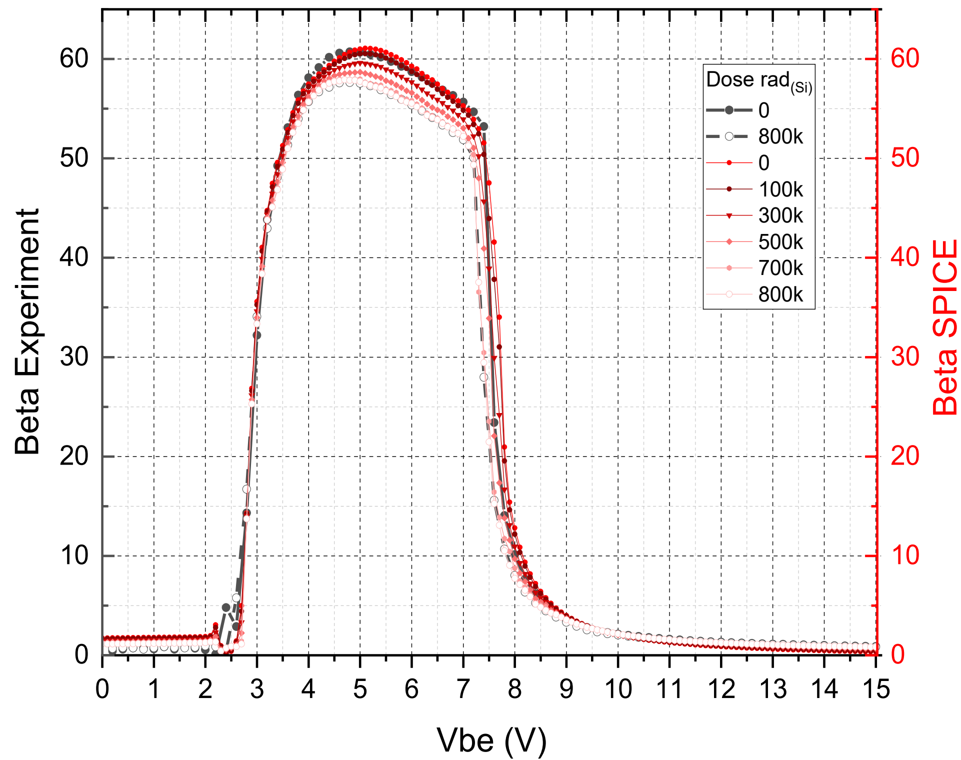

Figure 5.3. Comparison of measured transfer characteristics (symbols) and SPICE-model simulations (solid lines) for a 4H-SiC TTL inverter at different accumulated gamma-dose levels. The agreement demonstrates whether the extracted radiation-dependent BJT parameters reproduce circuit-level VTC degradation.

The model captures both the reduction of the logic-high level and the negative shift of the switching threshold. Using a 30% threshold shift as a practical failure criterion, the fitted model suggests a functional limit on the order of 16 Mrad(Si) for the investigated technology, although dynamic validation under pulsed irradiation remains future work [Paper IV].

5.5 Paper V: Enhanced Gamma Radiation Sensitivity of 4H-SiC Bipolar Junction Transistors at Low Temperatures

5.5.1 Does Low Temperature Improve or Worsen Radiation Stability?

Paper V examines whether low temperature improves or worsens effective TID tolerance. Although lower temperature often reduces conventional leakage-related failure mechanisms, under ionizing irradiation it also slows charge transport and recovery in the oxide, so the net outcome must be determined experimentally.

To isolate this effect, BJTs were irradiated in the worst-case zero-bias regime at room temperature and at cryogenic temperature, using both 200 and 50 rad(Si)/s. Current gain at fixed bias points was used as the main observable.

The results show a clear increase in degradation at low temperature. Even at 200 rad(Si)/s the gain loss is stronger than at room temperature, and in the combined cryogenic and low-dose-rate case the degradation approaches 50% at 1 Mrad(Si), defining the most severe condition observed in the thesis [Paper V].

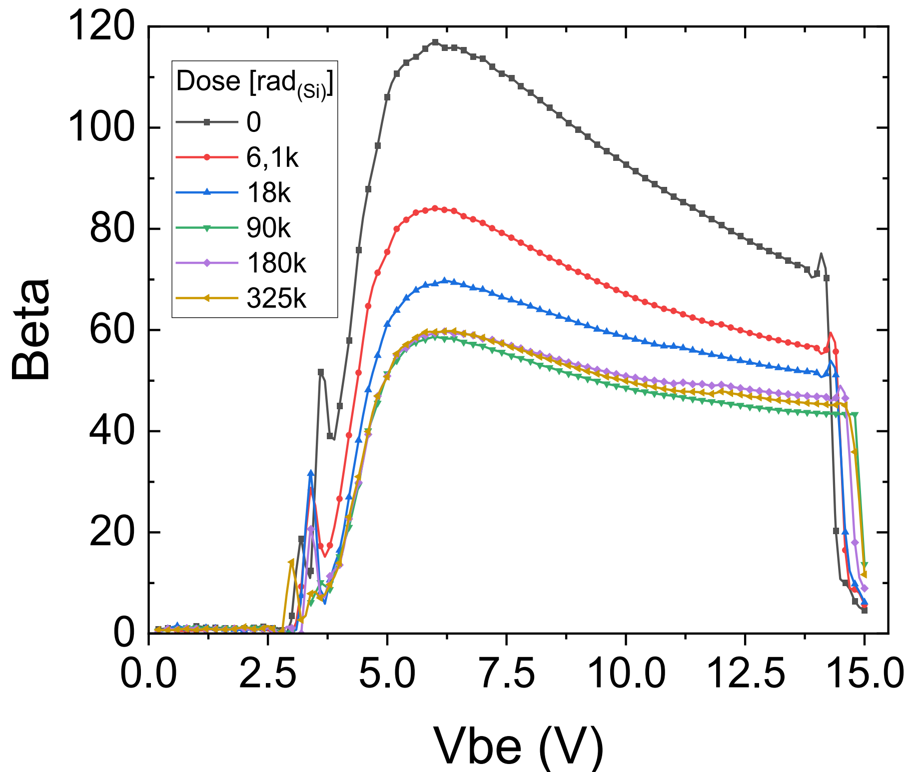

Figure 5.4. Comparative degradation of current gain (β) versus dose at +27°C (0 rad(Si)) and −70°C (6,1k/18k/90k/180k/320 rad(Si)).

The combination of low temperature and low dose rate (Cryo-LDR) represents the most severe scenario observed in this study, with nearly 50% gain loss at a dose of 500 $krad_{(Si)}$.

This means that low temperature does not simply scale the room-temperature response; it changes the effective kinetics of degradation. For deep-space use, qualification performed only at room temperature would therefore overestimate the available radiation lifetime.

5.5.2 Physical Interpretation: The "Frozen Hole" Model

An often suggested hypothesis in γ-irradiation studies is that degradation might stem from bulk DD, making temperature dependence more relevant. However, the strong temperature dependence observed here weakens that argument and points directly to oxide/interface mechanisms.

The anomalous degradation at $-70°C$ is best explained by the fundamental physics of charge transport in amorphous SiO_2, as discussed in *[65]*:

- Unlike electrons, which exit the oxide in picoseconds, holes in SiO_2 transport via a small-polaron hopping mechanism. The hole mobility (μ_p) is exponentially dependent on temperature. At $-70°C$, μ_p plummets by orders of magnitude.
- Because holes are effectively "frozen" in the oxide bulk, they cannot reach the contacts to be swept out or undergo recombination with injected electrons, especially under zero bias conditions. This maximizes the buildup of positive trapped charge (N_{ot}) [Paper V, 65].
- This uncompensated positive charge creates a strong electric field pointing into the SiC p-base, widening the surface depletion region along the mesa sidewall and dramatically increasing the SRH surface recombination rate, which directly reduces β.

Chapter 6. Discussion

6.1 Comparison of Radiation Hardness of Si and SiC Bipolar Transistors

The transition from Si to SiC technology in aerospace applications is driven not only by the need for thermal stability and energy efficiency, but also by the demand for a drastic increase in the lifetime of electronic hardware. While silicon bipolar devices (BJTs) typically approach their radiation-hardness limits at doses on the order of $10^4 - 10^5$ rad(Si), 4H-SiC BJTs can remain functional up to $\sim 10^7$rad(Si) and beyond. This phenomenological gap is explained by fundamental differences in radiation-matter interaction physics. Under gamma irradiation (e.g., ^{60}Co), the dominant degradation mechanism is ionization, which drives charge buildup in passivation layers and promotes the generation of surface states at semiconductor--dielectric interfaces [Paper I, Paper V].

Two fundamental factors underpin the superiority of SiC: the large ionization energy (E_p) and the extremely low intrinsic carrier concentration, n_i. The mean energy required to generate an electron-hole pair in 4H-SiC is $E_p \approx 7.8$ eV, more than twice that of Si (≈ 3.6 eV). Thus, for the same absorbed energy, SiC generates ~ 2.2 times fewer excess carriers, reducing the initial charge yield and the likelihood of forming stable charge traps. The intrinsic carrier concentration (n_i) is a key parameter for leakage currents.

In Si at 300 K, $n_i \approx 10^{10}\text{cm}^{-3}$, whereas in 4H-SiC $n_i \approx 10^{-9}$ cm^{-3}. Since recombination-related currents, a primary degradation channel, scale directly with n_i, SiC possesses an enormous "robustness margin". Even with orders-of-magnitude increases in defect density, the absolute leakage current can remain negligibly small [42].

The key parameters governing the radiation response of a BJT in forward-active operation are those of the non-ideal base-emitter diode, which increase the space-charge region, and at the emitter-base surface:

- I_{SE} (Base-Emitter Leakage Saturation Current): saturation current of the non-ideal (leakage) component.
- N_E (Leakage Emission Coefficient): non-ideality factor. $N_E = 1.5$ is typical for mixed diffusion-recombination, $N_E \approx 2.0$ indicates SRH-dominated recombination, and $N_E > 2.0$ suggests tunneling contributions (TAT)
- BF (Maximum Forward Beta): maximum ideal forward current gain.

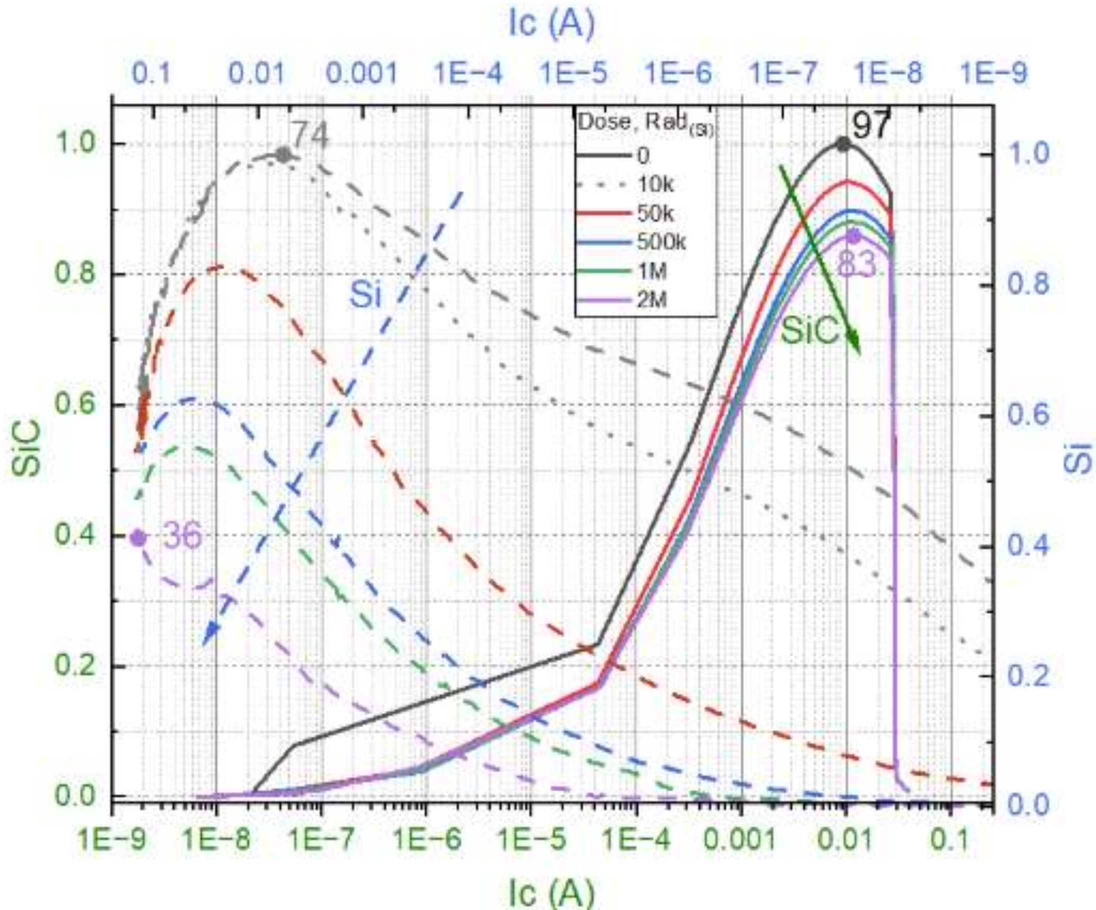

Figure 6.1. Evolution of current gain versus collector current for Si (npn 2N5339 [53]) and 4H-SiC BJTs (npn [Paper V]) under TID. Solid curves correspond to 4H-SiC, dashed curves to Si; colors indicate accumulated dose from 0 to 2 Mrad(Si). Note that the x-axis for Si devices (top scale) is turned in the opposite direction than for SiC to give a clearer view.

Figure 6.1 highlights the markedly different degradation modes in Si and SiC materials: in Si the gain peak collapses and shifts with dose (e.g., peak β drops from ~74 to ~36), while in 4H-SiC the gain remains comparatively stable even at multi-Mrad levels (e.g., ~97 to ~83), with degradation primarily emerging at low-current regimes associated with non-ideal base current components.

Table 6.1 summarizes the SPICE-relevant parameter changes underlying the gain degradation shown in Figure 6.1. The comparison separates changes in the non-ideal base-emitter leakage component, the non-ideality factor, and the maximum forward gain, making

clear why a large relative change in a leakage parameter can have a very different circuit impact in Si and 4H-SiC.

Table 6.1. Comparative degradation of SPICE-relevant BJT parameters for Si and 4H-SiC devices under extreme total ionizing dose conditions. The table highlights changes in the non-ideal base-emitter leakage term, non-ideality factor, and maximum forward current gain used to interpret the gain curves in Figure 6.1.

SPICE par	Pre-rad		100 krad Space typ.		500 krad High rad.		1 Mrad Extreme		2 Mrad Jupiter env	
	Si	SiC	Si	SiC	Si	SiC	Si	SiC	Si	SiC
I_{SE} (A)	1.0×10^{-14}	1.0×10^{-22}	5.0×10^{-12} ($\times 500$)	2.0×10^{-22} ($\times 2$)	1.0×10^{-10} ($\times 10^4$)	5.0×10^{-21} ($\times 50$)	Catastrophic failure	1.0×10^{-19} ($\times 10^3$)	Catastrophic failure	1.0×10^{-17} ($\times 10^5$)
N_E	1.5	2	1.8	2.02	> 2.0	2.1		2.25		2.45
BF	150	50	90 (-40%)	50 (~0%)	< 20 (Failure)	46 (-8%)		42 (-16%)		35 (-30%)
Interpretation	The 8-10 decade gap is fundamentally set by n_i: 10^{10} vs 10^{-9} cm-3. In SiC, recombination often dominates initially due to short lifetime. SiC has lower gain, but operates at far higher voltage class.		Si: oxide charge (N_{ot}) begins to modulate depletion and surface conditions. SiC: change remains masked by absolute scale.		Si: approaching functional failure as leakage becomes comparable to base drive. SiC: activation of D_{it} at mesa sidewalls becomes noticeable. SiC BJT remains fully functional.		Si: critical β drop at low currents. SiC: strong relative rise, but the absolute value (~0.1 aA) remains negligible.		Si: leakage becomes catastrophic. SiC: $N_E > 2$ indicates onset of TAT. Noticeable β degradation mainly in the μA regime. Requires base-drive margin, but remains switchable.	

Note: The 10^{-22} A value for SiC is obtained by extrapolation of a physics-based model; direct measurements below fA are typically instrument-noise limited. In SPICE, this value preserves the correct I-V shape in the ultra-low current regime.

6.1.1 Physical Interpretation: Absolute Current Scale, Bandgap, and Device Topology

The data reveal an apparent paradox: at 2 Mrad, I_{SE} in SiC increases by 10^5, yet the transistor remains functional, whereas a silicon device fails at much smaller relative parameter drift [Paper I, Paper V].

This is explained by the structure of the total base current and by material physics.

6.1.1.1 "Masking" by Intrinsic Carrier Concentration n_i

The base current I_B includes an ideal diffusion component and a recombination/leakage component, as described by [45]:

$$I_B \approx \underbrace{A \cdot n_i^2 \cdot \exp\left(\frac{qV_{BE}}{kT}\right)}_{\text{Injection}} + \underbrace{B \cdot n_i \cdot \sigma \cdot N_{it} \cdot \exp\left(\frac{qV_{BE}}{2kT}\right)}_{\text{Interface Recombination}}$$

A is a prefactor for the ideal diffusion-driven injection component, which includes device geometry; B is a prefactor for the interface-recombination component, again determined by geometry and recombination-active perimeter/area; $\sigma$is the carrier capture cross-section of the interface traps; and $N_{it}$is the areal density of electrically active interface traps at or near the dielectric/semiconductor interface.

Ionizing radiation increases the density of interface traps N_{it}, which linearly amplifies the second term [49, 64, 65].

- In silicon (Si): the intrinsic carrier concentration is $n_i \sim 10^{10}$ cm^{-3}. As radiation defects accumulate, this parasitic current rapidly enters from nano-/micro-Ampere range, becoming comparable to the useful injection current. The result is an effective "shunting" of the emitter junction and a catastrophic drop of current gain [49, 53, 64].
- In SiC: $n_i \sim 10^{-9}$ cm^{-3}, i.e., 19 orders of magnitude lower than in Si. Even if radiation increases the interface trap density N_{it} by a factor of a million (10^6), the absolute parasitic current rises only from a theoretical $\sim 10^{-22}$ A to $\sim 10^{-16}$ A. This current is physically present and grows steeply with dose, but it remains masked by the wide bandgap. It does not affect forward-active operation (mA-A collector currents), because it remains many orders of magnitude below the useful signal [Paper I, Paper V, 53].

6.1.1.2 Transition to TAT

The non-ideality factor N_E in Table 6.1 increases from 2.0 to 2.45 for SiC at 2 Mrad. According to classical SRH theory, the emission/non-ideality coefficient cannot exceed 2.0 for pure SRH recombination. The observed excess therefore unambiguously indicates a change in the dominant transport mechanism. At high doses, the defect density at the SiC/SiO_2 interface for instance on the mesa sidewall becomes critical. These defects act as "stepping stones" enabling multi-step carrier tunneling through the bandgap TAT [68].

In SiC, this effect is more pronounced than in Si due to strong internal electric fields, a consequence of the large built-in potential V_{bi}. However, unlike purely thermal recombination, tunneling current depends only weakly on temperature, which makes a degraded SiC device comparatively stable even under heating [68].

6.1.1.3 Geometrical Factor: Mesa versus Planar Topology

Topology strongly determines susceptibility to leakage-channel formation.

- Si: the base-emitter junction is located beneath an oxide layer (spacer oxide). Accumulation of positive oxide charge N_{ot} inverts the p-base surface, forming a

conductive n-channel between emitter and collector. This produces an uncontrolled leakage current I_{CES} and leads to functional failure [49, 64].

- SiC: the junction terminates at a vertical etched sidewall. The SiC base is heavily doped ($N_A \gtrsim 10^{17}$ cm^{-3}) to reduce base resistance. Inverting such a surface would require an electric field that cannot be generated by radiation-induced charge alone. Radiation modulates the near-surface space-charge region width and the surface recombination rate, but it does not form via device leakage channels [Paper III, 39].

Taken together, the comparison supports a practical conclusion: SiC does not eliminate radiation-induced degradation, but it shifts the failure problem from early catastrophic collapse toward a broader region of parametric drift that remains designable. This is precisely why compact modelling, bias-aware testing, and low-dose-rate qualification matter so much for the practical use of SiC in extreme environments [Paper I, Paper III, Paper V].

Three points follow from this analysis.

- Si and SiC do not degrade in the same way or on the same absolute scale.
- The useful design margin in SiC can remain substantial even after measurable parameter drift.
- The combination of HV capability, thermal tolerance and extended functional failure makes 4H-SiC BJTs realistic enabling technology for missions and systems in which conventional silicon is difficult to use [Paper I, Paper V].

In silicon, ionization damage often progresses toward structural or topological failure, for example through channel formation, severe leakage growth, or gain collapse at relatively modest doses. In 4H-SiC, the dominant effect under the conditions studied here is instead a gradual drift of parameters associated with surface recombination and interface-controlled leakage.

Because of this difference, circuit-level design margins can also be treated differently. Silicon often requires large guard bands simply to avoid abrupt failure, whereas in SiC a smaller but still explicit margin may be sufficient if the relevant worst-case irradiation regime has been identified and modelled correctly [Paper IV]. This combination of intrinsic material advantage and manageable degradation behavior is what makes SiC a promising technology for harsh applications such as Jovian missions, cold-space electronics, and control systems for nuclear environments.

The broader lesson is that the radiation robustness of 4H-SiC BJTs should not be framed as an automatic consequence of material choice alone. It is better understood as a material advantage that becomes genuinely useful only when coupled to correct testing logic, interface-aware processing, and predictive modelling [Paper I, Paper III–V].

Chapter 7. Conclusions

Studying radiation effects in SiC is a fundamental step toward electronics capable of reliable operation in extreme environments from deep space to nuclear reactors. Owing to its wide bandgap and high atomic bond energy, SiC exhibits exceptionally strong intrinsic radiation hardness. However, as the experimental results in this thesis clearly demonstrate, stating material-level robustness is only the first step. True reliability requires understanding under which conditions that hardness holds and under which conditions the system becomes vulnerable. This chapter presents a summary of gamma irradiation effects on a bipolar SiC technology platform. By moving systematically from discrete transistors to logic elements and finally to predictive SPICE macro models, the work establishes a rigorous methodology for radiation-hardness assessment of wide-bandgap electronics. The central conclusion is that the radiation hardness of 4H-SiC bipolar devices is not an absolute, static quantity only depending on irradiation dose. Instead, it is deeply conditional and depends critically on the device and circuit's operating regime, the temperature and dose rate.

At the discrete device level (Paper I), SiC BJTs were shown to exhibit an exceptionally low radiation-damage coefficient (K_β in the order of 10^{-9}rad^{-1}). Nevertheless, the use of advanced in-situ measurements revealed a counterintuitive phenomenon: the worst-case degradation scenario corresponds to the passive (zero-bias) condition. In the absence of an electric field, radiation-generated charge does not leave the oxide volume but is efficiently captured near the interface. Furthermore, experiments confirmed the presence of ELDRS, demonstrating that slow, long-duration dose accumulation can be more damaging than short, high-rate exposure.

By evaluating TTL inverters (Paper II), the study shows that the transistor-level "zero-bias phenomena" scales directly to the IC-level. As a consequence, the widely used aerospace strategy of cold sparing, keeping redundant blocks unpowered, becomes risky for bipolar SiC logic.

In Paper III, a comparison of ICs fabricated with different passivation oxide types resolves a long-standing scientific dispute. The experimental results unambiguously support the

hypothesis of interface-limited hardness. Thermal oxidation of SiC inevitably leaves carbon-related residues at the SiC/SiO_2 interface, which act as efficient traps for radiation-induced holes. PECVD, which does not consume the SiC surface, led to a substantial increase in radiation tolerance at the circuit level. This demonstrates that the practical hardness limit of SiC technology has not yet been reached and can be significantly improved through process optimization, so called hardness-by-process.

A major engineering achievement of this work (Paper IV) is the conversion of observed physical degradation into a practical tool for circuit designers. A device that simply "survives" irradiation may still exhibit hidden parameter drift that can destabilize complex circuits.

By extracting experimental trends, a dose-dependent model based on VBIC SPICE was developed. Through parameterizing the degradation of current gain (β), base resistance (R_B), and transit time (τ_F), radiation exposure was transformed into a predictable simulation variable. Using this model, a strict functional failure criterion for TTL inverters was defined (a 30% shift of the switching threshold V_M), and extrapolation predicted an impressive functional limit exceeding 16 Mrad(Si).

Finally, the study extended the operational envelope to deep-space conditions is examined (Paper V). In conventional engineering practice, low temperature is often assumed to stabilize electronics by slowing degradation mechanisms. This phenomenon is explained by polaron transport physics: at such low temperatures, hole mobility in the oxide collapses, holes become effectively "frozen" in the dielectric, natural relaxation/annealing pathways are blocked, and a strong shielding electric field is formed. The result is a critical warning: qualifying SiC components only at room temperature can dangerously overestimate lifetime for cold space environments.

The results presented in this thesis open several directions for future research. Further investigation of dose-rate effects over a wider range, including very low dose rates, is required to fully characterize potential ELDRS behaviour in 4H-SiC bipolar devices. Also, studies involving other radiation types, such as neutrons, protons, and heavy ions, would provide a more comprehensive understanding of DD and SEE in this technology. In-situ circuit-level measurements during irradiation should be expanded to capture dynamic behaviour and transient effects that are not observable in post-irradiation measurements. Detailed characterization of interface states and oxide traps, including their energy distribution and evolution under irradiation, would improve the physical understanding of degradation mechanisms. It would also provide input to a further optimization of oxide and interface processes that represents a promising pathway for improving the radiation tolerance of SiC bipolar devices and ICs. Finally, further development of compact models that incorporate radiation effects in a predictive and technology-independent manner is needed to support circuit design under harsh conditions.

References

[1] D. M. Fleetwood, “Radiation Effects in a Post-Moore World,” in 2020 IEEE NSREC Short Course, 2020.
Identifier: IEEE NSREC Short Course 2020
Link: https://www.nsrec.com/short-course-archive/

[2] R. Bowman, “Radiation Hardness Assurance in the ‘Wild West’ of Commercial Space,” in 2020 IEEE NSREC Short Course, 2020.
Identifier: IEEE NSREC Short Course 2020
Link: https://www.nsrec.com/short-course-archive/

[3] M. Kamiński et al., “The Overview of Silicon Carbide Technology: Status, Challenges, Key Drivers, and Product Roadmap,” Materials, vol. 18, no. 1, Art. no. 12, 2025.
DOI: 10.3390/ma18010012
ISSN: 1996-1944

[4] L. Lanni, Silicon Carbide Bipolar Technology for High Temperature Integrated Circuits, Ph.D. dissertation, KTH Royal Institute of Technology, Stockholm, Sweden, 2014.
ISBN: 978-91-7595-135-5

[5] D. Johannesson, Ultrahigh-Voltage Silicon Carbide Device Performance, Requirements, and Limitations in High-Power Applications, Ph.D. dissertation, KTH Royal Institute of Technology, Stockholm, Sweden, 2021.
Identifier: KTH DiVA record 1555396

[6] European Cooperation for Space Standardization (ECSS), ECSS-E-HB-10-12A: Space Engineering, Methods for the Calculation of Radiation Received and Its Effects, and a Policy for Design Margins, Noordwijk, The Netherlands, 2010.
Identifier: ECSS-E-HB-10-12A
Link: https://ecss.nl/wp-content/uploads/handbooks/ecss-e-hb/ECSS-E-HB-10-12A17December2010.pdf

[7] S. S. Suvanam, Radiation Hardness of 4H-SiC Devices and Circuits, Ph.D. dissertation, KTH Royal Institute of Technology, Stockholm, Sweden, 2017.
Identifier: KTH DiVA record 1066193

[8] S. A. Wender and M. Dominik, Los Alamos High-Energy Neutron Testing Handbook, Los Alamos National Laboratory, 2020.
Report No.: LA-UR-19-30813

[9] R. Ghandi, Fabrication Technology for Efficient High Power Silicon Carbide Bipolar Junction Transistors, Ph.D. dissertation, KTH Royal Institute of Technology, Stockholm, Sweden, 2011.
ISBN: 978-91-7415-861-8

[10] G. P. Summers et al., "Correlation of Particle-Induced Displacement Damage in Silicon," IEEE Transactions on Nuclear Science, vol. 34, no. 6, pp. 1134–1139, 1987.
DOI: 10.1109/TNS.1987.4337442
ISSN: 0018-9499

[11] A. M. Ivanov et al., "Radiation resistance of wide-gap materials as exemplified by SiC nuclear radiation detectors," Technical Physics, vol. 57, no. 4, pp. 556–560, 2012.
DOI: 10.1134/S1063784212040111
ISSN: 1063-7842

[12] M. Shakir, Process Design Kit and High-Temperature Digital ASICs in Silicon Carbide, Ph.D. dissertation, KTH Royal Institute of Technology, Stockholm, Sweden, 2019.
Identifier: KTH DiVA record 1317122

[13] M. W. Hussain, High-Temperature Radio Circuits in Silicon Carbide Bipolar Technology, Ph.D. dissertation, KTH Royal Institute of Technology, Stockholm, Sweden, 2019.
Identifier: KTH DiVA record 1306687

[14] S. Hou, Silicon Carbide High Temperature Photodetectors and Image Sensor, Ph.D. dissertation, KTH Royal Institute of Technology, Stockholm, Sweden, 2019.
Identifier: KTH DiVA record 1303493

[15] International Atomic Energy Agency, Radiation Protection and Safety of Radiation Sources: International Basic Safety Standards, General Safety Requirements Part 3, Vienna, Austria, 2014.
DOI: 10.61092/iaea.u2pu-60vm
ISBN: 978-92-0-135310-8; ISSN: 1020-525X

[16] International Atomic Energy Agency, IAEA Safety Glossary: Terminology Used in Nuclear Safety and Radiation Protection, 2018 Edition, Vienna, Austria, 2019.
ISBN: 978-92-0-104718-2; Report ID: STI/PUB/1830

[17] E. B. Podgorsak, Ed., Radiation Oncology Physics: A Handbook for Teachers and Students. Vienna, Austria: International Atomic Energy Agency, 2005.
ISBN: 92-0-107304-6; Report ID: STI/PUB/1196

[18] E. B. Podgorsak, Ed., Radiation Biology: A Handbook for Teachers and Students. Vienna, Austria: International Atomic Energy Agency, 2010.
ISSN: 1018-5518; Report ID: IAEA-TCS-42

[19] P. G. Neudeck et al., "Operational Testing of 4H-SiC JFET ICs for 60 Days Directly Exposed to Venus Surface Atmospheric Conditions," IEEE Journal of the Electron Devices Society, 2019.
DOI: 10.1109/JEDS.2018.2882693
ISSN: 2168-6734

[20] T. Sato, T. Endo, M. Zankl, D. Petoussi-Henss, and K. Saito, "Analytical Model for Estimating Terrestrial Cosmic Ray Fluxes Nearly Anytime and Anywhere in the World: Extension of PARMA/EXPACS," PLoS One, vol. 10, no. 12, Art. no. e0144679, 2015.
DOI: 10.1371/journal.pone.0144679
ISSN: 1932-6203

[21] I. G. Usoskin and G. A. Kovaltsov, "Cosmic Ray Induced Ionization in the Atmosphere: Full Modeling and Practical Applications," Journal of Geophysical Research, vol. 111, Art. no. D21206, 2006.
DOI: 10.1029/2006JD007150
ISSN: 0148-0227

[22] A. D. P. Hands et al., "The Disappearance of the Pfotzer-Regener Maximum in Dose Equivalent Measurements in the Lower Atmosphere," Space Weather, vol. 14, pp. 776–785, 2016.
DOI: 10.1002/2016SW001402
ISSN: 1542-7390

[23] K. O'Brien, W. Friedberg, H. H. Sauer, and D. F. Smart, "Atmospheric Cosmic Rays and Solar Energetic Particles at Aircraft Altitudes," Environment International, vol. 22, Suppl. 1, pp. S9–S44, 1996.
DOI: 10.1016/S0160-4120(96)00086-4
ISSN: 0160-4120

[24] W. Li and M. K. Hudson, "Earth's Van Allen Radiation Belts: From Discovery to the Van Allen Probes Era," Journal of Geophysical Research: Space Physics, vol. 124, no. 11, pp. 8319–8351, 2019.
DOI: 10.1029/2018JA025940
ISSN: 2169-9380

[25] K. Whitman et al., "Review of Solar Energetic Particle Models," Advances in Space Research, vol. 72, no. 12, pp. 5161–5242, 2023.
DOI: 10.1016/j.asr.2022.08.006
ISSN: 0273-1177

[26] J. H. Hubbell, H. A. Gimm, and I. Øverbø, "Pair, Triplet, and Total Atomic Cross Sections (and Mass Attenuation Coefficients) for 1 MeV–100 GeV Photons in

Elements Z = 1 to 100," Journal of Physical and Chemical Reference Data, vol. 9, no. 4, pp. 1023–1147, 1980.
DOI: 10.1063/1.555629
ISSN: 0047-2689

[27] M. A. Xapsos et al., "A Brief History of Space Climatology: From the Big Bang to the Present," IEEE Transactions on Nuclear Science, vol. 66, no. 1, pp. 17–37, 2019.
DOI: 10.1109/TNS.2018.2885649
ISSN: 0018-9499

[28] J. A. Simpson, "Elemental and Isotopic Composition of the Galactic Cosmic Rays," Annual Review of Nuclear and Particle Science, vol. 33, pp. 323–382, 1983.
DOI: 10.1146/annurev.ns.33.120183.001543
ISSN: 0163-8998

[29] European Cooperation for Space Standardization (ECSS), ECSS-E-HB-20-06A: Spacecraft Charging Handbook, Noordwijk, The Netherlands, May 15, 2019.
Identifier: ECSS-E-HB-20-06A

[30] National Aeronautics and Space Administration (NASA), NASA-HDBK-4002B: Mitigating In-Space Charging Effects, A Guideline, Washington, DC, USA, Jun. 7, 2022.
Identifier: NASA-HDBK-4002B

[31] S. R. Messenger et al., "NIEL for Heavy Ions: An Analytical Approach," IEEE Transactions on Nuclear Science, vol. 50, no. 6, 2003.
DOI: 10.1109/TNS.2003.820762
ISSN: 0018-9499

[32] European Cooperation for Space Standardization (ECSS), ECSS-Q-ST-60-15C: Space Product Assurance—Radiation Hardness Assurance—EEE Components, Oct. 1, 2012.
Identifier: ECSS-Q-ST-60-15C

[33] European Cooperation for Space Standardization (ECSS), ECSS-E-ST-10-12C Rev.1 Corr.1: Space Engineering, Methods for the Calculation of Radiation Received and Its Effects, and a Policy for Design Margins, Noordwijk, The Netherlands, Feb. 22, 2017.
Identifier: ECSS-E-ST-10-12C Rev.1 Corr.1

[34] A. F. Witulski et al., "Single-Event Burnout Mechanisms in SiC Power MOSFETs," IEEE Transactions on Nuclear Science, vol. 65, no. 8, pp. 1951–1955, 2018.
DOI: 10.1109/TNS.2018.2849405
ISSN: 0018-9499

[35] M. J. Campola et al., Compendium of Total Ionizing Dose and Displacement Damage Results from NASA Goddard Space Flight Center, NASA/GSFC, 2016.
Document ID: 20160009071

[36] J.-M. Lauenstein et al., “Recent Radiation Test Results for Trench Power MOSFETs,” in IEEE Radiation Effects Data Workshop, 2017.
DOI: 10.1109/NSREC.2017.8115473

[37] Japan Aerospace Exploration Agency, “JERG-2-211: Environmental Test Methods,” 2017.
Link: https://sma.jaxa.jp/TechDoc/Docs/E_JAXA-JERG-2-211A.pdf

[38] Japan Aerospace Exploration Agency, JERG-2-143: Design Standard, Space Environment Effects Mitigation (Radiation Resistance Design Standard), English translation, Sept. 3, 2008.
Identifier: JERG-2-143

[39] National Institutes for Quantum Science and Technology, QST Takasaki Annual Report 2023, Takasaki Institute for Advanced Quantum Science, Takasaki, Japan, 2023
Report ID: QST-M-51

[40] R. Wei et al., “Thermal Conductivity of 4H-SiC Single Crystals,” Journal of Applied Physics, vol. 113, Art. no. 053503, 2013.
DOI: 10.1063/1.4790134
ISSN: 0021-8979

[41] M. Usman, B. Buono, and A. Hallén, “Impact of Ionizing Radiation on the SiO_2/SiC Interface in 4H-SiC BJTs,” IEEE Transactions on Electron Devices, vol. 59, no. 12, pp. 3371–3376, 2012.
DOI: 10.1109/TED.2012.2222414
ISSN: 0018-9383

[42] A. Holmes-Siedle and L. Adams, Handbook of Radiation Effects. Oxford, U.K.: Oxford University Press.
Link: https://global.oup.com/academic/product/handbook-of-radiation-effects-9780198507338

[43] F. C. Beyer, Deep Levels in SiC, Ph.D. dissertation, Linköping University, Linköping, Sweden, 2011.
ISBN: 978-91-7393-100-7; ISSN: 0345-7524

[44] H.-S. Lee, M. Domeij, C.-M. Zetterling, M. Östling, F. Allerstam, and E. Ö. Sveinbjörnsson, “Surface Passivation Oxide Effects on the Current Gain of 4H-SiC Bipolar Junction Transistors,” Applied Physics Letters, vol. 92, no. 8, Art. no. 082113, 2008.
DOI: 10.1063/1.2888965
ISSN: 0003-6951

[45] B. Buono, R. Ghandi, M. Domeij, B. G. Malm, C.-M. Zetterling, and M. Östling, “Modeling and Characterization of Current Gain Versus Temperature in 4H-SiC Power BJTs,” IEEE Transactions on Electron Devices, vol. 57, no. 3, pp. 704–711, 2010.

DOI: 10.1109/TED.2009.2039099
ISSN: 0018-9383

[46] S. A. Campbell, Fabrication Engineering at the Micro- and Nanoscale. Oxford, U.K.: Oxford University Press, 2008.
ISBN: 978-0199861224

[47] P. S. Winokur, H. E. Boesch, Jr., J. M. McGarrity, and F. B. McLean, "Two-Stage Process for Buildup of Radiation-Induced Interface States," Journal of Applied Physics, vol. 50, no. 5, 1979.
DOI: 10.1063/1.326344

[48] F. B. McLean and T. R. Oldham, Basic Mechanisms of Radiation Effects in Electronic Materials and Devices, Harry Diamond Laboratories, Tech. Rep. HDL-TR-2129, 1987.
Report No.: HDL-TR-2129

[49] T. R. Oldham and F. B. McLean, "Total Ionizing Dose Effects in MOS Oxides and Devices," IEEE Transactions on Nuclear Science, vol. 50, no. 3, pp. 483–499, 2003.
DOI: 10.1109/TNS.2003.812927
ISSN: 0018-9499

[50] S. J. Pearton et al., "Radiation Damage in GaN/AlGaN and SiC Electronic and Photonic Devices," Journal of Vacuum Science & Technology B, vol. 41, Art. no. 030802, 2023.
DOI: 10.1116/6.0002628
ISSN: 2166-2746

[51] P. J. Griffin et al., "Uncertainty in Silicon Displacement Damage Metrics due to the Displacement Threshold Treatment," in RADECS 2016.
DOI: 10.1109/RADECS.2016.8093101

[52] A. S. Hauck et al., "Atomic displacement threshold energies and defect generation in GaN, AlN, and AlGaN: A high-throughput molecular dynamics investigation," Applied Physics Letters, vol. 124, Art. no. 152107, 2024.
DOI: 10.1063/5.0190371
ISSN: 0003-6951

[53] G. C. Messenger and M. S. Ash, The Effects of Radiation on Electronic Systems. New York, NY, USA: Van Nostrand Reinhold, 1992.
ISBN: 978-0442239527

[54] P. Hazdra et al., "Displacement Damage and Total Ionisation Dose Effects on 4H-SiC Power Devices," IET Power Electronics, vol. 12, no. 15, pp. 3908–3915, 2019.
DOI: 10.1049/iet-pel.2019.0049
ISSN: 1755-4535

[55] N. T. Son et al., "Negative-U System of Carbon Vacancy in 4H-SiC," Physical Review Letters, vol. 109, Art. no. 187603, 2012.

DOI: 10.1103/PhysRevLett.109.187603
ISSN: 0031-9007

[56] R. Karsthof, M. E. Bathen, A. Galeckas, and L. Vines, “Conversion Pathways of Primary Defects by Annealing in Proton-Irradiated n-Type 4H-SiC,” Physical Review B, vol. 102, Art. no. 184111, 2020.
DOI: 10.1103/PhysRevB.102.184111
ISSN: 2469-9950

[57] L. Storasta, F. H. C. Carlsson, J. P. Bergman, and E. Janzén, “Enhanced Annealing of the (Z1/2) Defect in 4H-SiC Epilayers,” Journal of Applied Physics, vol. 103, Art. no. 013705, 2008.
DOI: 10.1063/1.2829776
ISSN: 0021-8979

[58] A. Javanainen et al., “Heavy-Ion-Induced Degradation in SiC Schottky Diodes: Incident Angle and Energy Deposition Dependence,” IEEE Transactions on Nuclear Science, vol. 64, no. 8, pp. 2031–2037, 2017.
DOI: 10.1109/TNS.2017.2717045
ISSN: 0018-9499

[59] European Space Components Coordination, Basic Specification No. 22900: Total Dose Steady-State Irradiation Test Method.
Identifier: ESCC Basic Specification No. 22900

[60] U.S. Department of Defense, MIL-STD-883L, Method 1019.9: Ionizing Radiation (Total Dose) Test Procedure, 2019.
Identifier: MIL-STD-883L, Method 1019.9

[61] R. F. Hodson et al., Avionics Radiation Hardness Assurance (RHA) Guidelines, NASA/TM-20210018053, 2021.
Identifier: NASA/TM-20210018053

[62] A. H. Johnston, B. G. Rax, C. I. Lee, and J. L. Titus, “Enhanced Damage in Bipolar Devices at Low Dose Rates: Effects at Very Low Dose Rates,” IEEE Transactions on Nuclear Science, vol. 43, no. 6, pp. 3049–3059, 1996.
DOI: 10.1109/23.556904
ISSN: 0018-9499

[63] D. M. Fleetwood et al., “Physical Mechanisms Contributing to Enhanced Bipolar Gain Degradation,” IEEE Transactions on Nuclear Science, vol. 41, no. 6, pp. 1871–1883, 1994.
ISSN: 0018-9499

[64] J. R. Schwank et al., “Radiation Effects in MOS Oxides,” IEEE Transactions on Nuclear Science, vol. 55, no. 4, pp. 1833–1853, 2008.
DOI: 10.1109/TNS.2008.2001040
ISSN: 0018-9499

[65] H. E. Boesch, Jr. and F. B. McLean, “Hole Transport and Trapping in Field Oxides,” IEEE Transactions on Nuclear Science, vol. 32, no. 6, pp. 3940–3945, Dec. 1985.
DOI: 10.1109/TNS.1985.4334047
ISSN: 0018-9499

[66] V. V. Afanas’ev et al., “Oxidation of Silicon Carbide: Problems and Solutions,” Materials Science Forum, vols. 389–393, pp. 961–966, 2002.
DOI: 10.4028/www.scientific.net/MSF.389-393.961
ISSN: 0255-5476

[67] C. C. McAndrew et al., “VBIC95, The Vertical Bipolar Inter-Company Model,” IEEE Journal of Solid-State Circuits, vol. 31, no. 10, pp. 1476–1483, 1996.
DOI: 10.1109/4.540058
ISSN: 0018-9200

[68] J. Berens, M. V. Mistry, D. Waldhör, A. Shluger, G. Pobegen, and T. Grasser, “Origin of trap assisted tunnelling in ammonia annealed SiC trench MOSFETs,” Microelectronics Reliability, vol. 139, Art. no. 114789, 2022.
DOI: 10.1016/j.microrel.2022.114789
ISSN: 0026-2714